Linking advanced fracture models to structural analysis

BY

MATTEO CHIESA

Faculty of Mechanical Engineering
Department of applied mechanics, thermodynamics and fluiddynamics
The Norwegian University of Science and Technology

October 26, 2001
Trondheim, Norway

Tò pödet mia tirá fó ö caal de corsa da ö caal bóls

Preface

Shell structures with defects occur in many situations. The defects are usually introduced during the welding process necessary for joining different parts of the structure.

Higher utilization of structural materials leads to a need for accurate numerical tools for reliable prediction of structural response. The direct discretization of the cracked shell structure with solid finite elements in order to perform an integrity assessment of the structure in question leads to large size problems, and makes such analysis infeasible in structural application.

In this study a link between local material models and structural analysis is outlined. An *"ad hoc"* element formulation is used in order to connect complex material models to the finite element framework used for structural analysis. An improved elasto-plastic line spring finite element formulation, used in order to take cracks into account, is linked to shell elements which are further linked to beam elements. In this way one obtain a global model of the shell structure that also accounts for local flexibilities and fractures due to defects. An important advantage with such an approach is a direct fracture mechanics assessment e.g. via computed $J-$integral or $CTOD$. A recent development in this approach is the notion of two-parameter fracture assessment. This means that the crack tip stress tri-axiality (constraint) is employed in determining the corresponding fracture toughness, giving a much more realistic capacity of cracked structures. The present thesis is organized in six research articles and an introductory chapter that reviews important background literature related to this work.

Paper I and *II* address the performance of shell and line spring finite elements as a cost effective tool for performing the numerical calculation needed to perform a fracture assessment.

In *Paper II* a failure assessment, based on the testing of a constraint-corrected fracture mechanics specimen under tension, is proposed. Such specimen is designed in order to have the same geometrical constraint of the real structure which has to be assessed.

Paper III presents an alternative yield surfaces of plane strain single-cracked (SEC) specimens valid for both shallow and deep cracks. The performance of the backward-Euler return algorithm is addressed in order to evaluate the implementability of the proposed yield surface.

In *Paper IV* a SENT specimen is designed in order to give a constraint level comparable to the one calculated for a pipe by means of the modified line spring element.

Paper V presents a methodology to link micro-mechanically based crack growth simulations with line spring analysis by suggesting an alternative way to calculate the $J - integral$ from the line spring framework. *Paper VI* presents an application of the new line spring for pipelines subjected to e.g. large curvatures.

Acknowledgment

The present thesis has been submitted to NTNU[1] at the Faculty of Mechanical Engineering, Department of applied mechanics, thermodynamics and fuiddynamics in partial fulfillment of the requirements for the Norwegian academic title "DOKTOR INGENIØR".

The present work would probably not have been started or even finished without the continuous encouragements of my supervisor, Prof. Bjørn Skallerud. Bjørn has always been available for discussions of my often inconsistent ideas, giving valuable feedback not just limited to my research, but also covering other important issues of life. For these reasons I strongly recommend him as supervisor to any other students interested in research.

I also thank my Co-supervisor Prof. Christian Thaulow for his guide and encouragement thought my research and for obtaining the funding for my PhD.

The interest shown by my colleagues at Dept. of Fracture Mechanics and Material Testing at SINTEF[2] has positively contributed to my motivation, necessary to complete my work. In particular I am very grateful to my friend and fellow doctoral student Erling Østby who has helped me with many theoretical problems. Erling has been very generous with his time and he has always been available for discussions. Sincere thanks go also to Dr. Tore Holmås and Dr. Bård Nyhus for their productive collaboration.

During my studies, I had also the pleasure of staying 7 months at the Fachbereich Mechanik Technische Universität Darmstadt[3] in Germany. The help from the fellow doctoral students and the supervision of Prof. Dietmar Gross was important to make my stay as effective as possible.

My family has always been a source of motivation and objectivity which I often lack of, even at a distance of 3000 km. My friends need also to be mentioned for their ability to keep me in contact with Bacco and the smoothness of his unbounded world. THANK YOU!

This research was supported financially by Statoil[4] and the Norwegian Research Council within a project aimed at developing a better understanding of high-strength-steel behavior.

---

[1]Norwegian University of Science and Technology http//:www.ntnu.no
[2]SINTEF Dept. of Fracture Mechanics and Material Testing http://www.sintef.no/units/matek/2460/
[3]Fachbereich Mechanik Technische Universität http://www.mechanik.tu-darmstadt.de/
[4]Statoil http://www.statoil.com

Linking advanced fracture models to structural analysis

Contents

Paper I: Line spring elements in a yield strength mismatch situation with application to welded wide plates.

Paper II: Efficient fracture assessment of pipelines. A constrain-corrected SENT specimen approach.

Paper III: Closed form line spring yield surfaces for deep and shallow cracks: formulation and numerical performance.

Paper IV: Efficient numerical procedures for fracture assessments of surface cracked shells.

Paper V:An engineering methodology taking into account the effect of local damage on the global behavior of surface cracked shell structures.

Paper VI: Integrated local/global analysis and fracture assessment of pipelines with defects.

1 Introduction

The research council of Norway in connection with the oil industry has in the last decade financed many research projects through a forum called: "Stålmat". The present work has been carried out within a "Stålmat" project. One of the tasks of the project has been the introduction of steels with significantly higher strength in submarine pipelines.

During the last 20 years, steels with a yield strength exceeding 400MPa were increasingly used for offshore constructions. The requirement on structural steel plates for offshore structures differ because of varying field of application and location. Intensive research activities have been undertaken in order to supply standards for the qualification of structural steel with respect to reliability, easy fabrication process, safe service conditions and a fair price. The results of these activities have been of fundamental importance for meeting the new situation the oil industry is confronted with. Lately for example, new deep-water applications require steel with an even higher strength in order to decrease the weight of the bearing structure. Usually the time necessary to include the most recent results in the standardized assessment procedure is long (10-15 years). Therefore advanced expertise remains unutilized for far too long before it is finally taken into use. This slows obviously down the process required to develop new solutions. A need for taking into use the most recent knowledge, testing methodology and acceptance criteria for fracture assessment is dictated by the new challenges faced by the oil industry.

Products and structures are developed by using extensively computer programs. Finite element calculations are performed in order to verify that the structure is properly designed in order to guarantee an acceptable capacity with respect to failure. It is practice in structural calculation to perform numerical analysis by using a combination of beam and shell elements. The combination of beam and shell elements allow engineers to verify the integrity of the complete structure with respect to various extreme loading condition. A limitation with this kind of calculations is that the only tensile failure mode taken in to consideration is the one due to plastic collapse. In order to by-pass this intrinsic limitation a high conservatism is used in evaluating the numerical results. A more exhaustive description of the behavior of the structure by means of both failure modi and material behavior would allow a more effective use of material. In order to describe in detail the behavior of structures by means of finite element methods, a 3-dimensional analysis is needed. The use of solid finite element for structural analysis would lead to large size problems that are infeasible in most cases. Even though such analysis could be performed, the level of expertise required to evaluate the numerical results is often not available.

Advanced element formulations have to be used in order to connect complex material models to the finite element framework used for structural analysis. The present work presents a newly developed line spring finite element formulation used to account for cracks in shell structures. Linking these elements to shell elements, and further linking the shell elements to beam elements, one has a global model of the shell structure that also accounts for local flexibilities and

fractures due to defects. An important advantage with such an approach is the possibility of a direct fracture mechanics assessment e.g. via computed $J-$integral or $CTOD$. A recent development in this approach is the notion of two-parameter fracture assessment. This means that the crack tip stress tri-axiality (constraint) is employed in determining the corresponding fracture toughness, giving a much more realistic capacity of cracked structures.

The present work gives a short introduction on fracture mechanics theory, including two-parameter fracture assessment. Furthermore, a short presentation of the line spring finite element formulation is given. The main focus of this work is to develop a link between local material models and complex analysis. The work is presented by a series of papers:

- **Paper I** [1], addresses the performance of the line spring finite element utilized for describing a surface crack in a bi-material elastic plastic wide plate structure. Large scale test results are compared to the results obtained from both a 2D and 3D numerical analysis.

- **Paper II** [2],addresses the performance of shell and line spring finite elements as a cost effective tool for performing the numerical calculation needed to perform a so called "constraint corrected failure assessment". The proposed failure assessment is based on the testing of a constraint-corrected fracture mechanics specimen under tension. Such specimens are designed in so that their constraints are similar to that of the structure. In this way similar fracture mechanisms can be expected in both the specimens and the structure.

Paper I and **Paper II** highlight the limits of the line spring element implemented in the ABAQUS software and was the starting point for a further implementation of the line spring framework.

- In **Paper III** [3], accurate yield surfaces of plane strain single-cracked (SEC) specimens having shallow, as well as deep, cracks are developed in order to improve the overall performance of the line spring element. The yield surface is represented by equations that automatically satisfy the convexity requirement and that fit the result of the finite limit analysis. The performance of the backward-Euler return algorithm for an accurate yield surface formulated here is addressed by means of iso-error maps.

- In **Paper IV** [4] shell line spring calculations are performed by means of the newly developed line spring formulation in order to calculate the constraint level of a pipe with surface or through the thickness cracks. A single-edge-notched-tensile specimen (SENT) is designed to give a constraint level comparable to the one calculated for the pipe. The constraint corrected specimen is tested in order to obtain the crack-tip-opening-displacement ($CTOD$) versus the crack growth increment (Δa) curve. The $CTOD - \Delta a$ curve is implemented in the line spring formulation throughout an efficient numerical procedure. Ductile crack growth is taken into account in a proper manner.

- **Paper V** [5], presents a discussion around the meaning of the $J - integral$ when crack growth occurs. The $J - integral$ is regarded as a sort of accumulated measure of the

global deformation in the ligament. The complete Gurson [6] is used in order to support our observations. Furthermore a crack propagation law relating a local criterion for crack growth to the global deformation field is outlined. A methodology to link micromechanically based crack growth simulations with line spring analysis is proposed by suggesting an alternative way to calculate the $J - integral$ from the line spring framework.

- **Paper VI** [7], addresses nonlinear finite element analysis of pipelines subjected to e.g. large curvatures. Cracks are accounted for by means of a newly developed line spring finite element formulation. Linking these elements to shell elements, and further linking the shell elements to beam elements, one has a global model of the pipeline that also accounts for local flexibilities and fractures due to defects (in the welds).

2   Fracture mechanics theory

The aim of fracture mechanics is to provide engineers with a means to give quantitative estimates for the fracture resistance of cracked structure. Since the beginning of the 20th century the focus of much research has been on establishing mathematical expressions to characterize the stress and strain concentration ahead of a crack. The classical theory is based upon the assumption that the crack tip stress and strain field can be described by a single parameter. The single parameter scales the amplitude of a crack tip singularity and, when this singularity dominates over microstructural significant size scales, it serves to correlate crack initiation and growth.

The combination of plasticity and structural geometry limits the validity of the single parameter theory. In recent years one has introduced an alternative theoretical framework based on two different parameters. The first parameter scales the zone of the large stresses and strain and the second parameters scales the influence of geometry constraint on the near-tip stress.

2.1   Characterization of crack tip fields

2.1.1   Linear elastic crack tip fields

A number of solutions have been derived to describe the near tip fields for isotropic linear elastic materials. Westergaard [8], Irwin[9], Sneddon [10] and Williams [11] were among the first to publish such solutions. Employing polar coordinates (r, θ) centered at the crack tip, as shown in Fig 1, it can be shown that the stress field in any linear elastic cracked body is given by:

$$\sigma_{ij} = \left(\frac{K}{\sqrt{2\pi r}} \right) f_{ij}(\theta) + T\delta_{1i}\delta_{1j} + \text{higher order terms} \tag{1}$$

where σ_{ij} is the stress tensor, K is the stress intensity factor and f_{ij} is a dimensionless function of θ. The second term of Eq. 1 is the T-stress, it acts parallel to σ_{11} and it is independent of r and θ. The T-stress is depend on geometry. The higher order terms are an $\mathcal{O}(r^{1/2})$. Limiting attention to a small region surrounding the stress singularity ($\sigma_{ij} \rightarrow \infty$ when $r \rightarrow 0$) it is sufficient to retain only the first order term.

The asymptotic description of the stress field given in Eq. 1 represents the framework of the
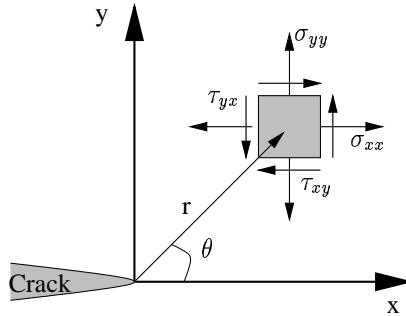
Figure 1: Definition of the coordinate axis ahead of a crack tip used for a two dimensional deformation field.

linear elastic fracture mechanics (LEFM). Linear elastic stress analysis of a sharp crack predicts an infinite stress at the crack tip. In real materials however the stresses are finite, because the crack tip radius must be finite. Inelastic material deformation, such as plasticity in metals, leads to further relaxation of crack tip stresses. While, in general, large-scale inelastic effects usually limit application of LEFM to the crack problem, K may still characterize the near-tip fields if the size of the zone where plastic effects prevail is small compared to other geometrical dimensions. Such a condition is usually referred to as *small scale yielding* (SSY). A concept of *boundary layer formulation* [12] and [13], has emerged to analyze the SSY problem. In the limit, when plastic region dimensions are negligible compared to other geometric dimensions, the surrounding elastic singularity sets the boundary conditions on the elastic-plastic boundary value problem. Thus, the SSY solution for mode I loading may be obtained by considering a semi-infinite cracked body see (Fig. 2) with displacements of the elastic singular field for (plane strain) mode I imposed on the outer circular boundary given by:

$$u(r, \theta) = K_I \frac{1+\nu}{E} \sqrt{\frac{r}{2\pi}} \cos\left(\frac{\theta}{2}\right) (3 - 4\nu - \cos\theta)$$

$$v(r, \theta) = K_I \frac{1+\nu}{E} \sqrt{\frac{r}{2\pi}} \sin\left(\frac{\theta}{2}\right) (3 - 4\nu - \cos\theta)$$

(2)

where ν is Poisson's ratio.

To the extent that SSY conditions prevail over sufficiently large length scales, the surrounding elastic crack tip stress fields are identical for different configurations if their stress intensity factors are equal, and thus if material properties are identical, the near tip stresses and deformations are also identical. Since the extent of the plastic zone in SSY under mode I loading is $r_p^{SSY} \approx (1/2\pi)(K_I/\sigma_Y)^2$, quantitative estimates of K-dominance (which ensure that the elastic singularity controls the local deformations) are given by the standards of the American Society for Testing of Materials (ASTM E-399), which require that

$$B, a, (h - a) \geq 2.5 \left(\frac{K_I}{\sigma_Y}\right)^2 \approx 16 r_p^{SSY}$$

(3)

$$\sigma_{ij} = \frac{K_I}{\sqrt{2\pi r}} f_{ij}(\theta)$$
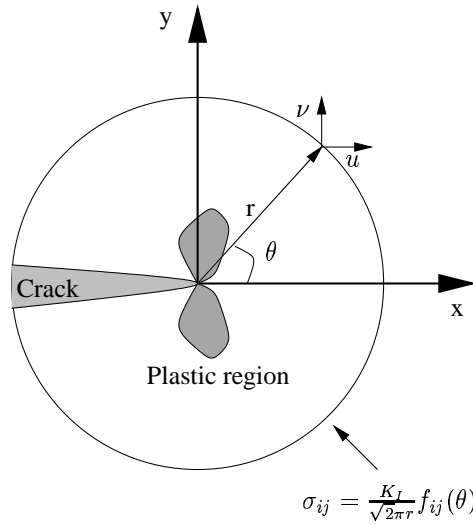
Figure 2: Small scale yielding model based on Rice's boundary layer formulation.

where σ_Y is the tensile yield stress, a is the crack size, h is the specimen width, $(h - a)$ is the uncracked ligament length and B is the specimen thickness.

2.2 Crack tip fields under elastic-plastic conditions

a) Displacement at the original
crack tip

b) Displacement at the inter-
-section of a $\frac{\pi}{2}$ vertex
with the crack flanks
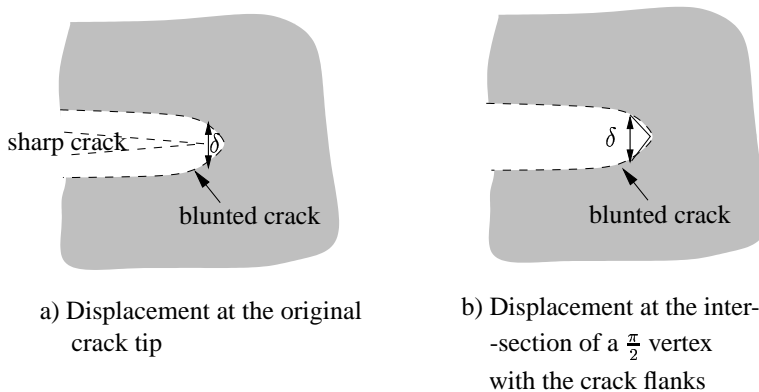
Figure 3: Alternative definitions of CTOD

For elastic-plastic conditions where the plasticity exceeds the limitation for valid use of the elastic parameter K, two different approaches are introduced for describing the crack tip conditions. The $CTOD$ introduced by Wells [14] and the $J-integral$ introduced by Rice [15] give a nearly size-independent measures of fracture toughness, even for relatively large amount of

crack tip plasticity. Limits for the amount of plasticity exist also in application of J and $CTOD$, however these limits are less restrictive than those for LEFM.

The $CTOD$ is based upon the assumption that the degree of crack tip blunting of fracture initiation is a measure of the fracture toughness. Two alternative definitions of $CTOD$ are alternatively used, see Fig. 3. The original $CTOD$ definition is the displacement at the original crack tip, Fig. 3a). Later Rice [15] suggested a $CTOD$ defined as the $\frac{\pi}{2}$ radians intercept, Fig. 3b), which is commonly used to introduce $CTOD$ in finite element analysis. If the crack blunts in a semicircle the two definitions are equivalent.

Using a strip yield model an expression for the $CTOD$ in an infinite plate subjected to tensile stress was derived as:

$$\delta = \frac{8\sigma_Y a}{\pi E} \ln \sec \left(\frac{\pi \sigma}{8 \sigma_Y} \right) \tag{4}$$

where σ_Y is the material yield strength and a half of the crack length. For $\sigma \ll \sigma_Y$ a relationship between K_I and $CTOD$ reads:

$$\delta = \frac{K_I^2}{M \sigma_Y E} \tag{5}$$

where M is a dimensionless constant that is approximately 1.0 for plane stress and 2.0 for plane strain conditions.

An alternative approach to non-linear characterization of the crack tip field was introduced by Rice [15]. Rice showed that the non-linear energy release rate, J, could be written as a path independent line integral by idealizing elastic-plastic deformation as non-linear-elastic. For large scale, but still limited, plasticity the line integral is defined as

$$J = \int_\Gamma \left(w dy - \sigma_{ij} n_j \frac{\partial u}{\partial x} ds \right) \tag{6}$$

where Γ is a contour surrounding the crack tip beginning at the bottom face of the crack and ending at the top face as shown in Fig. 4. w is the strain energy of the material defined as

$$w = \int_0^{\varepsilon_{ij}} \sigma_{ij} d\varepsilon_{ij} \tag{7}$$

n_j is the outward normal along Γ, u is the displacement vector and ds is an element of arc-length along Γ. Hutchinson [16] and Rice and Rosengren [17] independently showed that J characterizes the crack tip condition for a non-linear elastic material. They both assumed a Ramberg-Osgood stress strain relation where the elastic strain was neglected giving:

$$\frac{\varepsilon}{\varepsilon_0} = \kappa \left(\frac{\sigma}{\sigma_0} \right)^n \tag{8}$$

where σ_0 is a reference stress usually equal to the yield strength, $\varepsilon_0 = \sigma_0/E$ is the corresponding reference strain, κ is a dimensionless constant, and n is the strain hardening exponent.

An expression for the crack tip singular fields under mode I loading, which is now reffered to as the HRR (Hutchinson Rice and Rosengren) fields, is given by:

$$\sigma_{ij} = \sigma_0 \left(\frac{EJ}{\kappa \sigma_0^2 I_n r} \right)^{1/(n+1)} g_{ij}(\theta, n)$$

$$\varepsilon_{ij} = \frac{\kappa}{E} \sigma_0 \left(\frac{EJ}{\kappa \sigma_0^2 I_n r} \right)^{n/(n+1)} h_{ij}(\theta, n) \tag{9}$$
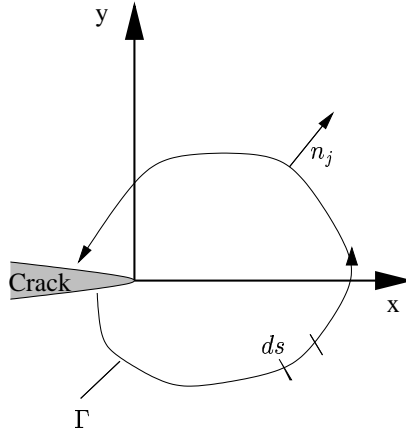
Figure 4: Crack in a two-dimensional deformation field with an arbitrary contour around the crack tip.

where I_n is an integration constant that depends on n and $h_{ij}(\theta, n)$ and $g_{ij}(\theta, n)$ are dimensionless function of n and θ. The J defines the amplitude of the HRR fields, just as the stress intensity factor K characterizes the amplitude of the linear elastic crack tip field. The $r^{-1/(n+1)}$ singularity of the HRR is also consistent with the $\frac{1}{\sqrt{r}}$ singularity for linear elastic material ($n = 1$). However the HRR field persists long after the linear elastic zone has been destroyed by crack tip plasticity.

As for the linear elastic fields the HRR singularity fields predict infinite stresses as $r \longrightarrow 0$. In reality large strains causes the crack tip to blunt, which reduce the stresses and the stress triaxiality locally. Large strain finite element analysis performed by McMeeking and Parks [18] indicates that the HRR field is not valid within a region approximately 2-3 times the crack tip opening displacement δ. However as long as there is a region surrounding the crack tip that can be described by Eq. 9, the J-integral uniquely characterizes the crack tip conditions, and a critical value of J is a size-independent measure of fracture toughness. The dominance of the HRR fields over a length of several crack tip opening displacements gives a unique relationship between the J integral and δ, expressed as [19]

$$\delta = d_n \frac{J}{\sigma_0} \tag{10}$$

where the crack tip opening displacement δ in this expression is defined as the opening distance at the interception of the crack flanks and a $\frac{\pi}{2}$ vertex, Fig. 3b). d_n is a dimensionless constant which exhibits a strong dependence on the strain hardening exponent n, and a moderate dependence on the reference strain $\varepsilon_0 = \frac{\sigma_0}{E}$. The radial distance from the crack tip over which the HRR field dominates is depending on loading, strain hardening and final geometry. Increased plastic deformation will gradually invalidate a HRR description of the crack tip field through loss of stress triaxiality. On the basis of finite element analysis, size requirements for HRR dominance were established by Shih and German [20] and McMeeking and Parks [18]. Such

requirements for obtaining J-controlled fracture initiation are usually given in the following form:

$$B, a, (h - a) \geq \nu_{cr} \frac{J}{\sigma_0} \tag{11}$$

where a is the crack size, h is the specimen width, $(h - a)$ is the uncracked ligament length, B is the specimen thickness and ν_{cr} is a dimensionless constant depending strongly on strain hardening n, weakly depending on $\frac{\sigma_0}{E}$ and also depending on loading condition. High hardening give less strict requirements than for low hardening. Reasonable values of ν_{cr} is from ≈ 200 for tension and from ≈ 25 for bending. Thus, bending gives high level of stress triaxiality and valid J-integral for smaller specimen and or larger amount of plastic deformation than tension.

2.2.1 Two and three parameter characterization of crack tip fields

In conventional fracture mechanics, it is assumed that crack tip stress field is controlled by a single parameter, as previously presented, and that the toughness obtained from tests with one specimen geometry can be transferred to structural applications. The factors that influence the transferability and invalidate the one-to-one relation between crack driving force J-integral and crack tip stress field is called constraint. In general, there are two types of constraints in a weld:

- the geometry constraint caused by crack size, specimen dimensions and loading mode;

- the material mismatch constraint due to inhomogeneous material properties.

These constraints may be characterized by the Q or T parameters (O'Dowd and Shih [21], Betegon and Hancock [22], Parks [26], Kirk and Bakker [27]) and the M-parameter (Ranestad et al. [24], Zhang et al [25]), respectively.

The constraints invalidate conventional fracture mechanics, i.e. for a given value of crack driving force J-integral, the crack tip stress field is influenced by the constraint level. Fig. 5a illustrates the geometry constraint effect on the crack tip stress field, where a reference solution given by the upper curve may be the HRR-field (i.e. a crack in an infinitely large specimen), whereas the lower curve is the actual stress field. Hence, there is no one-to-one relation between the crack driving force and crack tip stress field, and the fracture toughness obtained from one case cannot be directly transferred to another one.

For cleavage fracture occurring after significant plastic deformation, with attainment of a critical stress (normal or maximum principal stress) over a microstructurally relevant volume, the RKR (Richie-Knott-Rise) criterion see [28], is a feasible failure criterion. Brittle fracture initiates when a critical stress is reached in front of the crack tip over a sufficiently large distance. If this distance is given by point 2 in Fig.5a, then one sees that the stress field in a low constraint situation has reached the critical stress over a too small distance, point 1. This situation is illustrated in Fig.5b considering $J-$integrals. Here $J_{reference}$ is the $J-$integral that would exist in an infinitely large specimen with the same crack tip stress field as in the actual specimen. Fracture would initiate in a low constraint specimens for applied J equal to J_{cr1} or J_{cr2}. When these $J-$levels are reached, the RKR-criterion is fulfilled. Using the actual stress field (accounting for actual constraint), and comparing with the HRR stress field it is possible to determine what

a)

b)
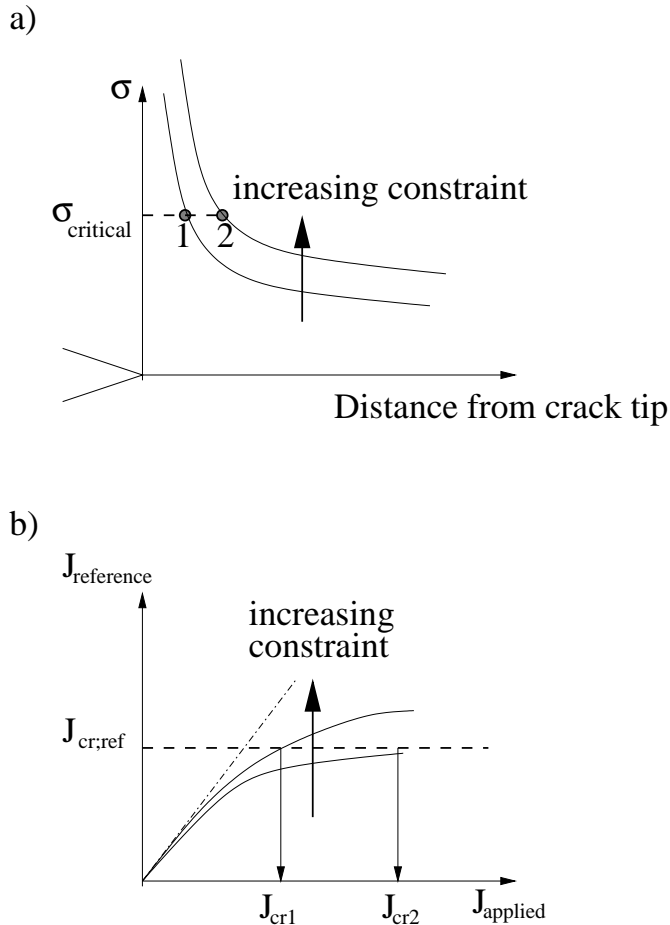
Figure 5: a) effect of constraint on crack tip stress field, b)relationship between applied J and reference J

magnitude of J-applied that is required to initiate fracture. Constraint influences the transferability and invalidate the one-to-one relation between crack driving force J and crack tip stress field. For specimens made of homogenous materials, the constraint is termed geometry constraint. It has been proposed that the stress field at different levels of geometry constraint can be characterized by the $J - Q$ theory, i.e. the J-integral and Q, a hydrostatic stress parameter see [21]. According to the $J - Q$ theory, the crack tip field inside the plastic zone can be separated into two parts. The first part is called reference field which is controlled by J-integral, i.e. the one-to-one relation between the J-integral and stress field is maintained in the reference field. The actual stress field is influenced by the constraint level at the crack tip. Therefore it modifies the reference field. This leads to a second stress field, called difference field, which is practically

controlled by the parameter Q. The complete stress field can therefore be written:

$$\sigma_{ij} = \sigma_{ij}^{ref} + Q\sigma_0\delta_{ij} \tag{12}$$

Within the modified boundary layer formulation, the $J - Q$ theory can be shown to be equivalent to the $J - T$ theory [23].

The material strength distribution in a real weld is complicated and certain simplifications of a weld crack problem are needed. For a specimen made of inhomogeneous materials with an interface crack, the observed fracture toughness of a reference material is obviously influenced by the mismatch properties of the material on the other side of the interface. For materials with identical elastic properties, there are three types mismatch: strength mismatch, hardening mismatch, and combination. Recently, extensive numerical studies have been carried out to investigate the effect of material mismatch constraint on the interface crack tip stress field of bi-material and tri-material boundary layer models. In the $J - Q - M$ formulation a general approximation for the difference field has been used, i.e. $\sigma_{i,j} = \sigma_{i,j}(r, \theta, J, Q, M)$, [24], [25], [29].

In order to relate $J_{reference}$ to fracture, an approach where the fracture is related to testing of weld thermal simulated $CTOD$ specimens has been applied, [30]. These specimens represents a homogenous microstructure of the most brittle part of the HAZ, hence the mismatch constraint, M, will be zero. For many steel materials, fracture after weld thermal simulation are experienced at a low $CTOD$, giving only a limited size of the plastic zone and little relaxation from the initial high constraint in small scale yielding. In this way $J_{reference}$ can be related to the failure of homogeneous microstructures and a specimen size where valid J results are obtained (e.g. under small scale yielding). A horizontal limit in Fig.5b can be chosen to represent the critical J experienced in weld thermal simulation testing, and the $J - Q - M$ approach is then used to transfer from this "ideal" situation to the actual weld under consideration.

3   A method for obtaining fracture mechanical parameters directly from a structural analysis

3.1   Elastic-Plastic Line-Spring finite element formulation
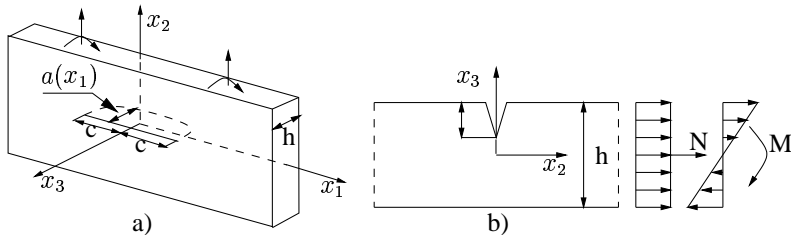
Figure 6: Part-trough-surface-crack and plane strain solution.

The part-through surface crack is originally a three dimensional problem as seen in Fig. 6a. The three dimensional problem is formulated within the context of two-dimensional plate or shell

theory with the part-cracked section represented as a line-spring. The line-springs take into account the additional flexibility due to the surface crack. The stiffness of the line-spring, with extensional and rotational degrees of freedom (δ, θ), is derived from a plane strain edge-cracked strip loaded in tension and in bending (N, M), see Fig.6b, i.e. mode I [32]. It is compatible with a two-dimensional plate or shell element with four nodes. A combination of shell and line spring elements enables us to describe the three dimensional part-through surface crack problem within the context of two-dimensional plate or shell theory.
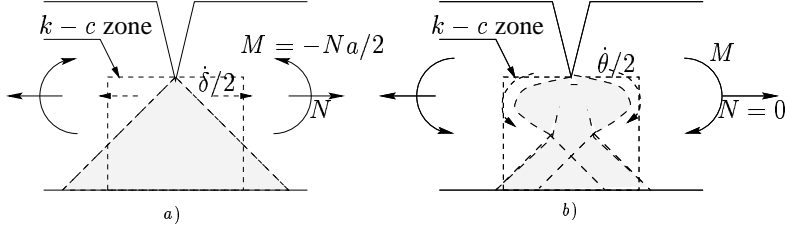
Figure 7: Slip line field approximation in the $kc - zone$. a) slip line solution for pure extension. b) Green Hundy solution for pure bending

The derivation of the elasto-plastic line-spring for the mode I case follows the classical plasticity theory. For plastic conditions, only the mode I case will be considered. It was solved for the line-spring in terms of the upper bound solution (slip line field, colored area in Fig. 7). The derivation of the mode-I line-spring follows the classical plasticity theory, [32] :

$$\phi(\mathbf{Q}, \sigma_Y^{LS}; a) = 0 \tag{13}$$

$$d\phi = \frac{\partial \phi}{\partial \mathbf{Q}} d\mathbf{Q} + \frac{\partial \phi}{\partial \sigma_Y} d\sigma_Y^{LS} = 0 \tag{14}$$

$$d\mathbf{q_p} = d\lambda \frac{\partial \phi}{\partial \mathbf{Q}} \tag{15}$$

when the yield condition is met Eq. 13, there will be plastic increment $d\mathbf{q_p}$ related to the yield function by normality rule Eq. 15. Additive split of elastic and plastic deformations in the ligament is assumed:

$$d\mathbf{q} = d\mathbf{q_e} + d\mathbf{q_p} \tag{16}$$

The plastic response of the line spring is governed by a yield surfaces having the crack depth as parameter. The yield surfaces implemented in ABAQUS [33] describe the plastic behavior of the rest ligament. These representations of the yield surface provide satisfactory results for a crack-depth-to-thickness ratio $\frac{a}{h} > 0.3$. In [3] an alternative yield surface which is able to univocally characterize the fully plastic yielding of both shallow and deep crack depths is proposed. The elasto-plastic constitutive law for the line-spring element reads:

$$d\mathbf{Q} = \mathbf{D_{ep}} \cdot d\mathbf{q} \tag{17}$$

11

where $\mathbf{D_{ep}}$ is the continuum elasto-plastic stiffness matrix for the line-spring element and reads:

$$\mathbf{D_{el}} = \left(\mathbf{D_{el}} - \frac{\left(\frac{\partial \phi^T}{\partial \mathbf{Q}}\mathbf{D_{el}}\right)^T \left(\frac{\partial \phi^T}{\partial \mathbf{Q}}\mathbf{D_{el}}\right)}{\frac{\partial \phi^T}{\partial \mathbf{Q}}\mathbf{D_{el}}\frac{\partial \phi}{\partial \mathbf{Q}} - \frac{\partial \phi^T}{\partial \mathbf{Q}}\mathbf{Q}\frac{\partial \phi}{\partial \sigma_Y^{LS}}\frac{E_p}{\sigma_y^{LS}k l^{n'}}} \right) \tag{18}$$

Parks and White [34], argue that the exponent n' of Eq. 18 is 2 and the k-factor of order unity, l is the length of the rest ligament and σ_Y^{LS} is the yield stress for the line spring. Note that k, l and n' are the quantities controlling the plasticity in the ligament region, $kc - zone$ in Fig 7. The representation of the yield surface proposed in this study, ϕ_{df}, is used here in order to describe the stress field of the line-spring. Having determined the plastic deformation increment, the crack-tip opening displacement is obtained from:

$$d\delta_p = du_p + \left(\frac{h}{2} - a \right) d\theta_p. \tag{19}$$

The validity of this relation was investigated by Lee and Parks, [35]. Their results show that for shallow edge cracks ($a/h \leq 0.2$), the relation is inaccurate, [35]. Employing the connection between the J_p and the Dugdale crack tip solution corrected for constraint, one has:

$$dJ_p = m\sigma_Y^{LS}d\delta_p \tag{20}$$

Here, m is a function of crack geometries and hardening characteristics. The total J integral may now be calculated:

$$J = J_e + J_p \tag{21}$$

As the edge-crack is the basic case for the line spring, computed values of J for a surface crack will be more accurate in the center compared to positions approaching the surface at the crack ends. Combining a computed $J-$integral with a measure of geometry constraint, initiation of fracture may be predicted. For the shell and line spring finite element model, a convenient way of determining constraint is by means of the $T-$stress. The $T-$stress is the second term in the asymptotic expansion of the elastic solution for the crack tip stress field by Williams see [11]. The T-stress has therefore been considered as an elastic parameter with a limited range of validity. Betegon and Hancock [22] have shown that the $T-$stress provides a good estimate of the constraint even beyond the elastic and small scale yielding regime. Lee and Parks [35] have proposed a method for calculating the $T-$stress for the shell-line-spring-mesh based on Sham's analytical work see [36]. By use of the membrane force and bending moment along the semi-elliptical crack front, the $T-$stress at any point along the crack front can be expressed, i.e. $T = T(a, N, M)$. Hence, a two-parameter fracture mechanics approach is possible with shell/line spring elements also.

References

[1] **Paper I:** Chiesa M., Skallerud B. and Thaulow C., Line spring elements in a yield strength mismatch situation with application to welded wide plates. To appear in *Engineering Fracture Mechanics*.

[2] **Paper II:** Chiesa M., Nyhus B., Skallerud B. and Thaulow C., Efficient fracture assessment of pipelines. A constrain-corrected SENT specimen approach. Engineering Fracture Mechanics 68, 527-547, 2001.

[3] **Paper III:** Chiesa M., Skallerud B. and Gross D., Closed form line spring yield surfaces for deep and shallow cracks: formulation and numerical performance. Submitted for publ. *Computers and Structures* 2000.

[4] **Paper IV:** Chiesa M., Skallerud B., and Nyhus B., Efficient numerical procedures for fracture assessments of surface cracked shells Presented at European Conference on Computational Mechanics

[5] **Paper V:** Chiesa M., Østby E., Skallerud B. and Thaulow C., An engineering methodology taking into account the effect of local damage on the global behavior of surface cracked shell structures. Presented at National Conference on Computational Mechanics

[6] Z.L. Zhang, C. Thaulow, J. Ødegård A complete Gurson model approach for ductile fracture Engineering Fracture Mechanics 67 (2) (2000) pp. 155-168.

[7] **Paper VI:** Skallerud B., Chiesa M. and Holmås T., Integrated local/global analysis and fracture assessment of pipelines with defects Presented at Offshore Mechanics and Artic Engineering

[8] Westegaard H. M., Bearing pressure and cracks. *Journal of applied mechanics*. 6, 49-53, 1939.

[9] Irwin G. R., Analysis of stress and strain near the end of a crack traversing a plate. *Journal of applied mechanics*. Vol 24, 361-364, 1957.

[10] Sneddon I. N., The distribution of stress in the neighbourhood of a crack in an elastic solid. *Proceedings, Royal Society of London*. Vol A187, 229-260, 1946.

[11] Williams M.L., On the Stress Distribution at the Base of a Stationary Crack. *J. Applied Mech*. Vol 24, 109-114, 1957.

[12] Rice J. R., Mechanics of crack tip deformation and extension by fatigue. *Fracture Toughness*. 247-311, Philadephia 1967. ASTM STP 415, American Society for Testing and Materials.

[13] Rice J. R. and Tracey D. M. Computational fracture mechanics. *Numerical and computer methods in Structural Mechanics*. 585-623, 1973.

[14] Wells A. A., Unstable crack propagation in metals: Cleavage and fast fracture. *Preceedings on the Crack propagation Symposium.* Vol1, 1961.

[15] Rice J. R., A path independent integral and the approximate analysis of strain consentration by notches and cracks. *Journal of Applied Mechanics.* 35, 379-386, 1968.

[16] Hutchinson J. W. Singular behavior at the end of a tensilecrack in a hardening material. *Journal of the Mechanics and Physics of Solids.* 16, 13-31, 1968.

[17] Rice J. R. and Rosengren G. F., Plane strain deformation near crack tip in a power law hardening material. *Journal of the Mechanics and Physics of Solids.* 16, 1-12, 1968.

[18] McMeeking R. M. and Parks D. M. On criteria for J-dominance of crack tip fields in large-scale yielding. *Elastic Plastic Fracture.* ASTM STP 668, 175-194, 1979. American Society for Testing and Materials.

[19] Shih C.F., Relations between the j-integral and the crack opening displacement for stationary and extending cracks. *Journal of the Mechanics and Physics of Solids.* 29, 305-326, 1981.

[20] Shih C.F. and German M.D,, Requirements for one parameter characterixation of crack tip field by the HRR singularity. *Internationa Journal of Fracture.* 21, 263-277, 1973.

[21] O'Dowd N. P. and Shih C. F., Family of crack tip fields characterized by a triaxility parameter-Part I,II. *J. Mech. Phys. Solids* 40 ,939-963, 1995.

[22] Betegon C., and Hancock J.W., Two-parameter characterization of elastic plastic crack-tip fields. *J. Appl. Mech.* 58, 104-110, 1991.

[23] Shih C. F. and O'Dowd N. P. A Fracture Mechanics Approach based on a Toughness Locus. In Dawes, M.G. (ED.), *Shallow Crack Fracture Mechanics, Toughness Tests and Applications.* The Welding Institute. Publishing, Abington Cambridge, U.K., 1992

[24] Ranestad Ø., Zhang Z. L. and Thaulow C., Two-parameter (J-M) description of crack-tip stress-fields for an idealised weld in small scale yielding. *Int. J. of Fracture* 2000.

[25] Zhang Z. L., Thaulow C. and Hauge M., Effects of crack size and weld metal mismatch on the HAZ cleavage toughness of wide plates. *Engineering fracture mechanics* 57 , 653-664, 1997.

[26] Parks D. M., Advances in characterization of elastic-plastic crack tip fields. Topics in fracture and fatigue *J. Press. Vessels Tech.* 104, 287-292, 1992.

[27] Kirk M., and Bakker A. Constraint effects in fracture and application. second volume *ASTM STP 1244, Philadelphia.*

[28] Ritchie R. O., Knott J. F. and Rice J. R., On the relationship between critical tensile stress and fracture toughness in mild steel. *J. Mech. Phys. Solids* 21 , 395-410, 1973.

[29] Zhang Z. L., Hauge M. and Thaulow C. Two-parameter characterization of the near tip stress fields for a bi-dimensional elastic-plastic interface crack. *Int. J. Fracture.* 79 , 65-83, 1996.

[30] Thaulow C., Hauge M., Zhang Z. L., Ranestad Ø. and Fattorini F. On the interrelationship between fracture toughness and material mismatch for crcaks located at the fusion line of weldments *Engineering Fracture Mechanics* 64, 367-382, 1999.

[31] Rice J., and Levy N. The part through surface crack in an elastic plate. *J. Applied Mech.* 185-194, 1972.

[32] Rice J. R., The line spring model for surface flaws. *The Surface Crack Physical Problems and Computer Solutions*. (ed J. L. Sweldow), ASME 1972.

[33] Hibbit Karlson and Sorenson., ABAQUS Manual, version 5.2.

[34] Parks D. M. and White, C. S., Elastic-plastic line spring finite elements for surface cracked plates and shells . *J. Press. Vessel Tech*. 104, 287-292, 1982.

[35] Lee, H. and Parks D.M., Enhanced elastic-plastic line spring finite element. *Int. J. Solids Struct.* 32 , 2393-2418,1995.

[36] Sham T.L., The determination of the elastic T-term using higher order weight functions. *Int.J. Fracture.* 48 , 81-102, 1991.

[37] Skallerud B., A mixed mode I/II inelastic line spring. *Int. J. Solids Struct.* 33 , 4143-4166,1996.

[38] Skallerud B., Numerical analysis of cracked inelastic shells with large displacements or mixed mode loading. *Int. J. Solids Struct.* 36 , 2259-2283,1999.

Line spring elements in a yield strength mismatch situation with application to welded wide plates

Matteo Chiesa[1], Bjørn Skallerud and Christian Thaulow

Department of Mechanical Engineering, NTNU, Trondheim, Norway

Key words: shell finite elements, line springs, solid finite elements, plasticity, cracked shells, yield stress mismatch

Abstract. *Higher utilization of structural materials leads to a need for accurate numerical tools for reliable prediction of structural response. Analysis with line spring finite elements is efficient in performing approximate fracture mechanics analysis of surface cracked shells. The present study addresses the performance of the line spring finite element utilized for describing a surface crack in a bi-material elastic plastic wide plate structure. Some outlines for the application of the line spring in a yield strength mismatch situation are obtained from a parameter study, and utilized for the 2D discretization of welded wide plates. Large scale test results are compared to the results obtained from both a 2D and 3D numerical analysis.*

1 Introduction

Shell structures with defects occur in many situations, for example in pipelines, pressure vessels and offshore platforms. The defects are usually introduced during the welding process necessary for joining different parts of the structure. Weldments are often the most critical part of a structure with regard to unstable fracture. Proper design and selection of material are of vital importance to structural integrity. Current fabrication practice in the industry adopts an approach based on a weld metal yield stress overmatch (with respect to the base metal). The overmatch weld has the advantage of increasing structural capacity (with cracks in the weld metals) for shallow and medium size cracks, and thus improving the welded joints resistance to failure. The steel usually employed is very ductile. As a consequence, the cracked shell allows

---

[1]Author to whom all correspondence should be addressed.

significant deformation without or before fracturing. In order to check the capacity, nonlinear fracture mechanics can be utilized, typically by means of the *J-integral* or the crack tip opening displacement *CTOD* supplemented by a parameter measuring the constraint in the crack tip region. A methodology based on *T-stress* or *Q-parameter* has been developed, see (O' Dowd and Shih I, II). The *J-Q* methodology quantifies the dependence of the crack tip stress field on the geometry when a homogeneous material system is considered. Such a methodology has been further developed to take in to account the effect of the material mismatch on the stress field by means of an extra parameter M, see [9]. The aim of the *J-Q-M* approach is to determine the fracture toughness of weldments in small scale fracture mechanics specimens and then transfer the results to structural components.

The direct discretization of the cracked shell structure with solid finite elements in order to compute the fracture mechanics quantities leads to large size problems, and makes such analysis infeasible in structural application, see [8]. In order to calculate the fracture mechanics parameters directly in a structural analysis, it is possible to use a combination of shell and line spring finite elements instead of solid finite elements. The number of degrees of freedom is reduced in this way by one order of magnitude compared to the 3D case. The accuracy of this approximation seems to be satisfactory from an engineering point of view. This approach has earlier been utilized for homogeneous materials, see [2]. The present study addresses the performance of inelastic shell finite elements combined with line springs when utilized to calculate the response of inhomogeneous structures where the defect is located in the weld metal. Some outlines for the calibration of the line spring in a bi-material case are given and utilized for the numerical discretization of the wide plates tested. The test-data are compared to the results obtained from both 2D and 3D model of the considered geometry.

2 Backgroun on tests and numerical simulations

2.1 Experimental program

As part of the work in the European project ACCRIS (Acceptance criteria and level safety for high strength steel weldments), twelve welded wide plates with a thickness of 70mm have been tested at $-10°C$, [18]. The material tested was a Thermo Mechanical Controlled Process (TMPC) steel with a yield strength of 500 MPa. The plates were oxygen torched into 750 mm wide panels by the manufacturer. FLUXOCORD 41-OP121TT was used as the welding consumable for the overmatch weld. The weld method used was Submerged Arc Welding (SAW). The welding position was horizontal and its direction was the same as the original rolling direction of the plate. After the welding, the panels were cut into test plates by oxygen torching, the cap layer of the welds and the edge of the Wide Plates were machined flush with the adjacent surfaces. The depth of the fatigue cracks was predetermined to be approximately 20mm deep. A notch was prepared by Electro Discharged Machining (EDM). The EDM notch was machined 2 mm shorter than the intended final depth of the fatigue crack. Cyclic loading of the wide plates in three-points-bending produced the fatigue start-cracks for the fracture mechanical test. The bending was performed in a 2.5 MN dynamic compression-testing machine run under constant

Table 1: Material Properties ($E = 210000$MPa $\nu = 0.3$).

PARAMETERS	BASE MATERIAL	WELD MATERIAL	HAZ
σ_Y	506 MPa	643 MPa	566 MPa
hardening n	0.065	0.07	0.07

amplitude load control at a frequency of 0.7 Hz. The crack extension was controlled by monitoring the reduction of the plate compliance. The large scale test was performed on SINTEF's Large Scale test machine. The test specimens were welded between the frames which were pushed apart by four hydraulic cylinders with a stroke of 500mm. Each cylinder can deliver a maximum force of 100MN. The following parameters have been monitored during the test: *force* and *displacement* for each cylinder,*specimen elongation*, crack Mouth Opening Displacement *CMOD*, the *strain* in the base and weld metal. After the test the following properties were calculated: **Gross Stress [MPa]**: the sum of load at the 4 cylinders of the test machine divided by the specimens cross-section. **Specimen Elongation [mm]**: the average of the displacements measured by the transducers installed . **Specimen Strain [%]**: the average of the displacements measured by the transducers installed divided by the measuring length (750mm).

2.2 Shell and line spring finite element formulation

All of the FE analysis were carried out with ABAQUS software. An eight-noded iso-parametric thick shell is used. This element is formulated for the Green-Lagrange strain and the conjugate 2. Piola-Kirkoff stress measure, and it is intended for large rotation with small or moderate strains [1]. In the analysis, deformation plasticity has been applied for the shell elements, with small strain theory characterized by the Ramberg-Osgood material model.

$$\frac{\varepsilon}{\varepsilon_Y} = \frac{\sigma}{\sigma_Y} + \alpha \left(\frac{\sigma}{\sigma_Y} \right)^{1/n} \tag{1}$$

In the above equation σ_Y is the yield stress parameter, n is the plastic hardening exponent,ε_Y is the yield strain and α is the "yield" offset [1]. The line spring elements are only implemented for linear geometry under small deformation. The only nonlinearity entering the system of equations is due to plasticity. Effects of large displacements has been investigated in [15].

The part-through surface crack is originally a three dimensional problem as seen in Fig. 1a. The three dimensional problem is formulated within the context of two dimensional plate or shell theory with the part-cracked section represented as a line spring. The line springs take into account the additional flexibility due to the surface crack. The stiffness of the line spring, with extensional and rotational degrees of freedom (u, θ), is derived from a plane strain edge-cracked strip loaded in tension and in bending (N, M), see Fig.1b, i.e. mode I [12]. The elastic stiffness is determined by the energy release rate combined with the known solutions for the stress intensity factor:
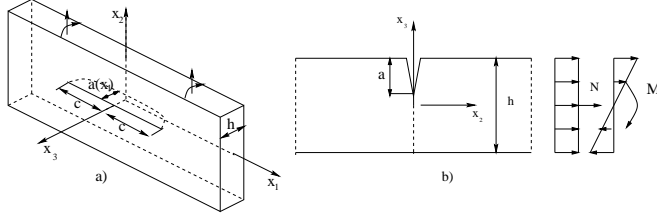
$$\mathbf{Q} = \mathbf{D_{el}q} \tag{2}$$

Figure 1: part trough surface crack and plane strain solution

$$\mathbf{Q} = [\mathbf{N}, \mathbf{M}]^{\mathbf{T}}, \quad \mathbf{q} = [\mathbf{u}, \theta]^{\mathbf{T}} \tag{3}$$

The additional deformation due to the crack $\mathbf{q}$ is determined from the structural equation system, and from these the force transmitted at the cracked shell section are obtained. For plastic condition, only the mode I case will be considered. It has been solved for the line spring in terms of upper bound solution (slip line field, colored area in Fig 2). A mixed mode I/II solution inelastic line spring based on a lower bound solution has been derived by Skallerud [13]. The derivation of the mode I line spring follows classical plasticity theory,[12] :

$$\phi(\mathbf{Q}, \sigma_{\mathbf{Y}}^{\mathbf{LS}}; \mathbf{a}) = \mathbf{0} \tag{4}$$

$$d\phi = \frac{\partial \phi}{\partial N}dN + \frac{\partial \phi}{\partial M}dM + \frac{\partial \phi}{\partial \sigma_Y}d\sigma_Y^{LS} = 0 \tag{5}$$

$$d\mathbf{q_p} = d\mathbf{q}\frac{\partial \phi}{\partial \mathbf{Q}} \tag{6}$$

$$d\mathbf{q_p} = d\mathbf{q_e} + d\mathbf{q_p} \tag{7}$$

$$d\mathbf{Q} = \mathbf{D_{ep}} \cdot d\mathbf{q} \tag{8}$$

$$d\mathbf{Q} = \left(\mathbf{D_{el}} - \frac{\left(\frac{\partial \phi^{\mathbf{T}}}{\partial \mathbf{Q}}\mathbf{D_{el}}\right)^{\mathbf{T}} \left(\frac{\partial \phi^{\mathbf{T}}}{\partial \mathbf{Q}}\mathbf{D_{el}}\right)}{\frac{\partial \phi^{\mathbf{T}}}{\partial \mathbf{Q}}\mathbf{D_{el}}\frac{\partial \phi}{\partial \mathbf{Q}} - \frac{\partial \phi^{\mathbf{T}}}{\partial \mathbf{Q}}\mathbf{Q}\frac{\partial \phi}{\partial \sigma_{\mathbf{Y}}^{\mathbf{LS}}}\frac{\mathbf{E_p}}{\sigma_{\mathbf{y}}^{\mathbf{LS}}\mathbf{kc}^{\mathbf{n'}}}} \right) d\mathbf{q} \tag{9}$$

Parks and White, (1982), argue that the exponent n' of Eq. 9 is 2 and the k-factor of order unity. c is the length of the rest ligament and σ_Y^{LS} is the yield stress for the line spring. Note that k, c, n' are the quantities controlling the plasticity in the ligament region, $kc - zone$ in Fig 2. The material properties in the $kc - zone$ need special consideration when a weldment is considered. Fig. 2 shows a simplified picture of the stress field in the $kc - zone$ under flow condition as a result of a slip line analysis. The $kc - zone$ is in our case heterogeneous, see Fig.2, it contains different materials with different properties. The yield surface employed here is based on an upper bound slip line solution [12], as implemented in ABAQUS, see [1]. Defining $X = \frac{\sqrt{3}N_I}{2\sigma_Y^{LS}(t-a)}$ and $Y = \frac{\sqrt{3}}{2\sigma_Y^{LS}(t-a)^2}(M_I + t/2N_I)$ the yield function implemented reads:

$$\phi_1 = (X - 0.3)^2 + 4.41(Y\frac{X}{2})^2 - 0.49 = 0 \quad for \quad X \leq 2Y \tag{10}$$

$$\phi_2 = \alpha_1 X + \alpha_2 Y + \alpha_3 X^3 Y + \alpha_4 X Y^3 - 1 \tag{11}$$

Slip line solution for pure extension

Green Hundy solution for pure bending
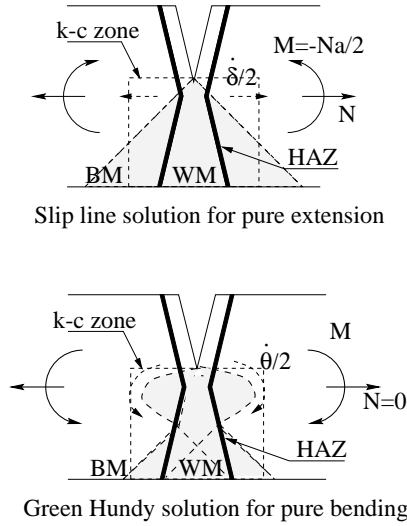
Figure 2: Slip line field approximation in the $kc - zone$.

The yield surface describes the plastic behavior of the $kc - zone$. The yield stress value chosen in the heterogeneous case will strongly influence the plastic behavior in the $kc - zone$. The understanding of this influence is the main goal of the present study.

Having determined the plastic deformation increment, the crack tip opening displacement is obtained from slip line kinematics which describe

$$d\delta_p = du_p + \left(\frac{t}{2} - a \right) d\theta_p. \tag{12}$$

The validity of this relation has been investigated by Lee and Parks, (1993 I). Their results show that for shallow edge cracks ($a/t \leq 0.2$) it becomes inaccurate, [3]. Employing the connection between the J_p and the Dugdale crack tip solution corrected for constraint, one has:

$$dJ_p = m\sigma_Y^{LS} d\delta_p \tag{13}$$

Here, m is a function of crack geometries and hardening characteristics. The total J integral may now be calculated:

$$J = J_e + J_p \tag{14}$$

As the edge crack is the basic case for the line spring, computed values of J for a surface crack will be more accurate in the center compared to positions approaching the surface at the crack ends.

3 Results

3.1 Discretization

Fig. 3 illustrates the 2D and 3D FE mesh for the welded wide plates tested. Due to the symmetries of the plates only one half is modeled, with no allowance for transversal motion or rotation of the nodes along the system line. In the shell-line-spring FE-model, on the left hand side of

Figure 3: A 2D FE mesh [on the left hand side] is compared to a 3D FE mesh

Fig. 3, there are 1240 nodes 468 8-node shell elements and 36 line spring elements. The weldment is located in the finest part of the mesh and the surface crack is located in the middle of the weldment. A fine element mesh is chos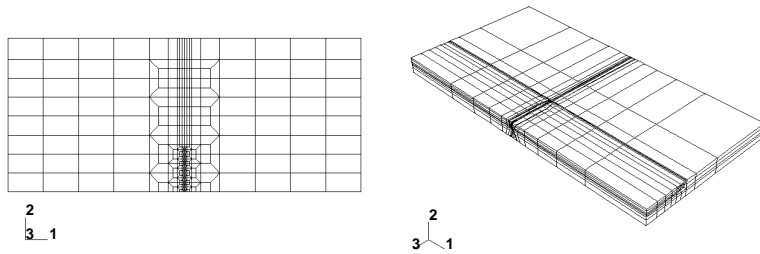en here to be able to describe the inhomogeneities of the system. In the solid FE-model, on the right hand side of Fig. 3, there are 5893 nodes and 4770 4-node solid elements. The cpu-time needed to complete the analysis is five times higher for the 3D-analysis than for the 2D one.

3.2 Line spring yield stress sensitivity

The 3D model Fig. 3 is designed to comply with the 70mm thick plate test specimen with X-groove weld, [17], [18]. The crack is a surface crack located in the middle of the X-groove weld. The relative crack depths is $a/t \approx 0.3$, the crack width to shell thickness ratio is $2c/t \approx 3.75$, and the crack length to the plate-width ratio is $c/W \approx 0.2$. The area of the crack is small compared to the intact part of the plate.

The different spatial material properties are taken into account in the 3D model through the thickness. The description of the X-groove in the 2D case would need a varying description of material characteristics through the thickness of the shell element. In order to avoid such a problem, a pragmatic methodology is used to calibrate our 2D model. The magnitude of the area characterized by the weld metal and the weighted area of the heat affected zone (colored zone in Fig. 4) is chosen to be the same in both the 3D case and in the 2D model.

The calibration of the yield strength in the line spring is important in order to obtain a reliable description of the ligament plasticity. This can be seen from the dependency of the plastic stiffness matrix, eq. 9, on the line spring yield strength, σ_Y^{LS}. For the cases analyzed herein, the cracks are located in the weld material. Hence, the line springs are located in the weld metal.
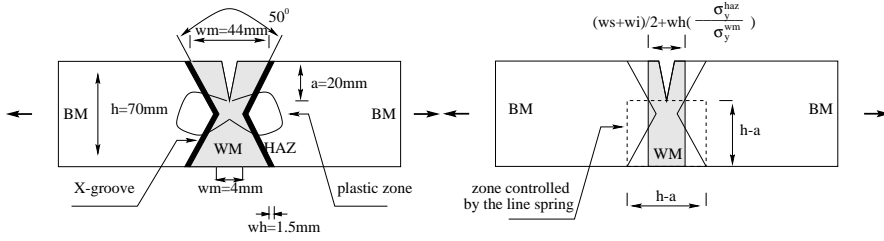
Figure 4: Representation of the weldment in the 3D and 2D case

They are therefore initially calibrated as $\sigma_Y^{WM} = \sigma_Y^{LS} = 643 MPa$, $n = 0.07$. The stress-displacement curve obtained from this analysis is compared to the curve obtained by calibrating the line springs with the properties of the base material $\sigma_Y^{BM} = \sigma_Y^{LS} = 506 MPa$, $n = 0.07$. The material properties of the two analyses are otherwise identical. Furthermore, k and n' are as implemented in ABAQUS [1] (Eq. 9). The stress-displacement curve seems to be only slightly dependent on the way the line spring is calibrated as seen in Fig. 5. This is due to the fact that such a curve represents the macroscopic behavior of the test specimen and does not describe the local behavior at the crack tip. When the mismatch relation $\frac{\sigma_Y^{WM}}{\sigma_Y^{BM}}$ is increased from an under-match to an overmatch situation the structural resistance is increased. This is a well
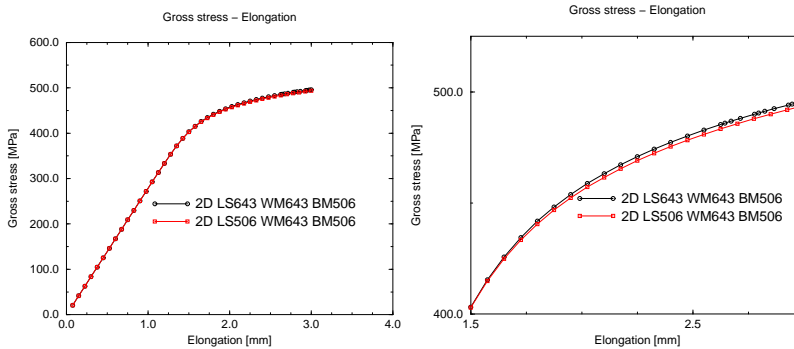
Figure 5: Gross Stress vs Elongation curves.

known phenomenon which is the basis for the over-match approach currently adopted as a fabrication practice in the industry. A parameter study has been carried out in order to see if the line springs describe such behavior.Gross Stress vs Displacement curves for four different yield stress mismatch situation, see table 2, are plotted in Fig. 6. The behavior is well described by the 2D-model as seen in Fig.6. The stress-displacement curves are moving upwards to an upper boundary limit which describes the situation in which the yielding is confined to the base metal.

The local non-linear behavior of the material at the crack front can be described by different parameters such as: $CMOD$, $CTOD$, J. In this study $CMOD$ is preferred to the other two parameters because it is the one directly obtained from the large scale test.

Table 2: Parameter study in which different strength mis-match situation are considered. ($E = 210000$MPa $\nu = 0.3$).

CASES	BASE MATERIAL[BM]	WELD MATERIAL[WM]	LINE SPRING[LS]
Even-match	$\sigma^{BM} = 506$ MPa	$\sigma_y^{WM} = 506$ MPa	$\sigma_y^{LS} = 506$ MPa
Under-match	$\sigma^{BM} = 506$ MPa	$\sigma_y^{WM} = 450$ MPa	$\sigma_y^{LS} = 450$ MPa
Over-match	$\sigma^{BM} = 506$ MPa	$\sigma_y^{WM} = 650$ MPa	$\sigma_y^{LS} = 650$ MPa
Over-match	$\sigma^{BM} = 506$ MPa	$\sigma_y^{WM} = 650$ MPa	$\sigma_y^{LS} = 750$ MPa
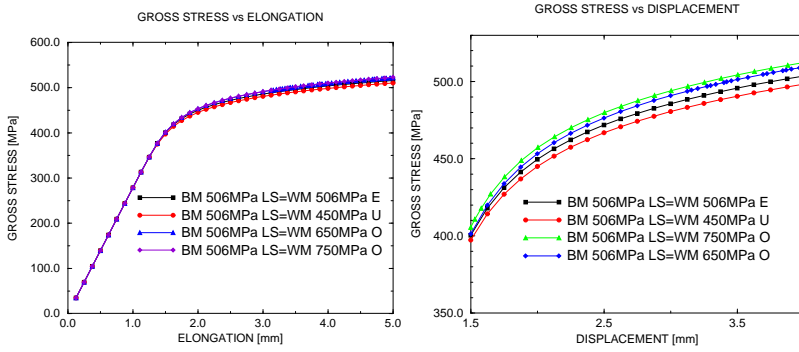
Figure 6: Gross Stress vs Displacement curves for different strength mis-match situation, see table 2.

$CMOD$ is very sensitive to the calibration of the line spring as seen in Fig. 7 where the results of a parameter study similar to the one of Fig. 5 and Fig. 6 are presented. The trend described by Fig. 7 is similar to what we have previously observed in Fig. 6: a higher overmatch leads to an increase in the ligament stiffness, and finally to a completely elastic ligament.

3.3 Plane strain edge-cracked strip model

In order to evaluate if the structural capacity increase is correctly described by the curves presented in Fig. 7 a further study on the $CMOD$ is carried out. An axially loaded plane strain edge-cracked strip model is considered. Fig. 8 represents the FE model for the problem. Two different numerical analyses of the plane strain edge-cracked strip model are carried out. The scope of these analyses is to compare the different local parameters in order to have a better understanding of what influences each of them. Two different material calibrations are used in this study: a single material calibration, where weld metal properties are used $\sigma_y^{WM} = 643 MPa$, $n = 0.07$ all over, and a bi-material material calibration with weld metal, $\sigma_y^{WM} = 643 MPa$, $n = 0.07$, and $\sigma_y^{BM} = 506 MPa$, $n = 0.065$. At the crack tip [local level] the two models are the same both from a geometrical and a material point of view. Fig. 9a) depicts $CTOD$ versus the J integral. There is a linear relation between $CTOD$ and J. This shows the direct relationship
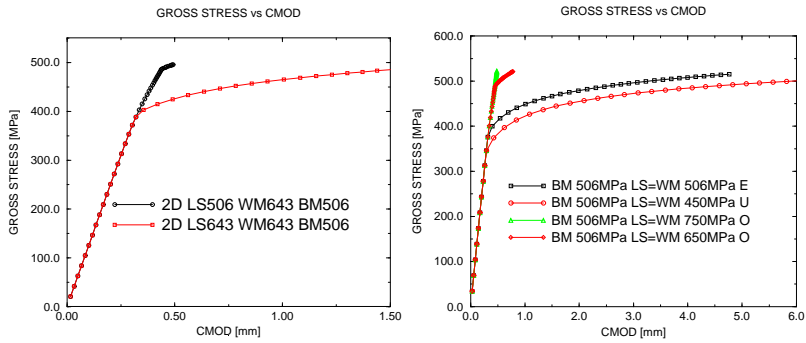
Figure 7: Gross Stress vs CMOD curves. The plot on the left hand side corresponds to the one in Fig. 5; and the one on the right hand side corresponds to the one in Fig. 6.

Figure 8: FE mesh for a plane strain edge-cracked strip model

Figure 9: J vs CTOD, CMOD curves

between the physical deformation described by $CTOD$ and the fracture mechanics parameter J. This linear relation between $CTOD$ and J underlines that $CTOD$ can be regarded as a
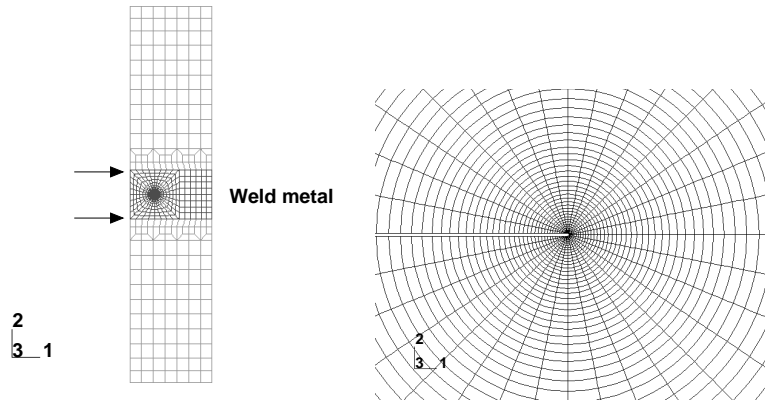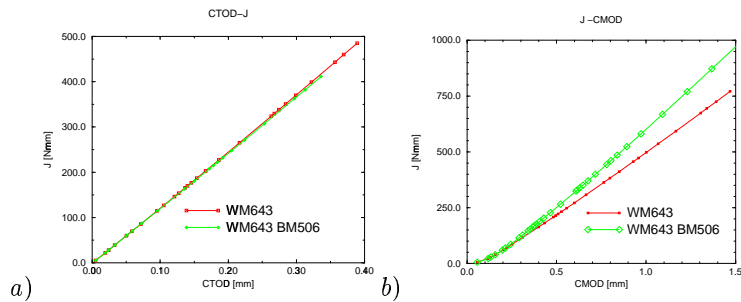
toughness criterion. Furthermore the curves for the two different material calibrations merge. This illustrates that the $CTOD$ and the J are two similar local parameters which describe the same local phenomenon. Fig. 9b) shows the relation between $CMOD$ and J. The $CMOD - J$ curves separate at increment number seven when the stress conditions in the specimen for the two cases start to differ, see Fig. 10. Weld metal and base metal behave in an elastic manner
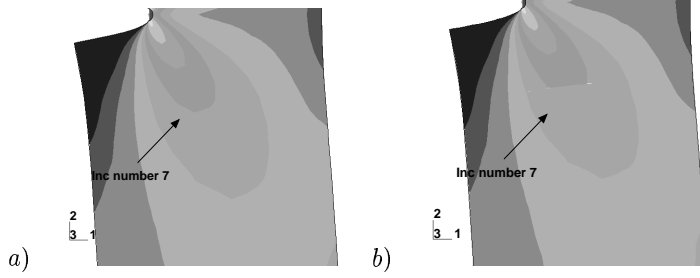
Figure 10: The Mises-stress distribution at the crack tip for the two cases (WM, WM-BM)

up to increment number six at which the stress distribution in the specimen is similar for both cases. At a further deformation increment the base metal starts yielding while the weld metal still behaves in an elastic manner, see Fig. 10. This leads to a different stress distribution in the specimen. The stress distributions at the crack tip seem however to be the same. Hence it can be stated that the $CMOD - J$ includes global effects compared to $CTOD - J$.

3.4 Outline for the calibration of the line spring

The results presented in the previous sections show how the yield stress calibration of the line springs influences the numerical results. In Fig 4, a qualitative picture of the plastic zone has been drawn. How the global stress distribution influences the different fracture mechanics parameters has been discussed. A reliable prediction of the stress distribution at the crack tip is the first step to obtain representative fracture mechanics parameters. The yield function which characterizes the plastic behavior of the line spring is derived from the slip line solution that assumes yielding through the rest ligament c. In other words, the stress distribution at the crack tip is dictated by the line spring element (see Fig. 4 and $kc - zone$ in Fig. 2). When the rest ligament is greater then the width of the weld metal $c > \frac{1}{2}(w_s + w_i) + w_h(\frac{\sigma_Y^{HAZ}}{\sigma_Y^{WM}})$ the line springs are calibrated with the same properties as the base metal. The width of the weld zone for the 2D model is calculated by equating the area of the weld metal in the 3D model, A_1, to the area of the weld metal in the 2D model, A_2:

$$A_1 = A_{WM} + A_{HAZ}\frac{\sigma_Y^{HAZ}}{\sigma_Y^{WM}} = A_2 \tag{15}$$

$$\frac{1}{2}(w_s + w_i)h - A_{cr} + 2(w_h * h)\frac{\sigma_Y^{HAZ}}{\sigma_Y^{WM}} = b * h - A_{cr} \tag{16}$$

$$b = \frac{(w_s + w_i)}{2} + 2w_h\frac{\sigma_Y^{HAZ}}{\sigma_Y^{WM}} \tag{17}$$

10

Gross stress – Elongation
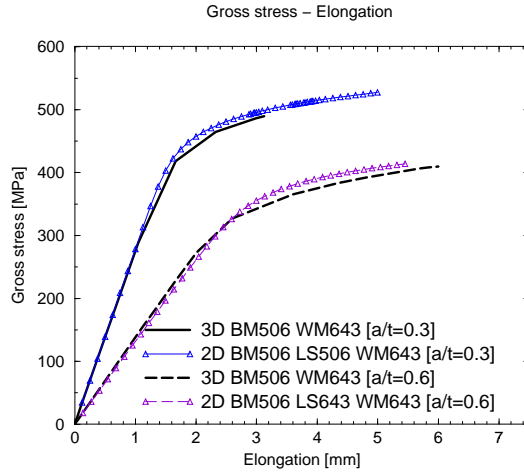
Figure 11: Gross Stress vs Displacement for the 2D and 3D analysis
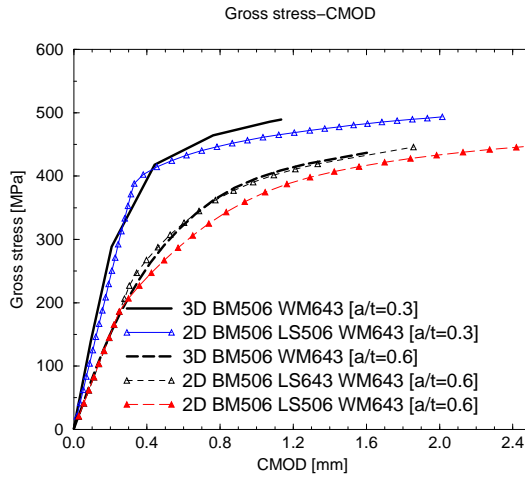
Gross stress–CMOD

Figure 12: Gross Stress vs CMOD for the 2D and 3D analysis

where w_s and w_i is the largest and smallest side of the X-groove, w_h is the width of the HAZ, A_{WM} and A_{HAZ} are the area of the weld material and of the heat affected zone respectively, and A_{cr} is the area of the crack, see Fig 4. In this way the size of the HAZ can be also taken in to account. In our case the influence of the weighted HAZ size is so small that it may be neglected.

The Gross Stress vs Displacement and the Gross Stress vs CMOD for the wide plate with two different relative crack depths $a/t \approx 0.3$ and 0.6 are plotted in Fig. 11 and 12. The rest ligament is greater than the width of the weld metal for $a/t \approx 0.3$, therefore the line springs are calibrated

11

with the same properties as the base metal, while for $a/t \approx 0.6$ the line spring is calibrated with the properties of the weld since the rest ligament is smaller than the width of the weld metal. The agreement becomes worse when the shell-line-spring model for $a/t \approx 0.6$ is calibrated in the same way as for $a/t \approx 0.3$ see Fig. 12.

It should be noted that the line spring yield stress is kept constant along all of the crack width. This is reasonable due to the low aspect ratio a/c for the cracks analyzed. In the line spring element at the end of the crack this introduces a small inaccuracy. For cracks with larger crack front curvatures this has to be accounted for.

The given outline is used in order to predict Stress-Displacement and Stress-CMOD curves for the wide plates tested where the HAZ zone is small compared to the weld and to the base metal.

3.5 Comparison with large scale tests

Figure 13: Gross Stress vs Displacement.Data from two tests are plotted and compared to data obtained from the 3D-model [see table 1 for the material calibration of the 3D model] and from the 2D-model [$\sigma_y^{WM} = 643MPa$, $\sigma_y^{BM} = \sigma_y^{LS} = 506MPa$]

The large scale test was performed on SINTEF's Large Scale test machine as described previously. The magnitude of the maximal axial load was $P \approx 30$MN. The material data used to calibrate the numerical model were obtained from tensile tests of the BM, HAZ, WM at different sampling position. The test data from the plates with the smallest amount of ductile crack growth ,$\approx 1mm$, are compared to the data obtained from the numerical analysis which does not take into account crack growth. The tests failed in brittle fracture at an elongation of 2.3 and $4mm$ respectively. The Stress-Displacement and the Stress-CMOD curves from the large scale test are plotted together with the curves obtained from the numerical analysis. In our case the size of the rest ligament is $c = 50mm$, the size of the weld metal zone for the 2D model

12
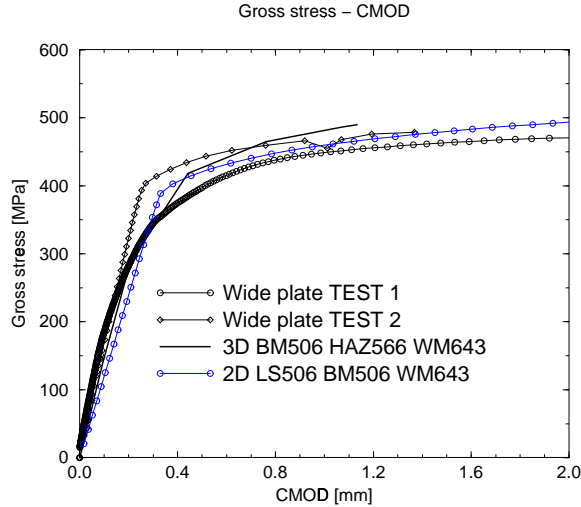
Gross stress − CMOD

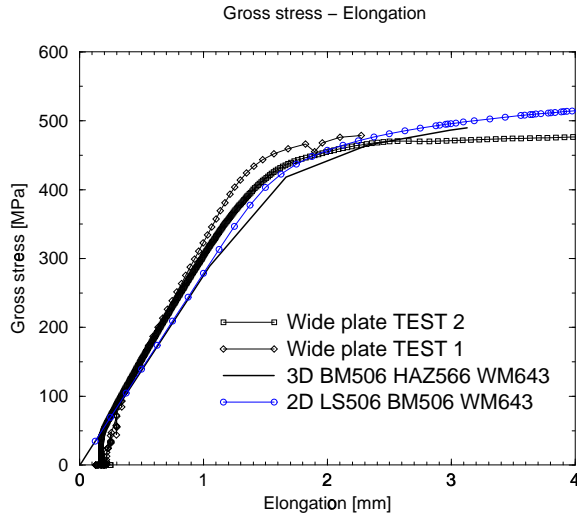

Figure 14: Gross Stress vs CMOD. Data from two tests are plotted and compared to data obtained from the 3D-model [see table 1 for the material calibration of the 3D model] and from the 2D-model [$\sigma_y^{WM} = 643 MPa$, $\sigma_y^{BM} = \sigma_y^{LS} = 506 MPa$]

accounting for the heat affected zone is $\frac{w_s+w_i}{2} + w_h(\frac{\sigma_Y^{HAZ}}{\sigma_Y^{WM}}) \approx 26mm$. Following the outline given in the previous section and since $h - a > \frac{w_s+w_i}{2} + w_h(\frac{\sigma_Y^{HAZ}}{\sigma_Y^{WM}})$, the line spring is calibrated with the same material parameter as the base metal $\sigma_Y^{BM} = \sigma_y^{LS} = 506 MPa$. Both global and local behavior of the plate is well described by the line spring model as seen in Figs. 13 and 14. The elastic stiffness of the structure is underestimated the same amount in both numerical analyses. This is due to the boundary conditions applied to the FE models. This inaccuracy at the elastic level is accepted since this study mainly focuses on the fully plastic behavior.

4 Conclusion

Regarding efficiency, the advantages in a line spring based approach compared to solid elements analysis of cracked shell structures are apparent. This paper shows the possibility of using the line springs in order to calculate fracture mechanical parameters in mis-matched situations such as welded plates with defects located in the weld metal. Calibration of the line springs with a proper yield strength, so that the plastic stiffness matrix can be properly calculated, is presented by means of averaging the weld metal/HAZ material area. If the width of this averaged area is less than the ligament, the base metal material properties are employed in the line spring finite element. Otherwise, the weld metal properties are employed. Comparison with large scale plate tests shows good agreement.

References

[1] Hibbit Karlson and Sorenson. ABAQUS Manual, version 5.2.

[2] Lee, H.; and Parks, D. M. Fully plastic analysis of plane strain single edged cracked specimen subjected to combined tension and bending. *Int.J. Frac.* 63, 329-349, 1993.

[3] Lee, H.; and Parks, D. M. Enhanced elastic-plastic line spring finite element. *Int.J. Solids Structures* 32, 2393-2418, 1995.

[4] O' Dowd, N.P., Shih, C.F. Family of crack-tip fields characterised by a triaxiality parameter: Part I-Structure of fields. *J. Mech. Phys. Solids* 40, 889-1015, 1991.

[5] O' Dowd, N.P., Shih, C.F. family of crack-tip fields characterised by a triaxiality parameter: Part II-Fravture Applications. *J. Mech. Phys. Solids* 40, 939-963, 1992.

[6] Parks, D. M. The inelastic line spring: estimates of elastic-plastic fracture mechanics parameter for surfaced cracked shells. *J. Press. Vessel Tech.* 103, 264-254, 1974.

[7] Parks, D. M. and White, C. S. Elastic-plastic line spring finite elements for surface cracked plates and shells . *J. Press. Vessel Tech.* 104, 287-292, 1974.

[8] Ranestad, Ø., Zhang, Z.L. and Thaulow, C. An Engineering Method for Constraint Based Assessment of Welded Construction Elements with Surface Cracks. *Int. J of Fracture.* 1999

[9] Ranestad, Ø., Zhang, Z.L. and Thaulow, C. Two-parameter (J-M) description of crcak-tip-stres-fields for an idealised weldment in small scale yielding. *Int. J of Fracture.* 1998

[10] Rice, J. R. A path independent integral and the appropriate analysis of strain concentration by notches and cracks. *J. Applied Mech.* 35, 379-386, 1968.

[11] Rice, J. R. and Levy, N. The part through surface crack in an elastic plate. *J. Applied Mech.* 185-194, 1968.

[12] Rice, J. R. The line spring model for surface flaws. *The Surface Crack Physical Problems and Computer Solutions.* (ed J. L. Sweldow), ASME 1972.

[13] Skallerud, B. Inelastic line springs in nonlinear analysis of cracked tubular joint. *Fatigue Fract. Engng Mat. Struct.* 18,463-477, 1996.

[14] Skallerud, B. A mixed mode I/II inelastic line spring. *Int. J. Solids Structures.* 33,4143-4166, 1996.

[15] Skallerud, B., Zhang Z. Finite element modelling of cracked inelastic shells with large deflections: 2D and 3D approaches. Accepted for publication *Int. J. Fatigue and Fract. Engng Mater. Struct..* 1999.

[16] Zhang, Z.L., Hauge, M., Thaulow, C. Two Parameter Characterization of the Near Tip Stress Fields for a Bi-Material Elastic-Plastic Interface Crack . *Int. Journal of Fracture*. 79,65-83, 1996.

[17] Zhang, Z.L., Hauge, M., Thaulow, C. Effects of Crack Size and Weld Metal Mismatch on the HAZ Cleavage Toughness of Wide Plates. *Engineering Fracture Mechanics*. 57,653-664, 1997.

[18] CSM, DNV, IWM, SINTEF, RWTH, NTNU ACCRIS REPORT (Acceptance criteria and level of safety for high strength steel weldments). *Summarizing reports*. 1997

Efficient fracture assessment of pipelines. A constraint-corrected SENT specimen approach.

Matteo Chiesa[1] ,Bjørn Skallerud and Christian Thaulow

Department of Mechanical Engineering
Norwegian University of Technology, Trondheim, Norway
e–mail: matteo.chiesa@matek.sintef.no
e–mail: bjorn.skallerud@maskin.ntnu.no
e–mail: christian.thaulow@maskin.ntnu.no

Bård Nyhus

SINTEF Materials Technology, Trondheim, Norway
Dept. of Fracture Mechanics and Materials Testing
e–mail: bard.nyhus@matek.sintef.no

Key words: shell finite elements, line springs, solid finite elements, plasticity, cracked shells, constraint, failure assessment.

Abstract. *Reeling has proven to be an efficient and cost effective method for offshore pipelaying. During the reeling process the pipe undergoes deformation that can strain the material by* $1 - 2\%$. *The existing failure assessment methods often turn out to be too conservative to allow such a strain level in the structure. The amount of conservatism can be significantly reduced by using a new failure assessment approach developed by SINTEF. This approach depends on finite element calculations for establishing the non-linear fracture mechanics parameters and the stress and strain distributions in the pipe. The present study addresses the performance of shell and line spring finite elements as a cost effective tool for performing such numerical calculations.*

---

[1]Author to whom all correspondence should be addressed.

1 Introduction

Reeling has proven to be an efficient and cost effective method for offshore pipelaying. This procedure strains the material close to the failure limit. A standard failure assessment analysis based on $[PD6493]$ and $[R6]$, see [3], [9], would hardly allow flaws in the pipe because of the high conservatism involved in the method. The Pipelaying process involves substantial resources, so any delays because of "unnecessary" repairs of flaws can be very expensive. Furthermore, repairing small flaws in the weld often leads to a further deterioration of the quality of the welds. The potential cost savings resulting from the relaxation of the conservatism of the failure assessments procedures are evident.

SINTEF has developed a new concept for failure assessment for low constraint applications which reduces the conservatism of the standard failure analysis, see [12], [11]. The method is based on the testing of constraint-corrected fracture mechanics specimens under tension. So far work has been concentrated on the SENT specimen. By varying the crack length and the distance between the clamps when the test is performed these specimens can be designed to give a constraint level comparable to that of a pipe with surface or through the thickness cracks. FE calculation of both the SENT and the pipe are necessary to design SENT specimens with a constraint level comparable to the pipe. In addition FE calculations have been used to derive analytical equations for the J-integral for the SENT specimen. The discretization of the cracked shell structure with solid finite elements in order to compute the fracture mechanics quantities makes such analysis time consuming. The present study addresses the performance of shell and line spring finite elements as an alternative tool for numerical calculations of the fracture mechanics parameters. This allows the number of degrees of freedom to be reduced by an order of magnitude compared to the 3D meshes utilized. The accuracy of this approximation seems to be satisfactory from an engineering point of view.

The new method based on constraint-corrected specimens has several advantages:

- It makes the failure assessment more efficient and precise by relaxing the high conservatism of the usual procedure.

- It makes the testing procedure for the SENT as easy as for the standard SENB.

- It provides a limit load obtained from the SENT that can be utilized to calculate the plastic collapse of the pipe.

The focus of this study is to find simple procedures for the computation of the fracture mechanics parameters necessary to perform failure assessment of pipes by using the new method. However, in our pursuit of engineering methodologies, a goal is to reduce the need for FE calculations. Current activities focus on mapping the constraint in pipes and SENT specimens for different crack geometries and loading conditions, in order to obtain a guideline for constraint-corrected SENT specimens. We also intend to find explicit equations for the fracture toughness of SENT specimens. With this, the method will not be more complicated than the current methods and the accuracy will be improved.

2 Outline of the new concept for failure assessment

2.1 Geometry-dependent fracture properties

The low constraint concept for failure assessment is based on the testing of a constraint-corrected fracture mechanics specimen under tension. So far work has focused on the SENT specimen. These specimens can be fitted to give the same constraint levels as for pipe with
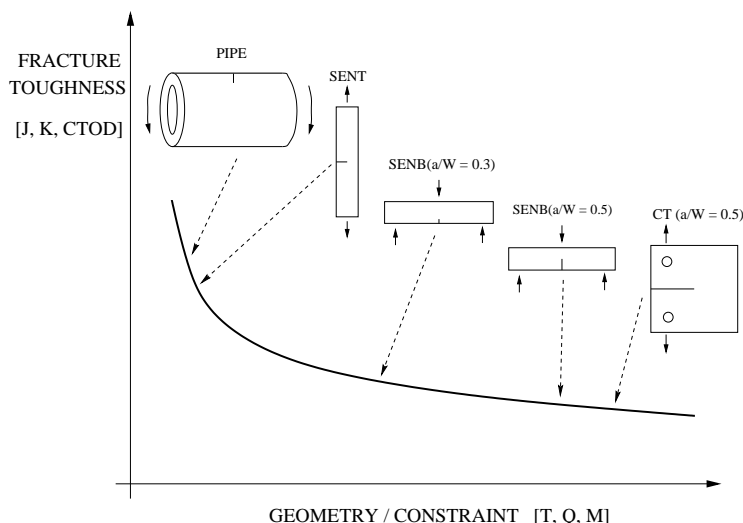
Figure 1: Schematic illustration of the influence of the constraint and specimen geometry on the fracture toughness.

cracks on the surface or through the entire thickness, see Fig. 1. The constraint level of the SENT specimen can be adjusted by varying the crack depth or the distance between the clamps. The stress fields in the low constraint geometries, such as SENT and pipes, and in the high constraint geometries, such as SENB, are different, see Fig. 2. Similar fracture mechanisms can be expected in geometries with a comparable constraint level. If the constraint-corrected SENT specimen undergoes brittle fracture, brittle fracture after ductile crack growth, plastic collapse, or plastic collapse after ductile crack growth, the pipe will most likely suffer from the same failure mechanism. It is important to keep in mind that the fracture toughness derived from constraint-corrected specimens is limited to a specific geometry, and should not be applied to other geometries without first verifying that the constraint in the geometry is similar or higher than that of the specimen. Traditional fracture mechanic specimens give lower bound solutions for the geometries. This is one reason for the high conservatism of the traditional approaches.

Full-scale testing shows that plastic collapse is usually the main failure mode that should be taken into account during pipeline design. The integrity of the pipe is determined by both the plastic deformation (tensile properties) in the rest ligament and the crack tip fields (fracture toughness). It is important to verify that the pipe is not susceptible to brittle failure. Failure assessments based on fracture toughness from traditional SENB and CT specimens often predicts
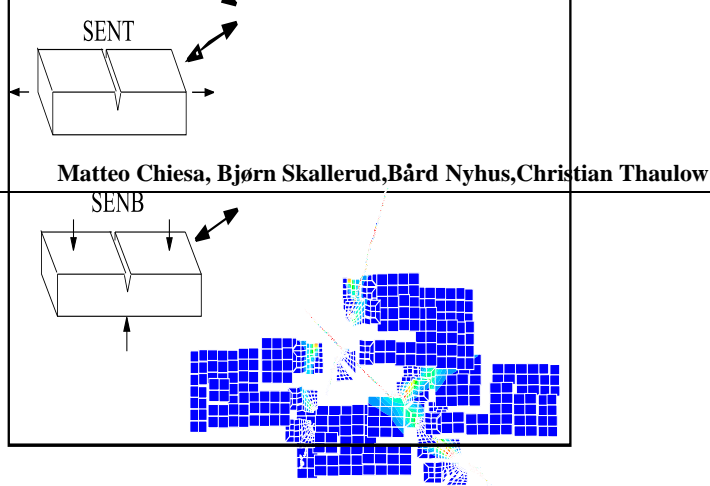
Figure 2: Ligament stress fields in high constraint SENB specimen and low constraint geometries like SENT specimens and pipes.

brittle fracture. However, full-scale testing shows that it is plastic collapse that is the limiting mechanism. Testing of constraint-corrected SENT specimens gives an improved estimate of fracture toughness and plastic collapse load. Further studies can therefore be concentrated on relaxing the high conservatism of the existing procedures for the prediction of plastic collapse.

2.2 Plastic collapse

Standards $[R6]$ and $[PD6493]$, see [9] and [3], for the plastic collapse failure mechanism are based on analytical solutions for the limit load and tensile properties. Plastic collapse is predicted when the stress in the ligament is equal to the flow stress (the average of yield strength and tensile strength). This analysis is conservative because the hardening is not entirely taken into account. The method developed herein accounts for both the hardening and inhomogeneous material zones in the failure assessment analysis. This is done by taking the limit loads from the constraint-corrected specimens, including this information in the calculation of the limit load for a pipe, and implementing this value into the failure assessment diagram, see [12], [10].

The ordinary failure assessment method becomes even more conservative for welds. The analytical equations for the limit load analysis are based on systems of homogenous materials. The properties of the material with the lowest strength are used in the assessments when the crack is located in a system with inhomogeneous material. This choice leads to an increased conservatism. It is also difficult to find the correct tensile properties in different parts of the weld zone. Such properties are necessary when analyzing the plastic collapse of a pipe with a

cracked weld. The loading direction under reeling is transverse to the girth welds, but since the welds are very narrow the tensile specimen has to be taken longitudinally to the weld. In addition the cross section of the specimen is very small compared to the cross section of the weld metal zone. For these reasons, it is difficult to find representative and reliable tensile properties for the weld metal transverse to the welding direction. For welds with soft zones in the HAZ the establishment of trustworthy tensile properties is even more difficult.

One can obtain a crack tip field which is comparable to that of circumferential cracks in pipes by testing SENT specimens taken from the pipe-wall, with a thickness close to the wall thickness, with realistic crack depths and loads similar to these in the pipe-wall. A representative plastic deformation of the rest ligament is also obtained with this. In the plastic collapse load obtained from these specimens, the effect of inhomogeneous material zones and the full hardening in these zones are taken in to account. This means that both the fracture and the plastic collapse properties can be determined by constraint-corrected SENT specimens. The need for the tensile properties of the different parts of the weld is therefore eliminated. The plastic collapse stress for the SENT specimens is transformed to an equivalent plastic collapse stress for the pipe by the analytical solutions for a homogenous material. Here is assumed that this transformation is independent of the inhomogeneity of the material strength. As long as the difference in geometry is minor the potential error in this assumption is also minor.

3 Numerical simulation

3.1 Shell and line spring finite element formulation

The FE analyses were carried out with the ABAQUS software. An eight-noded iso-parametric thick shell is used. In the analysis, deformation plasticity has been applied for the shell elements, with small strain theory and isotropic hardening. The part-through surface crack is originally a three dimensional problem as seen in Fig. 3a. The three dimensional problem is formulated within the context of two dimensional plate or shell theory with the part-cracked section represented as a line spring. The line springs take into account the additional flexibility due to the surface crack. The elastic stiffness is determined by the energy release rate combined with the
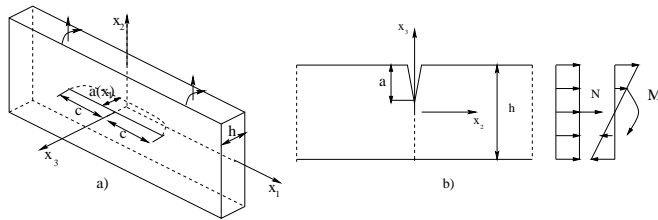

Figure 3: part trough surface crack and plane strain solution

known solutions for the stress intensity factor:

$$\mathbf{Q} = \mathbf{D_{el}} \cdot \mathbf{q} \tag{1}$$

$$\mathbf{Q} = [\mathbf{N}, \mathbf{M}]^{\mathbf{T}}, \quad \mathbf{q} = [\mathbf{u}, \theta]^{\mathbf{T}} \tag{2}$$

where $\mathbf{D_{el}}$ represents the elastic stiffness matrix and (u, θ) the extensional and rotational degrees of freedom of the line spring. For plastic condition, only the mode I case will be considered, [18], [20]. It has been solved for the line spring in terms of upper and lower bound solutions. The derivation of the mode I line spring follows classical plasticity theory:

$$\phi(\mathbf{Q}, \sigma_{\mathbf{Y}}^{\mathbf{LS}}; \mathbf{a}) = \mathbf{0} \tag{3}$$

$$d\mathbf{Q} = \left(\mathbf{D_{el}} - \frac{\left(\frac{\partial \phi^{\mathbf{T}}}{\partial \mathbf{Q}} \cdot \mathbf{D_{el}} \right)^{\mathbf{T}} \left(\frac{\partial \phi^{\mathbf{T}}}{\partial \mathbf{Q}} \cdot \mathbf{D_{el}} \right)}{\frac{\partial \phi^{\mathbf{T}}}{\partial \mathbf{Q}} \cdot \mathbf{D_{el}} \cdot \frac{\partial \phi}{\partial \mathbf{Q}} - \frac{\partial \phi^{\mathbf{T}}}{\partial \mathbf{Q}} \cdot \mathbf{Q} \cdot \frac{\partial \phi}{\partial \sigma_{\mathbf{Y}}^{\mathbf{LS}}} \frac{\mathbf{E_p}}{\sigma_{\mathbf{y}}^{\mathbf{LS}} \mathbf{kc^{n'}}}} \right) \cdot \mathbf{q} \tag{4}$$

where the current plastic modulus E_p, the length of the rest ligament c and the constants k and n' are quantities controlling the plasticity in the ligament region. The yield surface employed here is based on an upper bound slip line solution, see [18], as implemented in ABAQUS, see [1]. Note that σ_Y^{LS} denotes the yield stress in the line spring. This enables a possibility of using different materials in the plate and cracked region (e.g. a crack in a weld, see [4]). The yield surface describes the plastic behavior of the rest ligament. Having determined the plastic deformation increment, the crack tip opening displacement is obtained from slip line kinematics:

$$d\delta_p = du_p + \left(\frac{h}{2} - a \right) d\theta_p. \tag{5}$$

The validity of this relation has been investigated by Lee et al., [7]. Their results show that for shallow edge cracks $(a/h \leq 0.2)$ it becomes inaccurate, see [8].

Employing the connection between the J_p and the Dugdale crack tip solution corrected for plane stress/strain constraint, one has:

$$dJ_p = m\sigma_Y^{LS} d\delta_p \tag{6}$$

Here, m is a function of crack geometries and hardening characteristics. The total J integral may now be calculated:

$$J = J_e + J_p \tag{7}$$

As the edge crack is the basic case for the line spring, computed values of J for a surface crack will be more accurate in the center compared to positions approaching the surface at the crack ends.

The T-stress measures the constraint in the crack tip region and is used in combination with the $J - integral$ in order to quantify the dependence of the crack tip stress field on the geometry. The T-stress is the second term in the asymptotic expansion of the elastic solution by Williams, [22]. The T-stress has therefore been considered as an elastic parameter with a limited range of validity. Betegon and Hancock, [2], have shown that the T-stress provides a good estimate of the constraint even beyond the elastic and small scale yielding regime. Parks et al., see [21], have proposed a method for calculating the T-stress for the shell-line-spring-mesh based on Sham's analytical work. Parks argues that T can be seen as the summation of the contributions by the membrane force, $N(s)$, and the moment, $M(s)$. Thus the T-stress at any point along the crack front can be expressed as

$$T(s) = \frac{N(s)}{h} \cdot t_N(a(s)/h) + \frac{6M(s)}{h^2} \cdot t_M(a(s)/h) \tag{8}$$

where $N(s)$ and $M(s)$ have the same meaning as in Eq. 2. Functions t_N and t_M are calibration factors for T in a SEN specimen with a crack depth $a(s)$ and thickness h, under unit membrane stress $\sigma^\infty(\sigma^\infty = N(s)/h)$ and unit bending stress $\sigma_b(\sigma_b = 6M(s)/h^2)$. Sham, see Parks [21], has tabulated the t_N and t_M functions for the SEN specimen. In this study the same values are used to calculate the T-stress in the $SENT$ specimen and in the pipe. The results obtained from the shell-line-spring mesh are verified by carrying out both 2D and 3D solid finite element calculation of the same geometries.

4 Results and Observations

4.1 Plane strain 2D- and shell-line-spring- simulation of a SENT specimen

4.1.1 Discretizations
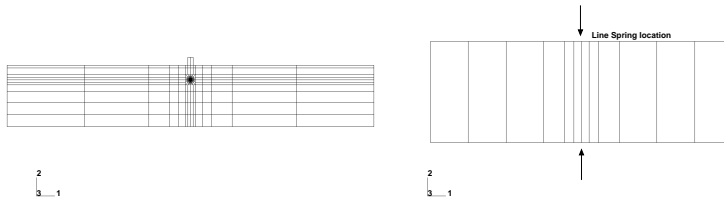
Figure 4: 2D and shell-line-spring FE mesh. The coordinate systems are local for each of the two mesh.

Fig. 4 illustrates the 2D-mesh for the SENT specimen with plane strain elements and with a combination of shell and line spring elements. Note that the coordinate systems for the two meshes in Fig. 4 are local for each mesh; direction 2 for the right-hand-side mesh corresponds to direction 3 for the left-hand-side mesh, see Fig. 5. The boundary conditions at the ends of the SENT specimen correspond to clamped (no rotation is allowed). In the shell-line-spring FE-model there are 66 nodes and 12 8-node shell elements of type $S8R$, see [1], and one line spring element. Displacement in the 2-direction and rotation about the 1-direction for the nodes
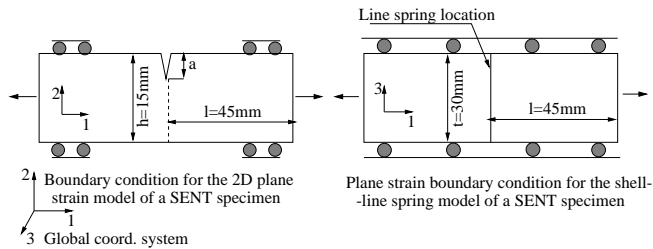
Figure 5: Clamped boundary condition utilized in the mesh in Fig. 4

at the top and at the bottom of the shell-line-spring model are constrained in order to obtain a plane strain situation in the middle of the model see Fig. 5. In the 2D-plane-strain-mesh for the SENT specimen there are 1619 nodes and 502 8-node plain elements of type $CPE8R$, see [1]. The cpu-time needed to complete the analysis is 10 times higher for the 2D-analysis than for the shell-line spring one. It should be noted that although the line spring feasibility is well established, the reason for the comparison between the 2D plane strain analysis and the line spring analysis carried out herein is due to the fact that a typical geometry of the SENT-specimen to be employed in the testing is rather stocky, and is not very similar to a shell structure. Hence if the constraint corrected SENT specimen is to be analyzed with line springs, the accuracy has to be verified.

4.1.2 Results

The 2D-plane-strain model, Fig. 4, is designed to comply with the 15mm thick SENT specimen. An idealized homogenous material is considered in this study along with small deformation theory. A parameter study is carried out for two different material yield strengths $[\sigma_y = 400MPa]$, $[\sigma_y = 600MPa]$ and for different crack depths: $a = 2.0mm$ $a = 3.5mm$ $a = 5.5mm$ $a = 7.5mm$ $a = 9.5mm$. Gross Stress vs Displacement curves for the five crack depths are plotted in figures 6 and 7. The global behavior of the SENT specimen is well described by the shell-line-spring mesh. The local stress field at the crack tip is described by either the $J - integral$ or the $CMOD$ (crack mouth opening displacement). There is a good agreement between the J values calculated from the two numerical discretization for J in the range $[500 - 1000N/mm]$ as seen in Figures 8 and 9, where the $J - integral$ is plotted against the Gross Stress. Experience from SENT testing has shown that the critical J-integral for most pipeline steel lies in the range $[500 - 1000N/mm]$. A better agreement in the transition zone can be obtained, see (Lee et al. I and II, 1993). The agreement of both the Gross Stress vs Displacement and the $J - integral$ vs Gross Stress curves is worse for the shallow crack $a = 2.0mm$. This is due to the yield function implemented in the ABAQUS software for the line-spring element, see [14]. This yield surface is meant for cracks sufficiently deep that the yielding is confined to the ligament. For the deepest crack it is also some disagreements, this is due to the stocky specimen combined with a load transfer that does not comply with shell modeling assumptions. Figures 10, 11, 12 and 13 represent the $J - CMOD$ curves for the different crack lengths for the two numerical meshes.

The shell-line-spring model describes the variation due to the different geometries in agreement with the results obtained by the 2D-plane-strain-model. This shows that the shell-line-spring-mesh can replace the more time consuming 2D-plane-strain-mesh analysis of the SENT specimen.

4.2 3D- and shell-line-spring- simulation of a SENT specimen

4.2.1 Discretization

In the shell-line-spring FE-model, Fig. 14, there are 190 nodes and 48 8-node shell elements of type $S8R$ and 3 line spring elements. Due to the symmetries of the SENT specimen only one half is modeled, with no allowance for transverse motion or rotation of the nodes along the
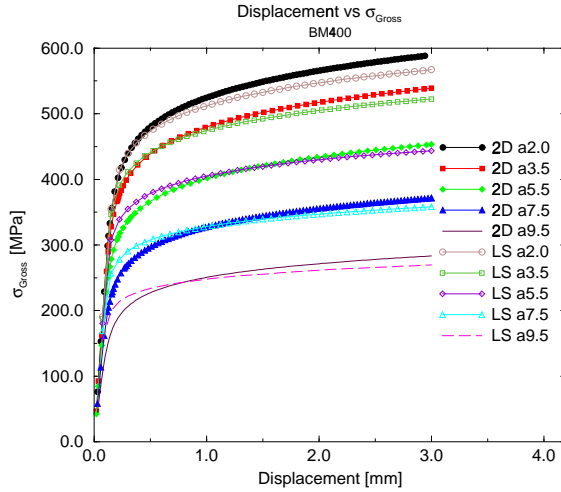
Figure 6: Gross stress vs displacement curves for different crack lengths [$a = 2.0mm$ $a = 3.5mm$ $a = 5.5mm$ $a = 7.5mm$ $a = 9.5mm$] and for yield strength [$\sigma_y = 400MPa$].$LS \longrightarrow$ shell-line-spring-mesh, $2D \longrightarrow$ 2D-plane-strain-mesh.
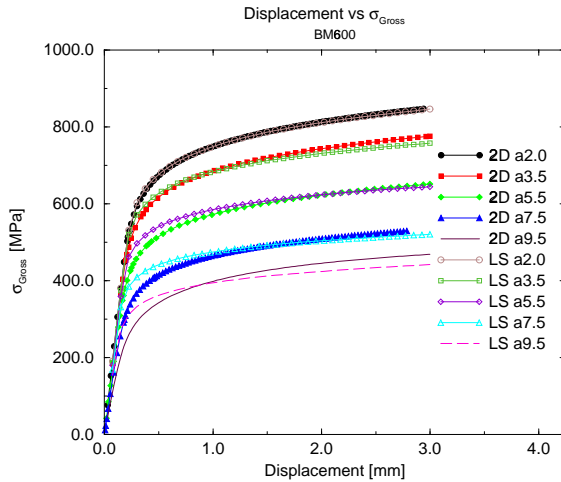
Figure 7: Gross stress vs displacement curves for different crack lengths see Fig. 6 and for yield strength [$\sigma_y = 600MPa$].

symmetry line. In the solid 3D-mesh for the SENT specimen, Fig. 14, there are 8711 nodes and 1340 3D elements of type $C3D20$. The cpu-time needed to complete the analysis is 12 times higher for the 3D-analysis than for the shell-line spring one. Note that small deformation theory was applied here also.
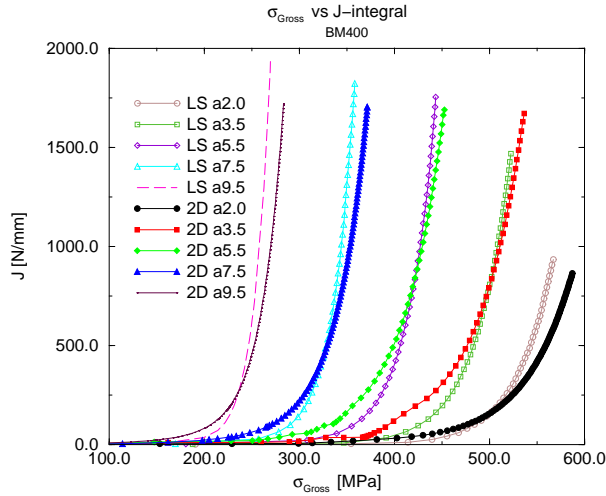
Figure 8: Gross stress vs J-integral curves for different crack lengths for $[\sigma_y = 400MPa]$.]
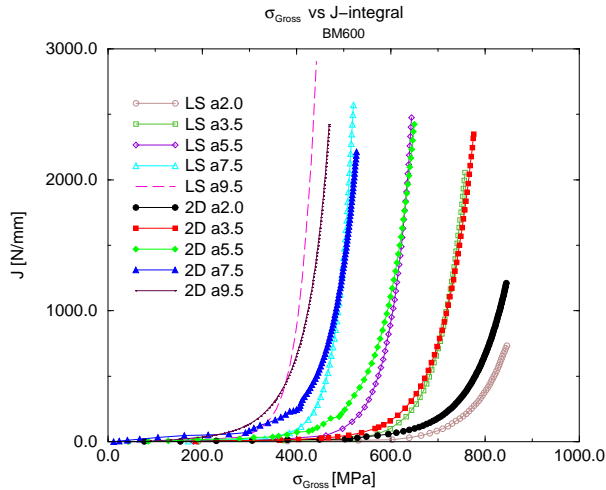
Figure 9: Gross stress vs J-integral curves for different crack lengths for $[\sigma_y = 600MPa]$.]

4.2.2 Results

The solid discretization of the $SENT$ specimen is the best way of representing the real situation. A plane strain model describes well the situation in the middle of the specimen where the stress triaxiality and the constraint are high. This is a conservative way of discretizing the $SENT$ specimen in order to reduce the CPU time needed for the numerical calculation. The line spring modeling is an alternative efficient way for performing such analysis without using too much computing time. The shell-line-spring-mesh describes the 3-dimensionality of the
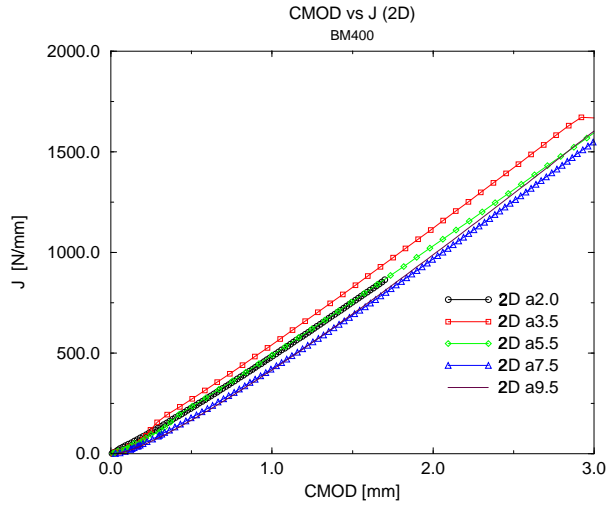
Figure 10: CMOD vs J-integral curves for different crack lengths and for a yield strength [$\sigma_y = 400 MPa$] . (Plane strain analysis)
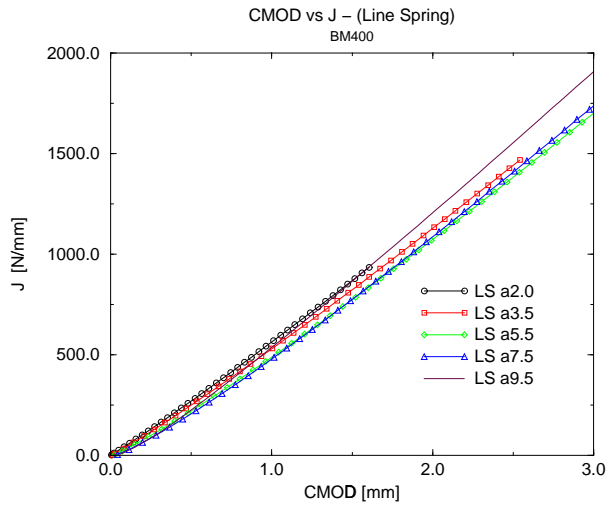
Figure 11: CMOD vs J-integral curves for different crack lengths and for a yield strength [$\sigma_y = 400 MPa$]. (shell-line-spring analysis)

$SENT$ specimen in a better way than the plain-strain-mesh, relaxing the conservatism involved with it. The difference from the previous mesh lies in the different boundary condition of the shell-line-spring-model. Displacement in the 2-direction and rotation about the 1-direction are allowed for the nodes along the line GF and are constrained at the symmetry line of the shell-
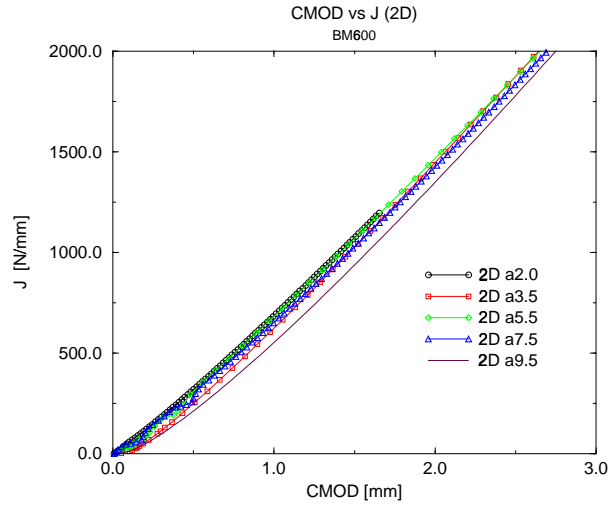
Figure 12: CMOD vs J-integral curves for different crack lengths and for a yield strength [$\sigma_y = 600MPa$] . (Plane strain analysis)
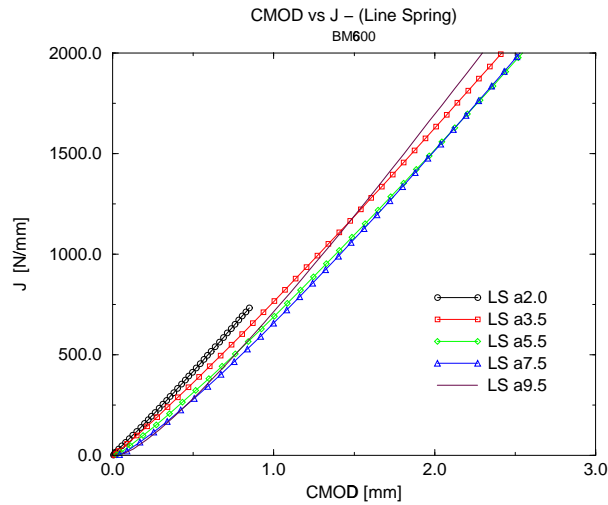
Figure 13: CMOD vs J-integral curves for different crack lengths and for a yield strength [$\sigma_y = 600MPa$]. (shell-line-spring analysis)

line-spring, see Fig. 17. The results from the "3D" discretization are plotted with those from the "2D" discretization for one single geometry ($a = 3.5mm$) as presented in Fig. 15 and 16. Fig. 15 shows the Displacement vs Gross stress curves for the "2D" and the "3D" discretization. The agreement between the "3D" meshes is better then for the "2D" ones. This is due to the fact that
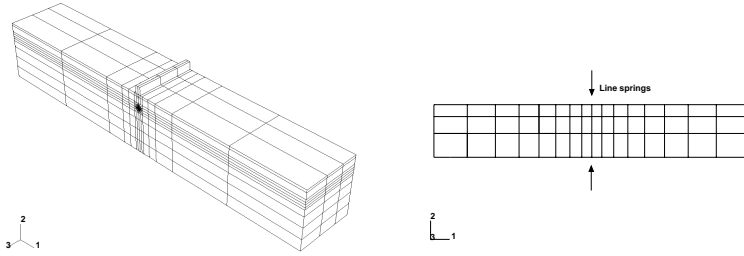
Figure 14: A 3D FE mesh [on the left hand side] is compared to a shell-line-spring FE mesh [on the right hand side] for half of the SENT specimen.The coordinates systems are local for each of the two mesh.
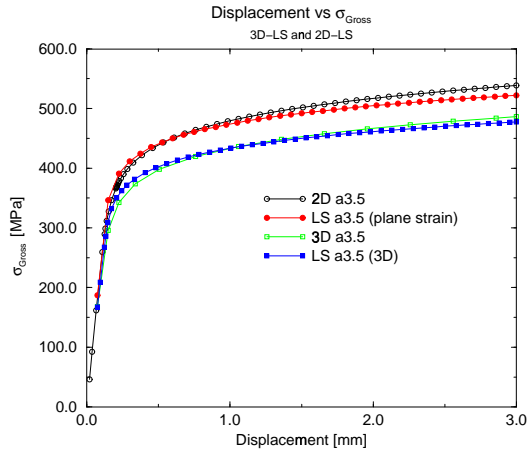
Figure 15: Displacement vs Gross stress curves for different meshes: $2D \implies$ plane-strain-2D-mesh (Fig. 4), $3D \implies$ 3D-solid-mesh (Fig. 14), $LS - plane - strain \implies$ plane-strain-shell-line-spring-mesh (Fig. 4), $LS\ 3D$ "3D"-shell-line-spring-mesh (Fig. 14).

the shell-line-spring mesh utilized in the "3D" discretization is much finer then the one used in the "2D" discretization. The same trend can be also observed in Fig. 16 where the Gross stress vs $J - integral$ for the different meshes is plotted. The shell-line-spring meshes seem to be well suited to describe the SENT specimen.

4.3   Constraint calculation in plane strain

The T-stress measures the constraint in the crack tip region and quantifies the dependence of the crack tip stress field on the geometry. The calculation of the T-stress in the shell-line-spring mesh is carried out by following the outlines of Parks, Eq. 8. The calculation is also carried out in a 2D plain-strain model. The nominal stress of the elements along the crack flank S_{11} in Fig. 18 is read at different distances D from the crack tip , see Fig. 18. The converged value is read
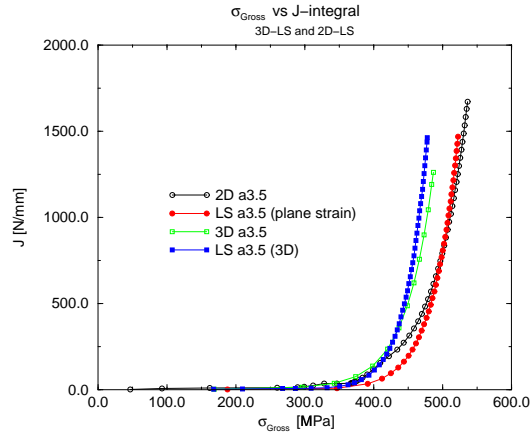
Figure 16: Gross stress vs $J - integral$ curves for different meshes, see Fig. 15
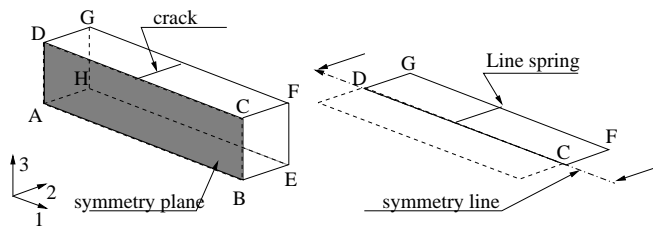
Figure 17: Symmetries of the SENT specimen utilized in the numerical discretization.

as the T-stress.
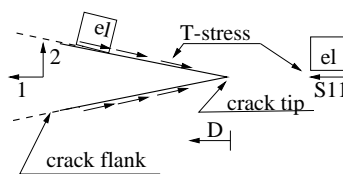
Figure 18: Representation of the way of calculating T-stress

An elastic calculation of the T-stress has been carried out and the values obtained by such a calculation are plotted in Fig. 19. The T-stress is taken at a similar local stress level [similar $J - integral$]. The T-stress from the line spring model is of course independent of the distance from the crack tip. Kirk et al. employed elements located at a distance $2\frac{J_0}{\sigma_0}$ in front of the crack tip in order to determine T , see Fig. 18. This approach requires more post-processing of the results than in the present approach. Fig.20 presents the biaxiality factor β for the different a/W relations. β is a dimensionless parameter which relates T to the stress intensity factor K_I

14
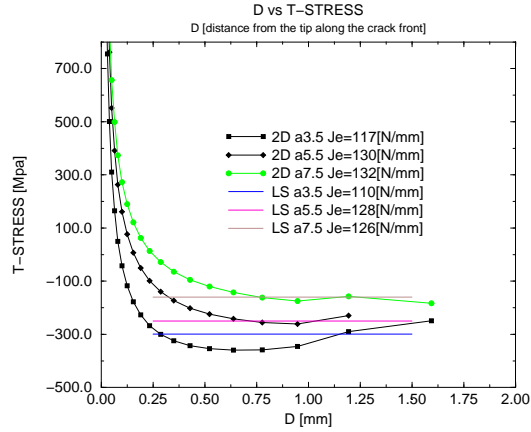
Figure 19: $T - stress$ vs D for the line spring mesh and from the 2D-plane-strain-mesh. D [distance from the tip along the crack flank]
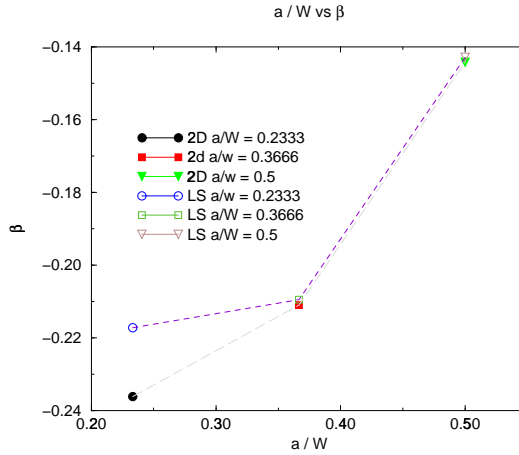
Figure 20: β vs a/W for the line spring mesh and from the 2D-plane-strain-mesh

through Eq. 9.

$$\beta = \frac{T\sqrt{\pi a}}{K_I}. \tag{9}$$

It is noted that the results from the 2D plane-strain analysis and those from the shell-line-spring simulation departs for cracks of depth less than $0.35W$. One reason for this is the assumption inherent in Eq. 8. The $2D$ simulation senses the proximity of the free surface when the crack get shorter. However, for cracks deeper than $0.35W$ the agreement between the shell-line-spring mesh and the plane-strain mesh is good.

15

4.4   3D- and shell-line-spring- simulation of a pipe

4.4.1   Discretization
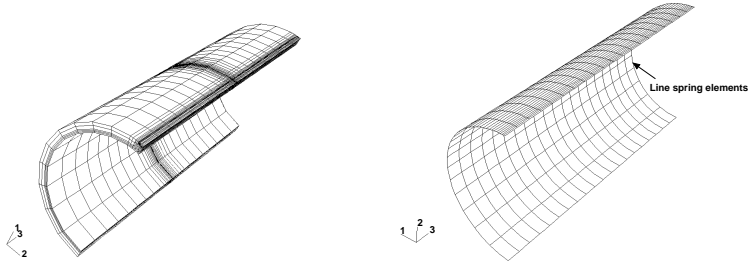
Figure 21: A 3D FE mesh and a shell-line-spring FE mesh for half of the pipe.

Non-linear small deformation FE analysis of a four meter long pipe with a $450mm$ long surface notch with crack depth $a/W = 0.75$ under pure tension has been carried out. The pipe wall is $25.7mm$ and the outer diameter is $921mm$. Fig. 21 illustrates the 3D mesh for the pipe by means of solid elements and by means of a combination of shell and line spring elements. Due to the symmetries of the considered geometry only one half is modeled, with no allowance for transversal motion or rotation of the nodes along the symmetry plane. In the shell-line-spring FE-model, Fig. 21, there are 1784 nodes and 560 8-node shell elements of type $S8R$ and 9 line spring elements. In the solid 3D mesh for the pipe, on the left hand side of Fig. 21, there are 10200 nodes and 8370 8-node elements of type $C3D8$. The cpu-time needed to complete the analysis is ≈ 10 times higher for the 3D analysis than for the shell-line spring one. This difference in calculation time could be even bigger if a longer crack is considered due to the fact that the number of degrees of freedom for the 3D mesh would grow almost proportionally to the crack length. The CPU-time for shell-line-spring analysis is not effected by changing crack size.

4.4.2   Results

Fig. 22 and Fig. 23 show the Displacement vs Stress curve and CMOD vs Stress curves respectively for the two discretization considered. The agreement of the results obtained from the two meshes is excellent. This is partly due to the fact that the shell-line-spring mesh is very fine. Fig. 24 represents the stress vs $J - integral$ at crack center, the agreement is again good. In Fig. 25 the T-stress is plotted from the tip along the crack flank for the deepest point of the crack. The T-stress value from the shell-line-spring analysis is higher then the value obtained from the 3D analysis of the pipe as seen in Fig. 25. The numerical analysis from which we read the T-stress is carried out in the elastic regime. The calculation of the T-stress for the pipe geometry by means of the shell-line-spring mesh follows the outlines of Parks et al., see [21], as discussed earlier. From our results it seems that Eq. 8 can be utilized also for the calculation of the T-stress of the pipe even if further investigations need to be carried out to validate the method for different crack geometries.
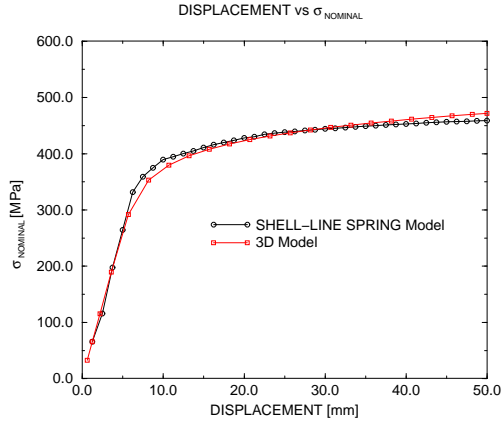
Figure 22: Displacement vs Stress for the two different discretizations of the pipe see Fig. 21.
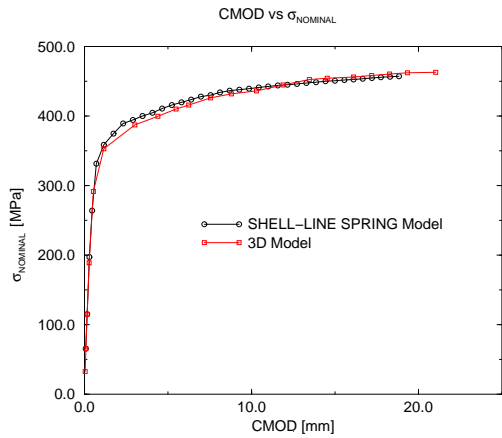
Figure 23: CMOD vs Stress for the two different discretizations of the pipe see Fig. 21.

5   Comparison of β with results from other studies

Fig. 26 compares our calculations of the biaxiality ratio β with the calculations performed in other studies, see [5]. A deviation between the two methods is apparent for short crack depths. In the 2D case this is due to the different methodology used for the calculation of the T-stress. In our study the T-stress calculations are performed at the crack flank for finite dimiension geometries, while Kirk et al., see [5], calculates the T-stress at a normalized distance in front of the crack tip using MBL finite element models. See also Fig.20 . The deviation is less for deeper cracks for which the surface effect on the stress values along the crack flank is negligible.

A deviation is also apparent for the biaxiality ratio as calculated from the shell-line-spring and from the 3D mesh, $\beta_{LS\_PIPE} \neq \beta_{3D\_PIPE}$, as shown on Fig. 26. This is due to the fact that Eq
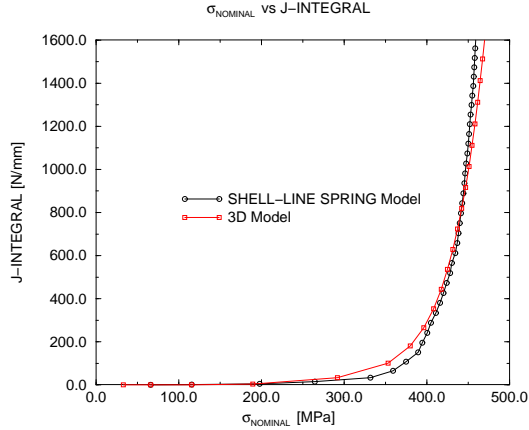
Figure 24: Stress vs $J - integral$ for the two different discretizations of the pipe see Fig. 21.
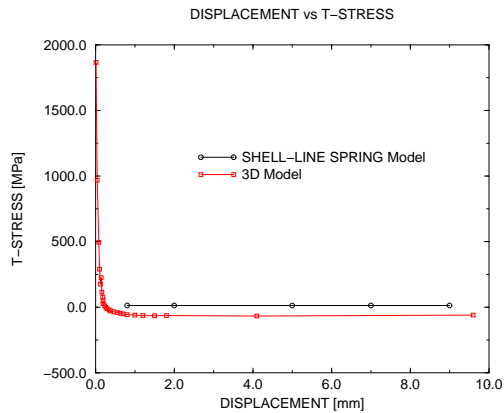
Figure 25: Displacement vs T-stress for the two different discretizations see Fig. 21. D [distance from the tip along the crack front.]

.8, by which we calculated the T-stress, is valid for a wide plate with a long, deep crack and not directly for the pipe. The constraint calculated from the shell-line-spring analysis by using Eq .8 gives conservative results, $\beta_{LS\_PIPE} > \beta_{3D\_PIPE}$ as shown on Fig. 26. However, the ranking of the geometry effect using the β parameter from the shell-line-spring model and the 3D model is similar, i.e. a reduced constraint when compared to the SENB specimen. It is concluded that the FE analysis for the SENT specimen can be properly carried out by using the line springs. Further studies are, however, needed in order to find an analytical equation which better relates the membrane force and the moment of the pipe to the T-stress.

Fig. 26 confirms what has been presented in section 2, Fig. 1: the traditional bending specimen SENB with a deep notch is far too conservative when a tubular geometry under tension or gobal
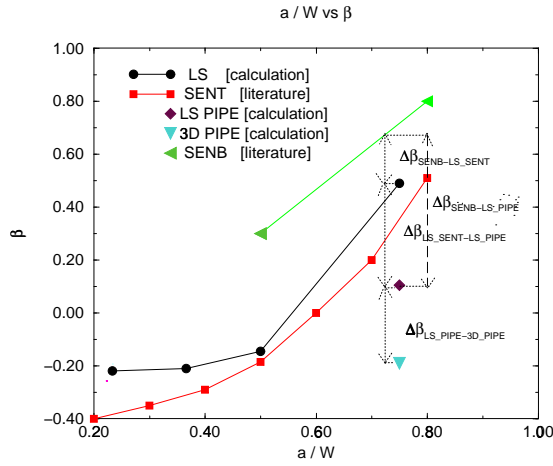
Figure 26: β vs a/W from the literature and from our results.
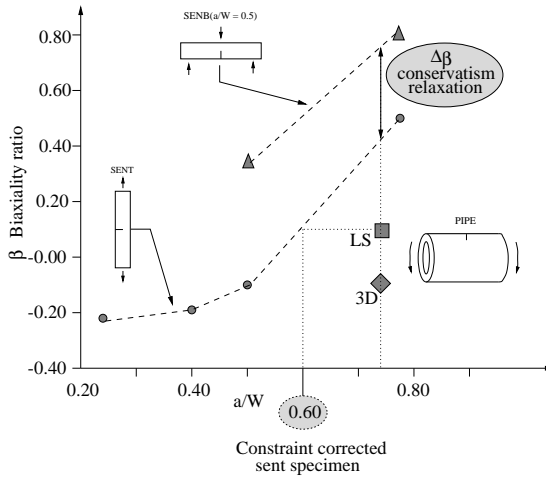
Figure 27: Constraint correction

bending is considered. The use of a SENT specimen with the same crack length as for the pipe relaxes the conservatism of the failure assessment, see Fig. 27. This can be seen in Fig 26 where $\Delta\beta_{LS\_SENT-LS\_PIPE} < \Delta\beta_{SENB-LS\_PIPE}$.

The SENT specimen can be constraint corrected with the value obtained from the shell-line-spring analysis of the pipe, see Fig 27. The constraint correction consists in finding a SENT specimen with a proper crack depth and geometry size so that its constraint is similar to that of the pipe. With the given SENT geometry employed here, see Fig. 5, the constraint-corrected SENT specimen which corresponds to the pipe with $a/W = 0.75$ is the specimen with $a/W =$

0.60, see Fig. 27. A representative $CTOD$ for the pipe is obtained by testing this constraint-corrected SENT specimen. In order to use the same SENT specimen for fracture mechanics and limit load analysis the same a/W-ratio as for the pipe has to be used for the SENT specimen and the correction is carried out by varying the geometry of the SENT specimen.

One should note that for a slender SENT specimen loaded in tension, a nonlinear geometry effect may evolve as the specimen will try to carry the load by pure membrane forces. This is manifested by finite out-of-plane deflections of the specimen during testing. As the ratio of tension and bending in the ligament controls constraint, the fracture initiation may be affected. In such cases all finite element simulations performed in the approach should account for large deformations. For stocky specimens this effect is small.

6   Summary

This study shows the performance of shell-line-spring models in calculating the response and fracture mechanics parameters for SENT specimens and cracked pipes. With this, the time consumed for FE calculation in the low constraint concept for failure assessment is greatly reduced. The proposed procedure for establishing the dimensions of the SENT specimen to be tested is as follows:

- FE model of a cracked pipe (shell-line-spring).

- Calculation of the T-stress from an elastic analysis, by means of Parks-Sham equations.

- FE model of a SENT specimen (shell-line-springs).

- Iteration of the design parameters for the SENT specimen up to the level where the T-stress is comparable to that of the pipe, see Fig. 27.

- Construction of the test specimen following from the previous point. The specimen may contain welds

- Perform the test.

The potential of the methodology will be investigated in a forthcoming publication, where significant test data will provide a verification basis.

References

[1] Hibbit Karlson and Sorenson., ABAQUS Manual, version 5.2.

[2] Betegon C. and Hancock J.W., Two Parameters Characterization of the Elastic-Plastic Crack Tip Field. *Journal of Applied Mechanics.* 58, 104-110, 1991.

[3] British Standard 7910 Guide on methods for assessing of flaw in fusion welded structures. 7910:1999.

[4] **Paper I:** Chiesa M., Skallerud B. and Thaulow C., Line spring elements in a yield strength mismatch condition. To appear in *Engineering Fracture Mechanics*.

[5] Kirks M.T., Dodds R. H. Jr. and Anderson T.L., Approximate Techniques for predicting Size Effects on Clevage Fracture Toughness. *Fracture Mechanics: 24th Volume.* ASTM STP 1207.

[6] Hancock J.W., Reuter W.G. and Parks D. M., Constraint and Toughness Parameterized by T. *Int.J. Solids Structures* 32, 2393-2418, 1995.

[7] Lee H. and Parks D. M., Fully plastic analysis of plane strain single edged cracked specimen subjected to combined tension and bending. *Int.J. Frac.* 63, 329-349, 1993.

[8] Lee H. and Parks, D. M., Enhanced elastic-plastic line spring finite element. *Constraint Effect in Fracture* ASTM STP 1171, 1993.

[9] Milne, I., Ainsworth R. A., Dowling A. R. Stewart A. T. Assessment of the Integrity of Structures Containing Defects. *Central Electricity generating board report* R/HR6-rev 3, 1986.

[10] Nyhus B., OGT Repair Welding. *SINTEF REPORT.* open report, 1999.

[11] Ørjasæter O. and Nyhus B. AiS: Fatigue and fracture mechanics testing of MIG and FS welded panels. *SINTEF report.* Open report, 1999.

[12] Nyhus B., Oseberg Hyperbaric welding procedure development. Fracture mechanics testing and ECA analysis. *SINTEF report.* Unrestricted, 1998.

[13] Parks D. M., A stiffness derivate finite element technique for the determination of crack tip stress intensity factors. *Int.J. Frac.* 487-502, 1974.

[14] Parks D. M., The inelastic line spring: estimates of elastic-plastic fracture mechanics parameter for surfaced cracked shells. *J. Press. Vessel Tech.* 103, 264-254, 1981.

[15] Parks D. M. and White, C. S., Elastic-plastic line spring finite elements for surface cracked plates and shells . *J. Press. Vessel Tech.* 104, 287-292, 1982.

[16] Rice J. R., A path independent integral and the appropriate analysis of strain concentration by notches and cracks. *J. Applied Mech.* 35, 379-386, 1968.

[17] Rice J. R. and Levy, N., The part through surface crack in an elastic plate. *J. Applied Mech*. 185-194, 1968.

[18] Rice J. R., The line spring model for surface flaws. *The Surface Crack Physical Problems and Computer Solutions*. (ed J. L. Sweldow), ASME 1972.

[19] Skallerud B., Inelastic line springs in nonlinear analysis of cracked tubular joint. *Fatigue Fract. Engng Mat. Struct*. 18,463-477, 1996.

[20] Skallerud B., A mixed mode I/II inelastic line spring. *Int. J. Solids Structures*. 33,4143-4166, 1996.

[21] Wang Y. Y., Parks, D. M., Evaluation of the elastic T-stress in surface crcaked plates using the line-spring method. *Int.J. Frac.*. 56, 25-40, 1992.

[22] Williams M.L., On the Stress Distribution at the Base of a Stationary Crack. *J. Applied Mech*. Vol 24, 109-114, 1957.

[23] Zhang Z.L., Hauge M. and Thaulow, C., Two Parameter Characterization of the Near Tip Stress Fields for a Bi-Material Elastic-Plastic Interface Crack . *Int. Journal of Fracture*. 79,65-83, 1996.

Closed form line spring yield surfaces for deep and shallow cracks: formulation and numerical performance.

Matteo Chiesa[1]**, Bjørn Skallerud**

Institute of Applied Mechanics
Norwegian University of Technology, Trondheim, Norway
e–mail: matteo.chiesa@matek.sintef.no
e–mail: bjorn.skallerud@maskin.ntnu.no

Dietmar Gross

Institute of Mechanics,
Darmstadt University of Technology, Darmstadt, Germany
e–mail: gross@mechanik.tu-darmstadt.de

Key words: plasticity, yield surface, convexity requirement, shallow crack, line spring, cracked shells, failure assessment, elastic predictor, plastic corrector, iso-error maps.

Abstract. *The line spring finite element is a versatile numerical tool for performing approximate fracture mechanics analysis of surface cracked shells. The accuracy of the shells line spring finite element solution for medium-sized cracks is higher than the accuracy for the shallow-sized ones. Proper treatment of shallow cracks is important because they are the ones most frequently encountered in engineering practice. Accurate yield surfaces of plane strain single-cracked (SEC) specimens having shallow, as well as deep, cracks are developed here in order to improve the overall performance of the line spring element. The yield surface is represented by equations that automatically satisfy the convexity requirement and that fit the result of the finite limit analysis. The present study addresses, furthermore, the performance of the backward-Euler return algorithm for one of the accurate yield surface formulated here, by means of iso-error maps.*

---

[1]Author to whom all correspondence should be addressed.

1   Introduction

Pipelines are a common example of a shell structure containing defects. The defects are usually introduced during the welding process necessary for joining different parts of the pipeline. The direct discretization of the cracked pipe structure with solid finite elements, in order to compute the fracture mechanics quantities, leads to large problems, and makes such analysis infeasible for this application. In order to calculate directly the fracture mechanics parameters in structural analysis, it is possible to use a combination of shell and line spring finite elements instead of solid finite elements.

The part-through surface crack is originally a three dimensional problem as seen in Fig. 1a. The three dimensional problem is formulated within the context of two-dimensional plate or shell theory with the part-cracked section represented as a line spring. The stiffness of the line spring is derived from a plane strain SEC specimen under tension and bending. General yielding loci for the SEC specimen were obtained from the known slip-line fields under bending. For the opening bending with high tension, an upper bound yield surface can be obtained from a kinematically admissible flow field consisting of a slip along a circular arc , see [20]. The validity of these yield surfaces is limited to deep cracks. It has been observed that the slip line field of shallow cracks in predominant bending is quite different from that of deep cracks, see (Green and Ewing). For a shallow crack, there exists an interaction between the crack-tip field and the front surface, and the slip-lines are observed to extend to the front surface. In the continuum finite element analysis using non-hardening plasticity, total equivalent plastic strain contours, which can be regarded as quasi-slip-lines, also have the same feature.

Proper treatment of shallow cracks is important because these cracks are the cracks most frequently encountered in engineering practice. During pipe-laying by reeling, for example, the material is strained close to its failure limit and a standard failure assessment analysis would just allow short flaws in the pipe because of high conservatism involved in the method. The focus of this study is to develop yield surfaces that univocally contain more accurate information about the general yielding behavior of shallow, as well as deep, SEC specimens. These yield surfaces are compared with Rice's approximate quadratic form and with yield surfaces derived from the slip-line field. One of the proposed yield functions is furthermore implemented in the inelastic line spring framework in order to improve the accuracy of the line-spring finite element solution for shallow cracks. The details of the implementation of the backward Euler integration scheme at the integration point of the line spring element in order to account for plasticity are here presented and the performance of the algorithm is assessed by means of iso-error maps. Work is in progress to implement the proposed elastic-plastic line-spring finite element in the framework of a commercial FEM program.

2   Elastic-Plastic Line-Spring finite element formulation

The part-through surface crack is originally a three dimensional problem as seen in Fig. 1a. The three dimensional problem is formulated within the context of two-dimensional plate or shell theory with the part-cracked section represented as a line-spring. The line-springs take into

account the additional flexibility due to the surface crack. The stiffness of the line-spring, with extensional and rotational degrees of freedom (δ, θ), is derived from a plane strain edge-cracked strip loaded in tension and in bending (N, M), see Fig. 1b, i.e. mode I [20]. The formulation of the Line-Spring element is presented in Appendix A. It is compatible with a two-dimensional plate or shell element with four nodes. A combination of shell and line spring elements enables
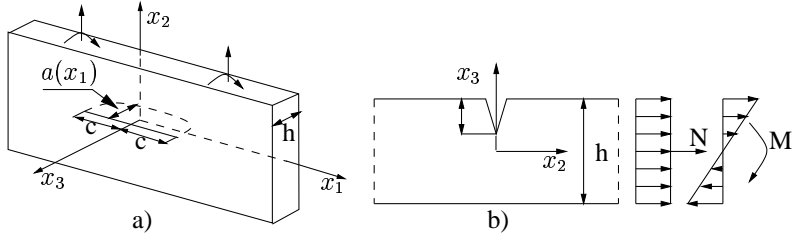
Figure 1: Part-trough-surface-crack and plane strain solution.

us to describe the three dimensional part-through surface crack problem within the context of two-dimensional plate or shell theory.

The derivation of the elasto-plastic line-spring for the mode I case follows the classical plasticity theory, details are presented in Appendix B. Fig. 2 shows a simplified picture of the flow field in the $kc - zone$ under a flow condition resulting from the slip-line analysis. The yield surface implemented in ABAQUS is based on the upper-bound slip-line solution [20], see [1]. The
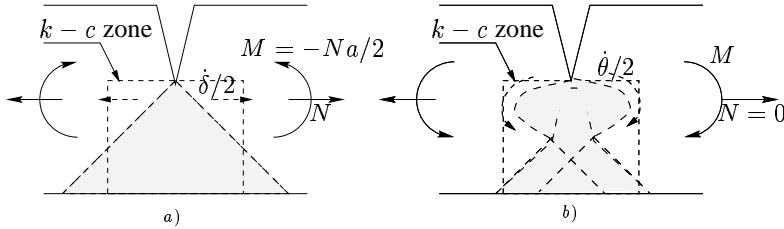
Figure 2: Slip line field approximation in the $kc - zone$. a) slip line solution for pure extension. b) Green Hundy solution for pure bending

yield surfaces implemented in ABAQUS describe the plastic behavior of the $kc - zone$. These representations of the yield surface provide satisfactory results for a crack-depth-to-thickness ratio $\frac{a}{h} > 0.3$. The main goal of this study is to propose an alternative yield surface which is able to univocally characterize the fully plastic yielding of both shallow and deep crack depths.

3 Yield Surfaces

The construction materials utilized for pipelines are often so ductile that a part of or the whole ligament between the surface crack front and the far shell wall undergoes yielding before frac-

ture criteria are met. Cracked pipelines can be analyzed effectively with an elastic-plastic line-spring model as presented in section 2. A convex yield surface, Eq. 38, is required for the plastic line-spring model. The yield surface for the plane-strain SEC specimen, subjected to combined tensile force and bending, is utilized for this purpose.

3.1 Explicit yield surfaces

3.1.1 Upper-bound approach

Fig. 3a shows a kinematically admissible flow field for the plane-strain SEC specimen for a rigid-plastic non-hardening material. The plane-strain single-edge specimen is subjected to combined tension and bending. In Fig. 3, δ is the work-conjugate displacement due to the axial force per unit length, N, and θ is the work conjugate rotation due to the bending moment per unit length, M. Rice, [20], has derived a yield surface for the ligament in mode I loading
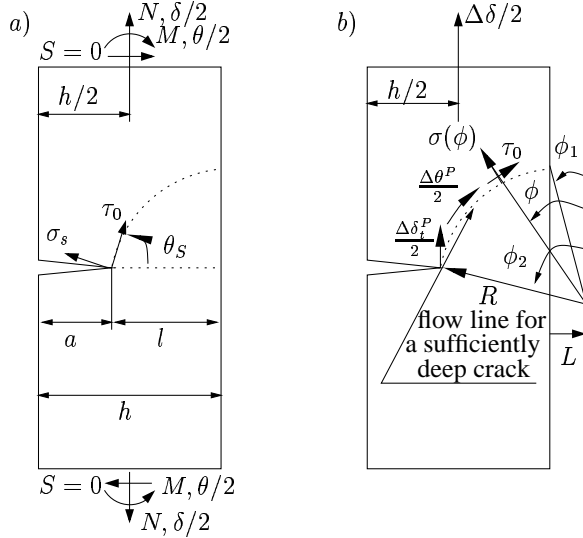
Figure 3: a) Plane strain single-edge cracked specimen subjected to combined tension and bending, b) Kinematically admissible flow field used by Rice to generate an upper bound yield surface, where $\Delta \delta_t^p = \Delta \delta^p + (h/2 - a)\Delta \theta^p$

(N,M), based on the slip-line field theory. The yield surface proposed by Rice is valid for deep cracks and for a ligament loaded predominantly in tension. Fig. 3b shows the kinematically admissible flow field used by Rice to generate an upper-bound yield surface. Yielding occurs by discontinuous slip along a circular arc of radius R with the center O at a distance L measured positive to the right of the specimen surface. There are four kinematic variables (ϕ_1, ϕ_2, L, R) of which only one, after imposing two geometrical constraints and minimizing the upper bound inequality, is an independent variable. Rice chose this to be ϕ_1, in this way an upper bound yield

4

surface was graphically constructed. The result reads:

$$\phi_R = \left[\frac{N/2\tau_0 l - 0.3}{0.7}\right]^2 + 9\left[\frac{M + Na/2}{2\tau_0 l^2}\right]^2 - 1 = 0 \tag{1}$$

where τ_0 is the yield strength in shear, a is the crack length and l is the remaining ligament $h = a + l$. This explicit equation (representing the yield surface) covers load states of predominant tension ($N > 0, \theta \geq 0$).

Flow is also reached in the plane-strain single-edge specimen when a bending moment is superposed to an axial force. The GH-field (see Fig. 2, Green Hundy) for pure bending can be modified to produce a slip-line field for the combined loading state. White et al. obtained the following yield surface:

$$\phi_{MGH} = \frac{M}{\tau_0 l^2} - \frac{N}{2\tau_0 l}(0.26 - a/l) + 0.37\left(\frac{N}{2\tau_0 l}\right)^2 - 0.63 = 0 \tag{2}$$

The addition of a tensile force has the effect of "cutting off" a portion of the back-face compressive region, while the addition of a compressive force produces the opposite effect. It was previously observed by White et al. that the maximum allowable axial force is $N_{max} = 0.55(2\tau_0 l)$ and the minimum is $N_{min} = -2\tau_0 l$. In conclusion, Eq. 2 represents a good description of plasticity of the SEC specimen at the crack tip when sufficiently deep cracks are considered. Furthermore, Eq. 2 is to be considered as an upper-bound representation of the yield surface.

3.1.2 Lower-bound approach

The yield surface of an uncracked strip subjected to combined tension and bending was proposed by Green and Ewing:

$$\phi_U = \frac{2|\tilde{M}|}{\tau_0 h^2} + \left(\frac{N}{2\tau_0 h}\right)^2 - 1 = 0 \tag{3}$$

where h is the thickness of the uncracked strip and $\tilde{M} = M$ is the moment about mid-specimen. Eq. 3 is to be considered exact since both the upper-bound and the lower-bound approaches lead to the same expression. Replacing the thickness h with the rest-ligament size l and interpreting $\tilde{M} = M + Nl/2$ as the moment about mid-ligament, Eq. 3 provides a lower bound yield surface for the SEC specimen.

3.2 Tabulated yield surfaces

The validity of the yield surfaces defined by Eq. 1 and Eq. 2 is limited to cracks where $\frac{a}{h} > 0.3$. For such cracks, it is possible to consider the yield as confined to the rest ligament $kc - zone$. Lee and Parks tabulated a yield surface by loading a SEC finite-element model of an isotropic elastic-perfectly plastic material with a combined displacement δ and rotation θ so that the yielding point[2] of the specimen is reached, see [9]. Fig. 4 schematically illustrates the way Lee

---

[2]The yielding point is taken as the limit load state of the SEC specimen under combined displacement and rotation
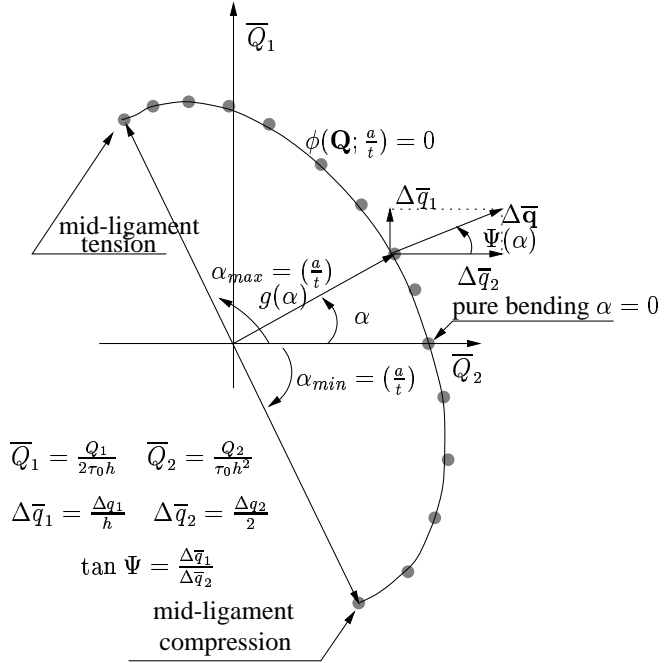
Figure 4: Schematic illustration of a yield surface in the generalized force space for a given relative crack depth. The circled point represent data points obtained from the continuum finite element analysis.

and Parks tabulated their yield surfaces, the coordinates $\bar{Q}_2 = \frac{M}{\tau_0 h^2}$ and $\bar{Q}_2 = \frac{N}{2\tau_0 h}$ are the generalized forces normalized by means of the shear yield stress τ_0. A set of data obtained from the continuum finite-limit analysis is represented by circular points in the generalized-normalized $\bar{Q}_1$-$\bar{Q}_2$ space. These points represent a yielding state for the SEC finite-element model. The yield locus represented by the solid line in Fig. 4 interpolates the points of the discrete set of data with the piecewise rational quadratic function and the Hermite cubic function, see [9]. Lee and Parks observed a discrepancy between their computed yield function and both Rice's quadratic, Eq. 1, and the modified GH yield surface, Eq. 2, for shallow cracks of relative crack depths $\frac{a}{h} = 0.1$ and 0.2. The agreement of the analytical yield surfaces, Eq. 1 and 2, and the constructed yield surfaces proposed by Lee and Parks is good for cracks where $\frac{a}{h} > 0.3$ see Fig. 5 and 6. For deep cracks, the yield surfaces are observed to fall on one master curve. In Fig. 5 and 6 the data points sets obtained from the continuum analysis are represented by filled symbols, the dashed lines represent ϕ_R and ϕ_{MGH} and the solid line represents the uncracked yield surface ϕ_U. In Fig. 5 and 6, it is possible to observe that the validity range of the yield surface ϕ_R is limited, as previously discussed, to tension loadings. For combined load states, ϕ_{MGH} is a better description of the SEC yield surface than the equation proposed by Rice. ϕ_U is an upper-bound description of an uncracked SEC specimen, it represents a yielding locus in
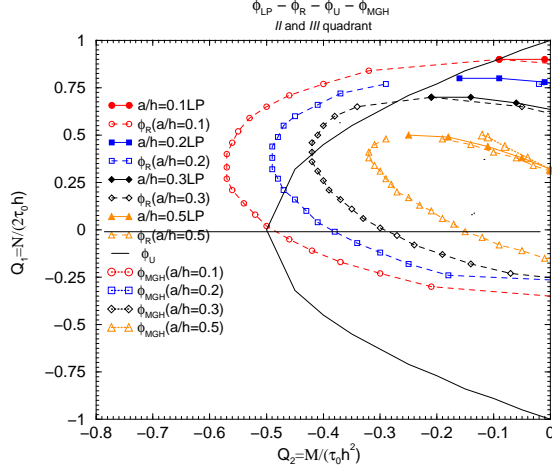
Figure 5: Combined tension and bending yield surfaces in the II and III quadrant of the generalized force space.
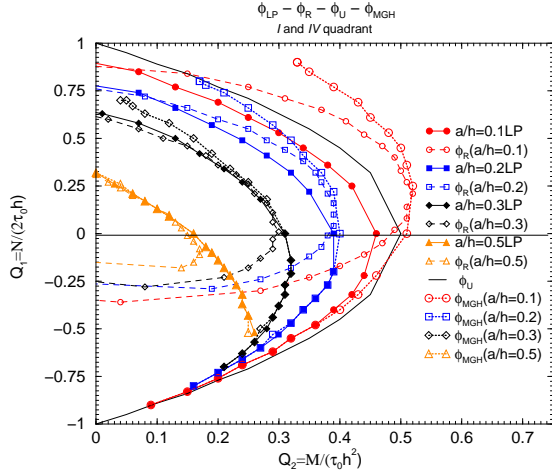
Figure 6: Combined tension and bending yield surfaces in the I and IV quadrant of the generalized force space.

which all the other surface should theoretically be contained.

4   New accurate yield surfaces

The numerically constructed yield surface proposed by Lee and Parks, see [9], characterizes the fully plastic yielding of SEC specimens having shallow, as well as, deep cracks. Numerically,

the implementation of tabulated yield surfaces for different relative crack depths in the line spring framework is infeasible.

4.1 Limit load elliptical yield surfaces

4.1.1 Double-fitting yield surface

It is, at first, chosen to represent the yield surface using a parabolic equation so that the convexity requirement for the yield surface is automatically satisfied. The proposed yield surface reads:

$$\phi_{df} = \bar{Q}_2 \hat{a}_1^{df} - \bar{Q}_1 \left(\hat{a}_2^{df} - \hat{b}_1^{df} \frac{a}{l} \right) \left(\frac{l}{h} \right) + \bar{Q}_1^2 \hat{a}_3^{df} - \hat{a}_4^{df} \left(\frac{l}{h} \right)^2 = 0 \tag{4}$$

where the coefficients $\hat{a}_i^{df}$ and $\hat{b}_i^{df}$ are functions of the relative crack depth. The term $-\bar{Q}_1 \left(\hat{a}_2^{df} - \hat{b}_1^{df} \frac{a}{l} \right)$ takes into account the "shaving-off" effects due to an additional tensile force. It is desirable to find a set of parameters $\hat{a}_i^{df}$, $\hat{b}_{i,}^{df}$ that fits the data set obtained by Parks and Lee for different relative crack depths. The coefficients of Eq. 4 are varied so that the squared difference

$$(\bar{Q}_{2_{tab}} - \bar{Q}_{2_{df}})^2 \tag{5}$$

is minimized. $\bar{Q}_{2_{tab}}$ is the normalized general abscissa of the tabulated yield surface obtained by Lee and Parks, while $\bar{Q}_{2_{df}}$ is the correspondent general abscissa obtained from the proposed yield function (Eq. 4). In order to improve the solution due to possible non-linearities of the problem in question, a quadratic extrapolation algorithm is used and, in order to guarantee convergence, the quasi-Newton method is employed. The adjustable coefficients are furthermore constrained to be positive. Different sets of values for different relative crack depths are obtained in this way . Fig. 7 shows the best possible fitting of Eq. 4, by means of the LSQ (least square) method, to the data points obtained from the continuum finite limit analysis. The parameter sets $\hat{a}_i^{df}$ and $\hat{b}_i^{df}$, obtained by the LSQ method and utilized in Eq. 4, are reported in Table 1. An attempt is now made to fit a first and second order polynomials

$$l_1 = \hat{c}_1 + \hat{c}_2 \frac{a}{h} \tag{6}$$

$$l_2 = \hat{d}_1 \left(\frac{a}{h} \right)^2 + \hat{d}_2 \left(\frac{a}{h} \right) + \hat{d}_3 \tag{7}$$

to the obtained set of points $(\frac{a}{h}; \hat{a}_i^{df})$, $(\frac{a}{h}; \hat{b}_i^{df})$, see Table 1, by means of the LSQ method. The coefficients adjusted in this second fitting procedures are the parameters $\hat{c}_1$ and $\hat{c}_2$ of Eq. 6, and $\hat{d}_1$, $\hat{d}_2$ and $\hat{d}_3$ of Eq. 7. The result of the fittings reads:

$$\hat{a}_1^{df} = \left[2 \left(\frac{a}{h} \right) + 0.7 \right] \tag{8}$$

$$\hat{a}_2^{df} = \left[0.65 \left(\frac{a}{h} \right) + 0.04 \right] \tag{9}$$

$$\hat{a}_3^{df} = \left[0.5 \left(\frac{a}{h} \right) + 0.41 \right] \tag{10}$$
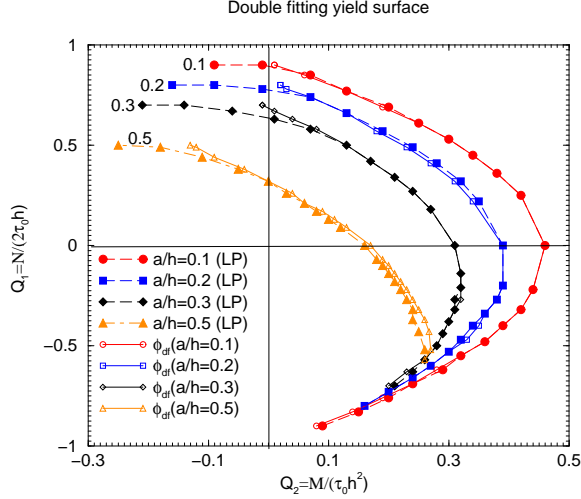
Figure 7: Combined tension and bending yield surfaces in the generalized force space. The data-point sets are represented by shaded symbols. The solid lines represent the fitting curve Eq. 4 where the values of the coefficients of the equation are reported in Table 1

Table 1: Best fitting parameters $(\hat{a}_i^{df}, \hat{b}_i^{df})$

$\frac{a}{h}$	$\hat{a}_1^{df}$	$\hat{a}_2^{df}$	$\hat{a}_3^{df}$	$\hat{a}_4^{df}$	$\hat{b}_1^{df}$
0.1	0.9	0.105	0.46	0.51	1.26
0.2	1.1	0.17	0.51	0.67	1.17
0.3	1.3	0.235	0.56	0.82	1.21
0.5	1.7	0.365	0.66	1.13	1.71

$$\hat{a}_4^{df} = \left[1.535 \left(\frac{a}{h}\right) + 0.3575\right] \tag{11}$$

$$\hat{b}_1^{df} = \left[6.875 \left(\frac{a}{h}\right)^2 - 4.375 \left(\frac{a}{h}\right) + 1.5586\right] \tag{12}$$

The use of Eq. 8-12 for the coefficients of the double fitting yield surface, gives a set of curves which are hardly distinguishable from those drawn in Fig. 7 using the coefficients reported in Table 1. In conclusion, the double fitting yield surface ϕ_{df} describes the fully plastic behavior of a SEC specimen having shallow, as well as deep, cracks in a satisfactory way and can be employed in order to describe infinitesimal crack growth.

4.1.2 Rotational elliptical yield surface

In order to obtain a simpler yield surface representation than Eq. 4, an elliptical function is considered. As before, the reason for choosing an elliptical surface is simply to meet the convexity

requirement. The yield surface reads:

$$\phi_{ro} = \left(\frac{\bar{Q}_2}{\hat{a}_1^{ro}}\right)^2 + \left(\frac{\bar{Q}_1}{\hat{a}_2^{ro}}\right)^2 - \hat{a}_3^{ro} = 0 \tag{13}$$

where $\bar{Q}_2$ and $\bar{Q}_1$ are the generalized forces normalized by means of the shear yield stress τ_0. The "shaving-off" effect is not directly taken into account in the expression of Eq. 13 in
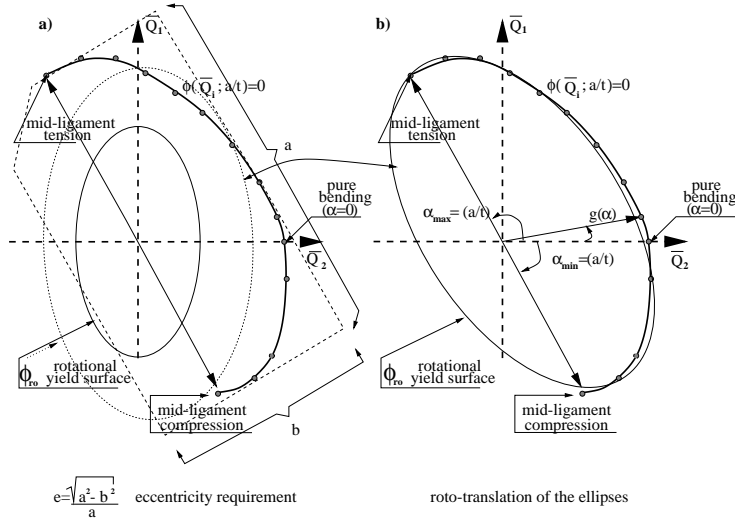
Figure 8: Schematic illustration of a constructed rotational yield surface in the generalized force space.

order to keep the proposed yield surface as simple as possible. An attempt is made to fit Eq. 13 to the set of data points obtained by the finite limit analysis for the relative crack depth $\frac{a}{h} = 0.2$. The eccentricity e^3 of the ellipses[4] ϕ_{ro} is imposed to be equal to the eccentricity of a convex piecewise rational quadratic function, [9], fitting the data set, see Fig. 8a. The eccentricity requirement is satisfied by the set of parameters $\hat{a}_i^{ro}$ reported in Table 2. Afterwards, the ellipsis is roto-translated so that the data sets obtained by the finite limit analysis are properly described. The size of the ellipses, described by the parameters $\hat{a}_i^{ro}$, is kept constant while undergoing the rigid transformations, see Fig. 8b. The translation and rotation of the ellipse of an angle $\beta\left(\frac{a}{h}\right)$ around its center C reads:

$$\left[\frac{1}{(\hat{a}_1^{ro})^2} \quad \frac{1}{(\hat{a}_2^{ro})^2} \right] \left(\mathbf{R} \left[\begin{array}{c} Q_2 \\ Q_1 \end{array} \right] \right)^2 = \hat{a}_3^{ro}. \tag{14}$$

---

[3]The eccentricity is defined as: $e = \frac{\sqrt{a^2-b^2}}{a} \leq 0$ where $a = \sqrt{\hat{a}_3^{ro}(\hat{a}_1^{ro})^2}$ and $b = \sqrt{\hat{a}_3^{ro}(\hat{a}_2^{ro})^2}$, see [29]

[4]The ellipsis is the geometric locus of points P for which the sum of the distance from 2 fixed points L_1 and L_2 is constant. $|P - L_1| + |P - L_2| = 2a$ (the constant 2a describes the size of the ellipse)

where $Q_1 = \overline{Q}_1 - B$ and $Q_2 = \overline{Q}_2 - A$ represent the translation of the ellipsis and the rotation tensor $\mathbf{R}$ employed in order to describe a rotation of the ellipsis around its center:

$$\mathbf{R} = \left[\begin{array}{cc} cos(\beta) & -sin(\beta) \\ sin(\beta) & cos(\beta) \end{array} \right] \tag{15}$$

The "shaving-off" effect due to an additional tensile force is described by roto-translating the yield locus. The shaded symbols in Fig. 9 and 10 represent the sets of data obtained from the continuum finite limit analysis while the empty ones represent the rotational yield surface. Fig.

Table 2: Best fitting parameters ($\hat{a}_i^{ro}$, A, B and β in radians)

$\frac{a}{h}$	$\hat{a}_1^{ro}$	$\hat{a}_2^{ro}$	$\hat{a}_3^{ro}$	A	B	$\beta(rad)$
0.1	0.96	1	1.18	-0.59	-0.12	3.17
0.2	0.96	1	1.18	-0.65	-0.15	3.17
0.3	0.96	1	1.18	-0.73	-0.16	3.16
0.5	0.96	1	1.18	-0.88	0.07	3.00
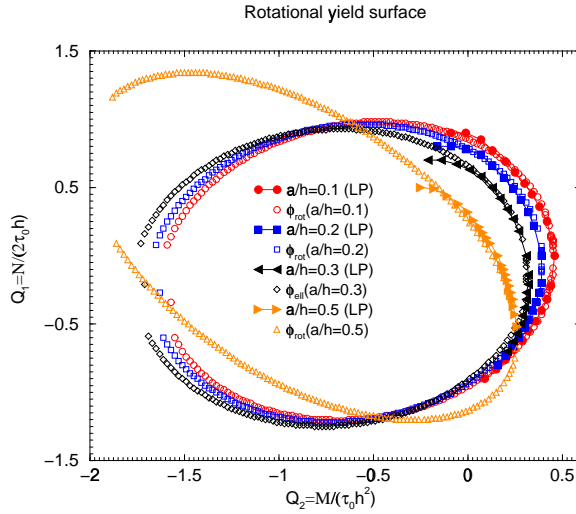
Figure 9: Combined tension and bending rotational yield surfaces in the generalized force space.

9 and 10 show that Eq. 13 fits the numerical sets of data well . The parameters describing the magnitude of the roto-translation of the system β, A and B are reported in Table 2. The first and second order polynomials Eq. 6, 7 are fitted to the obtained set of points $\left(\frac{a}{h}; A\right)$, $\left(\frac{a}{h}; B\right)$ and $\left(\frac{a}{h}; \beta\right)$. The result of the double-fitting procedure reads:

$$A = \left[-0.55 \left(\frac{a}{h} \right) - 0.55 \right] \tag{16}$$

11
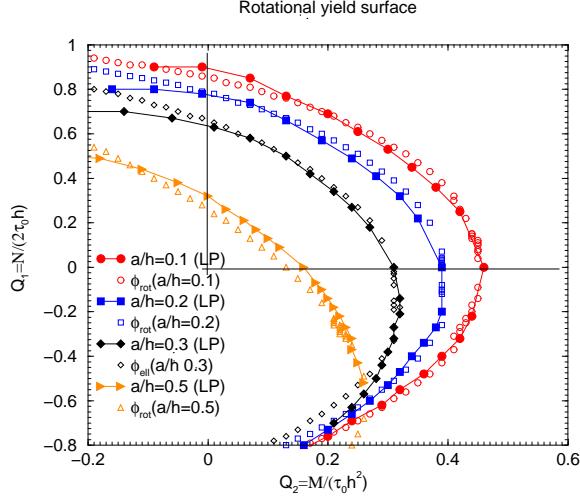
Figure 10: Combined tension and bending rotational yield surfaces in the generalized force space in a limited domain.

$$B = \left[0.5 \left(\frac{a}{h} - 0.3 \right)^2 - 0.2 \right] \tag{17}$$

$$\beta = \left[-0.225 \left(\frac{a}{h} \right) + 3.2125 \right] \tag{18}$$

ϕ_{ro} can be employed in order to describe infinitesimal crack growth because of its simplicity.

4.1.3 Elliptical yield surface

A new elliptical yield surface is considered:

$$\phi_{el} = \left[\frac{\overline{Q}_2 - \hat{a}_1^{el}}{\hat{a}_2^{el}} \right]^2 + \left[\frac{\hat{b}_1^{el}(\overline{Q}_2 + \hat{b}_5^{el}) + \hat{b}_2^{el}(\overline{Q}_1 - \hat{b}_4^{el})}{\hat{b}_3^{el}} \right]^2 - \hat{c}_1^{el} = 0 \tag{19}$$

The equation proposed here, in order to represent the yield surface for the SEC specimen, contains a mixed term which intrinsically takes into account the rotation of the ellipses in the force space $\overline{Q}_1 - \overline{Q}_2$. Eq. 19 is fitted, at first, to the sets of data points obtained from the finite limit analysis. In order to simplify the fitting procedure, $\hat{b}_3^{el}$ and $\hat{c}_1^{el}$ are kept constant. The coefficient of the mixed term, $\hat{b}_1^{el} \hat{b}_2^{el}$ describes the angle of rotation of the ellipse represented by Eq. 19. The best possible set of fitting parameters $\hat{a}_i^{el}$, $\hat{b}_i^{el}$ and $\hat{c}_i^{el}$ is found by means of the least square method, see Table 3, Fig. 11 and 12. As previously we try to fit a first and a second order polynomials, Eq. 6 and 7 to the obtained set of points $\left(\frac{a}{h}; \hat{a}_i \right)$, $\left(\frac{a}{h}; \hat{b}_i \right)$, see Table 1, by means of the LSQ method. Eq. 19 is very sensitive for any small change of the parameters so that fitted polynomials are not good enough for our purpose. In order to bypass the sensitivity problem a fourth order Lagrange interpolation polynomial can be used. This leads to a far too complicated description of the yielding surface which seems not to be suitable to describe infinitesimal crack growth.

Table 3: Best fitting parameter ($\hat{a}_i^{el}$, $\hat{b}_i^{el}$, $\hat{c}_i^{el}$).

$\frac{a}{h}$	$\hat{a}_1^{el}$	$\hat{a}_2^{el}$	$\hat{b}_1^{el}$	$\hat{b}_2^{el}$	$\hat{b}_3^{el}$	$\hat{b}_4^{el}$	$\hat{b}_5^{el}$	$\hat{c}_1^{el}$
0.1	-0.677	1.14	-0.27	1.7	2	0.1	0.14	1
0.2	-1.0605	1.45	-0.33	1.5	2	0.35	1	1
0.3	-1.445	1.77	-0.16	1.3	2	0.6	3.2	1
0.5	-2.211	2.47	-0.13	1.22	2	1.1	6.2	1
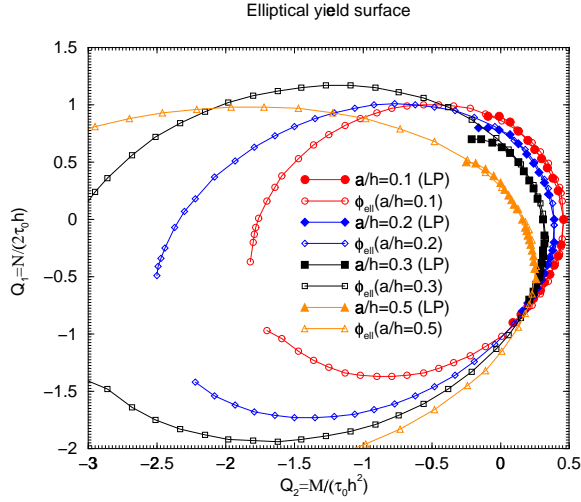
Figure 11: Combined tension and bending yield surfaces in the generalized force space. The data points sets are represented by filled symbols. The solid line represents the fitting curve Eq. 19.

5 Qualitative verification of the proposed yield surfaces

5.1 A symmetric yielding locus, ϕ

The double fitting yield surface, Eq. 4, is a parabolic function, therefore its validity is confined mainly to the I and IV quadrants of the generalized force space. ϕ_{df} does not describe the yielding behavior in the negative sector of the generalized force space in a correct way. An alternative function, located in the upper bound limit, has to be implied in these quadrants of the $\overline{Q}_2$-$\overline{Q}_1$ force space.

Under compression, the magnitude of the yielding stress is expected to be just slightly less than what obtained for the uncracked specimen. In this loading state, in fact, the specimen can be thought as if it was uncracked. These observations can be generalized to the bending loading. The function ϕ_{df}^s, symmetric to ϕ_{df} with respect to the line $\overline{Q}_1 = tg(\frac{\pi}{2} + \alpha)\overline{Q}_2$, can be used in order to describe this yielding behavior in the II and III quadrants. The angle α between the
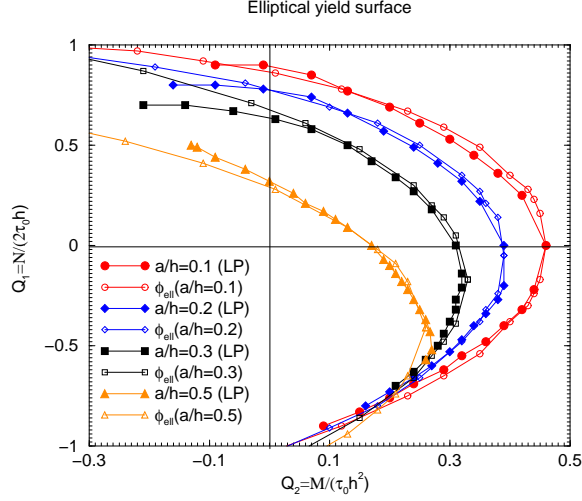
Figure 12: Combined tension and bending yield surfaces in the generalized force space in a limited domain.

symmetry line and the Q_1-axis is a linear function of the relative crack depth $\frac{a}{h}$:

$$\alpha(\frac{a}{h}) = \frac{\pi}{6}\frac{a}{h}. \tag{20}$$
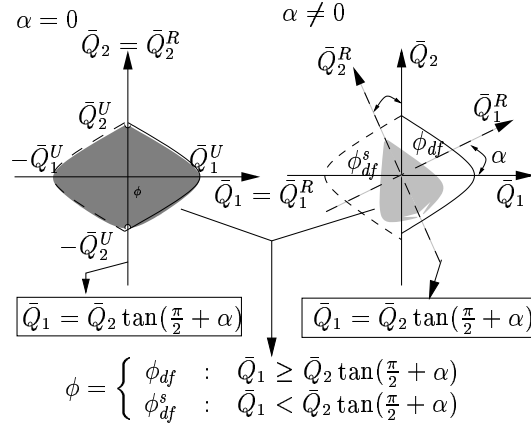
Figure 13: Schematical construction of a symmetric yielding locus

Fig. 13 schematically represents the symmetric yielding locus constructed with ϕ_{df} and ϕ_{df}^s. The double-fitting yielding surface can be written in a simpler way as

$$\phi_{df} = A\bar{Q}_2 + B\bar{Q}_1 + C\bar{Q}_1^2 + D = 0 \tag{21}$$

14

where $A = \hat{a}_1^{df}$, $B = -\left(\hat{a}_2^{df} - \hat{b}_1^{df}\frac{a}{l}\right)(a/l)$, $C = \hat{a}_3^{df}$, $D = -\hat{a}_4^{df}(a/l)^2$. The parameters a_i^{df} and $\hat{b}_i^{df}$ are functions of the relative crack depth, as discussed in section 4.1.1. The function ϕ_{df}^s, symmetric to the double fitting yield surface, reads:

$$
\begin{aligned}
\phi_{df}^s &= -A[\bar{Q}_2 \cos 2\alpha + \bar{Q}_1 \sin 2\alpha] \\
&+ B[-\bar{Q}_2 \sin 2\alpha + \bar{Q}_1 \cos 2\alpha] \\
&+ C[\bar{Q}_2 \sin 2\alpha - \bar{Q}_1 \cos 2\alpha]^2 + D = 0
\end{aligned} \tag{22}
$$

The symmetrical yielding locus ϕ is constructed by using both the double fitting yield surface and its symmetric counterpart. It is valid for the whole force space and reads:

$$
\phi = \begin{cases} \phi_{df} &: \quad \bar{Q}_1 \geq \bar{Q}_2 \tan(\frac{\pi}{2} + \alpha) \\ \phi_{df}^s &: \quad \bar{Q}_1 < \bar{Q}_2 \tan(\frac{\pi}{2} + \alpha) \end{cases} \tag{23}
$$
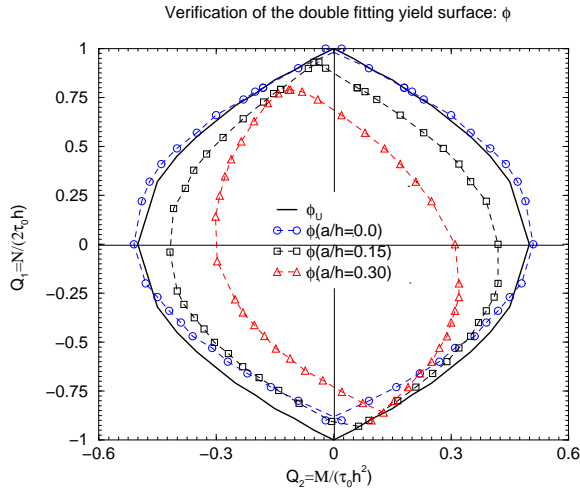
Figure 14: Qualitative verification of the double fitting yield surface

A qualitative verification of the proposed yield surfaces is carried out by plotting the upper-bound yield surface, Eq. 3, with the proposed yield surfaces ϕ. The solid line in Fig. 14 represents the upper-bound yield surface while the dashed line which interpolates the empty circle-points, represents the double-fitting yield surface for an uncracked SEC specimen $\frac{a}{h} = 0$. The agreement between ϕ_U and ϕ_{df} is good. It is useful to emphasize that the symmetrical yielding locus ϕ is an even function when it is expressed in the rotated coordinate system $\overline{Q}_2^{\mathbf{R}}$-$\overline{Q}_1^{\mathbf{R}}$:

$$
\phi(\overline{Q}_2^{\mathbf{R}}, \overline{Q}_1^{\mathbf{R}}) = \phi(-\overline{Q}_2^{\mathbf{R}}, \overline{Q}_1^{\mathbf{R}}). \tag{24}
$$

The convexity requirements for the yield function ϕ are satisfied in the whole $\overline{Q}_2$-$\overline{Q}_1$ force space. The intersection points of the two yielding surfaces, see Fig. 13, need to be treated in a careful way during the numerical implementation of the yield locus since its first derivative is discontinuous in these points.

5.2 Combination of the rotational yielding surface and of the upper bound solution, $\hat{\phi}$

The validity of the rotational yield surface is, as for the double-fitting yield function, mainly confined to the I and IV quadrants of the generalized force space. The yielding behavior in the negative sector of the generalized force space is not described in a satisfactory way. ϕ_{ro} is located outside the locus described by ϕ_U which is, as discussed in section 3.1.2, an upper-bound solution for the yielding locus. An alternatilve yielding surface $\hat{\phi}$ is constructed by using a combination of both the rotational yield surface and the upper-bound solution and reads:

$$\hat{\phi} = \begin{cases} \phi_{ro} & : & \bar{Q}_2 \geq 0 & \vee & (\bar{Q}_2 < 0 & \wedge & \phi_{ro} \leq \phi_U) \\ \phi_U & : & \bar{Q}_2 < 0 & \wedge & \phi_{ro} > \phi_U \end{cases} \tag{25}$$

Once again, the convexity requirements for the yield function $\hat{\phi}$ are satisfied in the whole $\overline{Q}_2$-$\overline{Q}_1$ force space. The intersection points of the two yielding surfaces need to be treated in a special way during the numerical implementation of the yield locus since the first derivative of $\hat{\phi}$ is not continuous at the intersection point.

5.3 Observations

The symmetric yielding locus ϕ, Eq. 23, is to be preferred because it is a better description of the overall yielding behavior at the rest ligament of the SEC specimen.

6 Numerical implementation of the proposed yield surface

The details of the implementation of the backward Euler integration scheme at the integration point of the line spring element in order to account for plasticity are presented here shortly for the case of an elastic-perfectly plastic material.

6.1 Numerical procedure for returning to the yield surface

A return mapping algorithm provides an effective and robust integration scheme of the rate constitutive equations at the integration point of the line spring element. Geometrically, it amounts to finding the closest distance of a point to a convex set, ϕ, see [22] and [5] . At a time increment Δt_n, estimates of the elastic predictor $\Delta \mathbf{q}$ are presumed known. The generalized force rate $\Delta \mathbf{Q}$, due to the elastic predictor, is obtained so that the force state at point B is calculated. $\mathbf{Q}^B$ will most likely not satisfy the consistency rule $\phi = 0$, therefore, a plastic corrector $\Delta \lambda \mathbf{a}_B$ is used as first corrector, where $\mathbf{a}_B$ is the radiant to the yield surface at point B

$$\mathbf{a}_B = \frac{\partial \phi}{\partial \mathbf{Q}}|_B. \tag{26}$$

The generalized force estimate at point C:

$$\mathbf{Q}^C = \mathbf{Q}^B - \Delta \lambda \mathbf{D} \mathbf{a}_B \tag{27}$$

will not always lie on the yield surface, and, therefore, further iterations are required in order to find a force state which satisfies the constitutive law. The backward Euler return is based on the equation

$$\mathbf{Q}^C = \mathbf{Q}^B - \Delta\lambda \mathbf{D}\mathbf{a}_C \qquad (28)$$

where $\mathbf{a}_C$ is the radient to the yield surface at the final force state C. The details of the iterative loop used in order to correct $\mathbf{Q}^C$ and $\Delta\lambda$ to the right solution, can be found in [22], [23], [5] and [6].

6.1.1 Pragmatic solution at the corners

The yield surface ϕ, Eq. 23, used here, has corners located on the line $Q_1 = Q_2 \tan(\frac{\pi}{2} + a)$. There exist different solutions which can be implemented at the corners in the case when two active yield surfaces are active, see [21] and [6]. In this study, a pragmatic return to the yield surface from the corner is adopted. The "normal" at the corner is not unique, there exists a normal for the double-fitting yield surface and one for its symmetric counterpart. In order to solve this non-uniqueness problem, we consider the function ϕ_{df} to be the "master" curve so that the "normal" at the corner is calculated for this curve. The normal is now uniquely defined. When $\phi_{df} = 0$, ϕ^s_{df} is checked. If this is violated further iterations coments. The numerical implementation is in this way kept as simple as possible.

6.1.2 Accuracy analysis. Iso-error maps

Iso-error maps provide a systematic approach to test the accuracy of the implemented algorithm. The iso-errors map is constructed selecting a sequence of specified normalized displacement
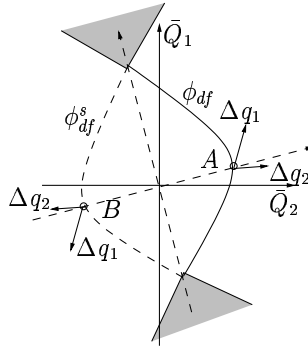
Figure 15: Symmetric yield surface: points for iso-errors maps.

increments for two symmetric force states A and B. The generalized forces corresponding to the prescribed displacement are computed by the algorithm. Results are reported in terms of the relative root mean square of the error between the exact and computed solution:

$$\chi = \frac{\sqrt{[\mathbf{Q} - \mathbf{Q}^*][\mathbf{Q} - \mathbf{Q}^*]^T}}{\sqrt{\mathbf{Q}^* \mathbf{Q}^{*T}}} \times 100 \qquad (29)$$

17

where $\mathbf{Q}$ is the result obtained by application of the algorithm and $\mathbf{Q}^*$ is the "exact" solution corresponding to the specific strain increment. The "exact" solution is obtained by a subincrementation of the strain increment, see [5]. The iso-error maps shown in Fig. 16 are obtained

Iso−error map at point A and B
χ is reported next to each iso−error curve
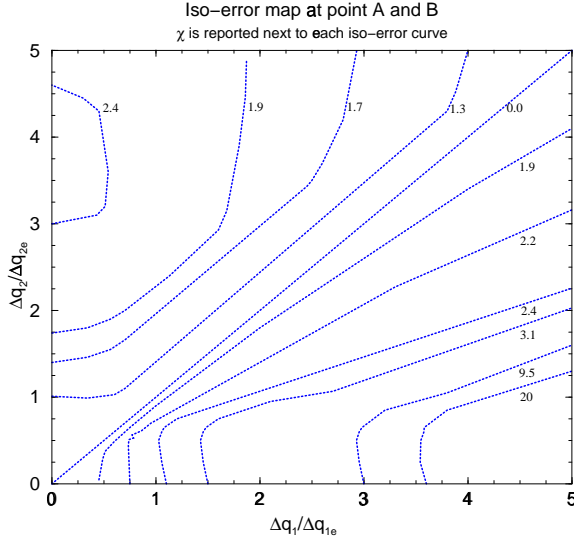
Figure 16: Iso-error maps for two symmetric force states A and B.

for the yield surface ϕ, Eq. 23, in the case of ideal plasticity. $\Delta q_2/\Delta q_{2e}$ and $\Delta q_1/\Delta q_{1e}$ are the components of the elastic predictor normalized by means of the elastic displacement associated with initial yielding. The iso-error maps for the two symmetric force states are, as expected, the same, see Fig. 16. The error is contained in a range satisfactory for engineering aplication. The accuracy of the solution decreases when the force state due to the trial increment $\mathbf{Q}^B$ is located in the dashed area of Fig.15. In this case both yielding surfaces are active and have to be satisfied at the end of the integration algorithm. The solution is more sensitive on the displacement increment in these areas of the force space.

7 Summary

This study presents alternative description of the yield surface of SEC specimen under combined tension and bending loads. The proposed yield surfaces provide a satisfactory description of the fully plastic yielding of both shallow, as well as deep, cracks.

The numerical implementation of an elastic predictor plastic corrector itegration scheme is also presented in order to take into account plastic behavior. The accuracy analysis of the algorithm is carried out showing an overhall satisfactory behavior.

Work is in progress to implement the inelastic line spring element in the framework of a commercial FEM program.

A Formulation of the Line-Spring element

- The crack line, Fig 1a, is discretized into a finite number of line spring elements.

- The line spring element can be schematically represented by two straight lines $\overline{14}$ and $\overline{23}$ connected to each other by a series of springs as seen in Fig. 17. At zero deformation the lines lie upon each other. When deformation takes place each line displaces in opposite direction. The displacement is constrained by the springs.
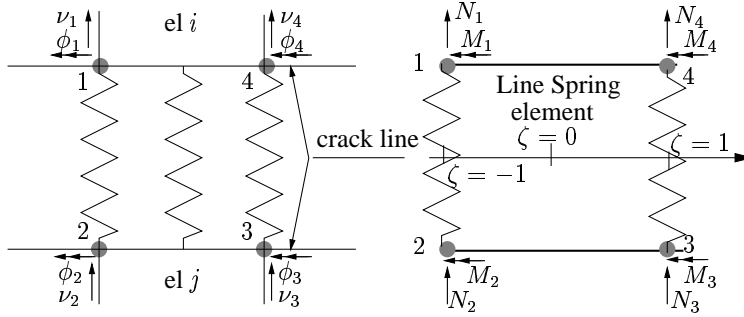
Figure 17: Line spring element.

- Let $\mathbf{q_A} = [\delta_\mathbf{A}, \theta_\mathbf{A}]^\mathbf{T}$ and $\mathbf{q_B} = [\delta_\mathbf{B}, \theta_\mathbf{B}]^\mathbf{T}$ be the generalized displacements of the line spring at $\zeta = \mp 1$ respectively. The relation between the generalized displacements and the nodal displacements (ν_i, ϕ_i) reads:

$$\delta^* = \mathbf{N}^* \nu_\mathbf{e} \tag{30}$$

$$\delta^* = \begin{bmatrix} \delta_A \\ \theta_A \\ \delta_B \\ \theta_B \end{bmatrix} \quad \mathbf{N}^* = \begin{bmatrix} 1 & 0 & -1 & 0 & 0 & 0 & 0 & 0 \\ 0 & 1 & 0 & -1 & 0 & 0 & 0 & 0 \\ 0 & 0 & 0 & 0 & -1 & 0 & 1 & 0 \\ 0 & 0 & 0 & 0 & 0 & -1 & 0 & 1 \end{bmatrix} \quad \nu_\mathbf{e} = \begin{bmatrix} \nu_1 \\ \phi_1 \\ \nu_2 \\ \phi_2 \\ \nu_3 \\ \phi_3 \\ \nu_4 \\ \phi_4 \end{bmatrix}$$

The generalized displacement $\mathbf{q} = [\delta, \theta]^\mathbf{T}$ at an arbitrary point $|\zeta| \leq 1$ is assumed to vary linearly within the element. This reads:

$$\mathbf{q} = \mathbf{N}\delta^* \tag{31}$$

$$\mathbf{q} = \begin{bmatrix} \delta(\zeta) \\ \theta(\zeta) \end{bmatrix} \quad \mathbf{N} = \begin{bmatrix} \hat{N}_1 & 0 & \hat{N}_2 & 0 \\ 0 & \hat{N}_1 & 0 & \hat{N}_2 \end{bmatrix} \quad \delta^* = \begin{bmatrix} \delta_A \\ \theta_A \\ \delta_B \\ \theta_B \end{bmatrix}$$

where

$$\hat{N}_1 = \frac{1-\zeta}{2} \qquad\qquad \hat{N}_2 = \frac{1+\zeta}{2} \tag{32}$$

- The equivalent nodal forces (N_i, M_i) are calculated as follows:

$$
\begin{bmatrix} N_1 \\ M_1 \\ N_4 \\ M_4 \end{bmatrix} = - \begin{bmatrix} N_2 \\ M_2 \\ N_3 \\ M_3 \end{bmatrix} = \int_{L_e} \begin{bmatrix} \hat{N}_1 & 0 \\ 0 & \hat{N}_1 \\ \hat{N}_2 & 0 \\ 0 & \hat{N}_2 \end{bmatrix} \begin{bmatrix} N \\ M \end{bmatrix} ds. \tag{33}
$$

The vector $\mathbf{F}_e = [N_1, M_1, N_2, M_2, N_3, M_3, N_4, M_4]^T$ is expressed as outlined above, Eq.33, and reads:

$$\mathbf{F}_e = \int_{L_e} \begin{bmatrix} \begin{bmatrix} \mathbf{N}^T \end{bmatrix} \\ -\begin{bmatrix} \mathbf{N}^T \end{bmatrix} \end{bmatrix} \begin{bmatrix} N \\ M \end{bmatrix} ds. \tag{34}$$

- The relation between the generalized force $\mathbf{Q} = [N, M]^T$ and the corresponding generalized displacement $\mathbf{q}$ at a generic point $|\zeta| \leq 1$ reads:

$$\mathbf{Q} = \mathbf{D}\mathbf{q}. \tag{35}$$

where $\mathbf{D}$ is the stiffness matrix of the line spring at point ζ evaluated as outlined in literature [18].

- the substitution of Eq. 31 and Eq. 32 into Eq. 35 leads to:

$$\mathbf{Q} = \mathbf{D}\mathbf{N}\mathbf{N}^*\nu_{\mathbf{el}} \tag{36}$$

where the matrix multiplication $\mathbf{N}\mathbf{N}^*$ is observed to be equal to $\mathbf{N}^{**} = ([N], -[N])$. Taking into account this observation and substituting Eq. 36 into Eq. 34, we can write the stiffness equation for the line spring element as

$$\mathbf{F}_e = \int_{L_e} \mathbf{N}^{**^T}\mathbf{D}\mathbf{N}^{**}ds\nu_{\mathbf{el}} \tag{37}$$

The line spring element formulated here is compatible with a two-dimensional plate or shell element with four nodes.

B   Accounting for elastoplasticity in the Line-Spring element

For plastic conditions, only the mode I case will be considered. It was solved for the line-spring in terms of the upper bound solution (slip line field, colored area in Fig. 2). The derivation of

the mode-I line-spring follows the classical plasticity theory, [20] :

$$\phi(\mathbf{Q}, \sigma_{\mathbf{Y}}^{\mathbf{LS}}; \mathbf{a}) = \mathbf{0} \tag{38}$$

$$d\phi = \frac{\partial \phi}{\partial \mathbf{Q}} d\mathbf{Q} + \frac{\partial \phi}{\partial \sigma_{\mathbf{Y}}} \mathbf{d}\sigma_{\mathbf{Y}}^{\mathbf{LS}} = \mathbf{0} \tag{39}$$

$$d\mathbf{q_p} = \mathbf{d}\lambda \frac{\partial \phi}{\partial \mathbf{Q}} \tag{40}$$

$$d\mathbf{q} = d\mathbf{q_e} + d\mathbf{q_p} \tag{41}$$

$$d\mathbf{Q} = \mathbf{D_{ep}} \cdot \mathbf{dq} \tag{42}$$

$$d\mathbf{Q} = \left(\mathbf{D_{el}} - \frac{\left(\frac{\partial \phi^{\mathbf{T}}}{\partial \mathbf{Q}} \mathbf{D_{el}} \right)^{\mathbf{T}} \left(\frac{\partial \phi^{\mathbf{T}}}{\partial \mathbf{Q}} \mathbf{D_{el}} \right)}{\frac{\partial \phi^{\mathbf{T}}}{\partial \mathbf{Q}} \mathbf{D_{el}} \frac{\partial \phi}{\partial \mathbf{Q}} - \frac{\partial \phi^{\mathbf{T}}}{\partial \mathbf{Q}} \mathbf{Q} \frac{\partial \phi}{\partial \sigma_{\mathbf{Y}}^{\mathbf{LS}}} \frac{\mathbf{E_p}}{\sigma_{\mathbf{y}}^{\mathbf{LS}} \mathbf{kl}^{\mathbf{n'}}}} \right) \mathbf{dq} \tag{43}$$

Parks and White (1982), argue that the exponent n' of Eq. 43 is 2 and the k-factor of order unity, l is the length of the rest ligament and σ_Y^{LS} is the yield stress for the line spring. Note that k, l and n' are the quantities controlling the plasticity in the ligament region, $kc - zone$ in Fig 2. The representation of the yield surface proposed in this study, ϕ_{df}, is used here in order to describe the stress field of the line-spring. Having determined the plastic deformation increment, the crack-tip opening displacement is obtained from:

$$d\delta_p = du_p + \left(\frac{h}{2} - a \right) d\theta_p. \tag{44}$$

The validity of this relation was investigated by Lee and Parks, [10]. Their results show that for shallow edge cracks ($a/h \leq 0.2$), the relation is inaccurate, [10]. Employing the connection between the J_p and the Dugdale crack tip solution corrected for constraint, one has:

$$dJ_p = m\sigma_Y^{LS} d\delta_p \tag{45}$$

Here, m is a function of crack geometries and hardening characteristics. The total J integral may now be calculated:

$$J = J_e + J_p \tag{46}$$

As the edge-crack is the basic case for the line spring, computed values of J for a surface crack will be more accurate in the center compared to positions approaching the surface at the crack ends.

Acknowledgements

21

References

[1] Hibbit Karlson and Sorenson., ABAQUS Manual, version 5.2.

[2] Betegon C. and Hancock J.W., Two Parameters Characterization of the Elastic-Plastic Crack Tip Field. *Journal of Applied Mechanics.* 58, 104-110, 1991.

[3] British Standard 7910 Guide on methods for assessing of flaw in fusion welded structures. 7910:1999.

[4] **Paper I:** Chiesa M., Skallerud B. and Thaulow C., Line spring elements in a yield strength mismatch situation with application to welded wide plates. To appear in *Engineering Fracture Mechanics*.

[5] Crisfield M.A. Non-linear Finite Element Analysis of Solid and Structures *Vol 1.*

[6] Crisfield M.A. Non-linear Finite Element Analysis of Solid and Structures *Vol 2.*

[7] Kirks M.T., Dodds R. H. Jr. and Anderson T.L., Approximate Techniques for predicting Size Effects on Clevage Fracture Toughness. *Fracture Mechanics: 24th Volume.* ASTM STP 1207.

[8] Hancock J.W., Reuter W.G. and Parks D. M., Constraint and Toughness Parameterized by T. *Int.J. Solids Structures* 32, 2393-2418, 1995.

[9] Lee H. and Parks D. M., Fully plastic analysis of plane strain single edged cracked specimen subjected to combined tension and bending. *Int.J. Frac.* 63, 329-349, 1993.

[10] Lee H. and Parks, D. M., Enhanced elastic-plastic line spring finite element. *Constraint Effect in Fracture* ASTM STP 1171, 1993.

[11] Milne, I., Ainsworth R. A., Dowling A. R. Stewart A. T. Assessment of the Integrity of Structures Containing Defects. *Central Electricity generating board report* R/HR6-rev 3, 1986.

[12] Nyhus B., OGT Repair Welding. *SINTEF REPORT.* open report, 1999.

[13] Ørjasæter O. and Nyhus B. AiS: Fatigue and fracture mechanics testing of MIG and FS welded panels. *SINTEF report.* Open report, 1999.

[14] Nyhus B., Oseberg Hyperbaric welding procedure development. Fracture mechanics testing and ECA analysis. *SINTEF report.* Unrestricted, 1998.

[15] Parks D. M., A stiffness derivate finite element technique for the determination of crack tip stress intensity factors. *Int.J. Frac.* 487-502, 1974.

[16] Parks D. M., The inelastic line spring: estimates of elastic-plastic fracture mechanics parameter for surfaced cracked shells. *J. Press. Vessel Tech.* 103, 264-254, 1981.

[17] Parks D. M. and White, C. S., Elastic-plastic line spring finite elements for surface cracked plates and shells . *J. Press. Vessel Tech*. 104, 287-292, 1982.

[18] Rice J. R., A path independent integral and the appropriate analysis of strain concentration by notches and cracks. *J. Applied Mech*. 35, 379-386, 1968.

[19] Rice J. R. and Levy, N., The part through surface crack in an elastic plate. *J. Applied Mech*. 185-194, 1968.

[20] Rice J. R., The line spring model for surface flaws. *The Surface Crack Physical Problems and Computer Solutions*. (ed J. L. Sweldow), ASME 1972.

[21] Simo J. C., Kennedy J. C. and Govindee S. Non-smooth multisurface plasticity and viscoplasticity. Loading/unloading conditions and numerical algorithms. *International Journal for numerical methods in Engineering*. 26, 2161-2186 1988.

[22] Simo J. C., Taylor R. L. Consistent tangent operators for rate-independent elastoplasticity. *Computer methods in applied mechnanics and engineering*. 48, 101-118 1985.

[23] Simo J. C., Taylor R. L. A return mapping algorithm for plane stress elastoplasticity. *International Journal for numerical methods in Engineering*. 22, 649-670, 1986.

[24] Skallerud B., Inelastic line springs in nonlinear analysis of cracked tubular joint. *Fatigue Fract. Engng Mat. Struct*. 18,463-477, 1996.

[25] Skallerud B., A mixed mode I/II inelastic line spring. *Int. J. Solids Structures*. 33,4143-4166, 1996.

[26] Wang Y. Y., Parks, D. M., Evaluation of the elastic T-stress in surface crcaked plates using the line-spring method. *Int.J. Frac.*. 56, 25-40, 1992.

[27] Williams M.L., On the Stress Distribution at the Base of a Stationary Crack. *J. Applied Mech*. Vol 24, 109-114, 1957.

[28] Zhang Z.L., Hauge M. and Thaulow, C., Two Parameter Characterization of the Near Tip Stress Fields for a Bi-Material Elastic-Plastic Interface Crack . *Int. Journal of Fracture*. 79,65-83, 1996.

[29] Merziger G. and Wirth T. Repetitorium der h"o"heren mathematik. *Binomi*. 2. Aufgabe, 1993.

Efficient numerical procedures for fracture assessments of surface cracked shells

Matteo Chiesa and Bjørn Skallerud
Department of Mechanical Engineering
Norwegian University of Technology, Trondheim, Norway
e–mail: matteo.chiesa@matek.sintef.no
e–mail: bjorn.skallerud@maskin.ntnu.no

Bård Nyhus
SINTEF Materials Technology, Trondheim, Norway
Dept. of Fracture Mechanics and Materials Testing
e–mail: bard.nyhus@matek.sintef.no

Abstract. *The line spring finite element is a versatile numerical tool for performing engineering fracture mechanics analysis of surface cracked shells. An accurate yield surface of plane strain single-cracked (SEC) specimens having shallow, as well as deep, cracks is here implemented in order to improve the overall performance of the line spring element. The details of the implementation of the backward Euler integration scheme at the integration point of the line spring element in order to account for plasticity are presented here for a bilinear material model. The improved line spring element is utilized within a new failure assessment approach. Shell line spring calculations are performed in order to calculate the constraint level of a pipe with surface or through the thickness cracks. A SENT specimen is designed to give a constraint level comparable to the one calculated for the pipe. The constraint corrected specimen is furthermore tested in order to obtain a $CTOD - \Delta a$ curve.*
The present study presents, furthermore, an efficient numerical procedure, based on the $CTOD - \Delta a$ curve obtained, in order to account for ductile crack growth within the line spring framework. A numerical case is presented in order to show that the proposed procedure is suited to account for ductile crack growth.

1   Introduction

Surface cracked shell structures occur in many applications, e.g. pipelines, offshore structures, pressure vessels etc. The defects are usually introduced during the welding process. The direct discretization of the cracked shell structure with solid finite elements in order to compute the fracture mechanics quantities leads to large size problems, and makes such analysis infeasible in most cases. In order to directly calculate the fracture mechanics parameters in structural analysis, a combination of shell [1] and line spring finite elements [2] instead of solid finite elements is an attractive option. The line spring element can be schematically represented by two straight lines $\overline{14}$ and $\overline{23}$ connected to each other by a series of springs as seen in Fig. 15c see Appendix A. At zero deformation the lines lie upon each other. When deformation takes place each line displaces in opposite direction. The displacement is constrained by the springs. The stiffness of the line spring is derived from a plane strain SEC (single edged cracked) specimen under tension and bending. The general yield surfaces ϕ see [3], governing the plastic behavior of cracked shell section ligament, is plotted in the generalized force space $Q_{1,2}$ for different crack depth to thickness ratio $\frac{a}{h}$, see Fig. 15a. ϕ contains more accurate information about the general yielding behavior of shallow, as well as deep cracks, for the SEC specimen than the typically employed yield surfaces.

A new concept for failure assessment for low constraint applications is developed, see [4], [5]. It reduces the conservatism of the standard failure analysis, see [6]. The method is based on the testing of constraint-corrected single-edge-notched specimens under tension (SENT). The method has been used in several pipe-laying projects. By varying the crack length and the distance between the clamps when the test is performed these specimens can be designed to give a constraint level comparable to that of a pipe with surface or through the thickness cracks. FE calculation of both the SENT and the pipe are necessary to design SENT specimens with a constraint level comparable to the pipe. The discretization of the cracked shell structure is performed by combining shell and line spring finite elements. A SENT specimen is designed here as outlined in [6]. The SENT specimen has a constraint level comparable to that calculated for the pipe. The constraint corrected specimen is then tested in order to obtain a curve for tip opening displacement versus crack growth $CTOD - \Delta a$.

In order to simulate inelastic behavior and ductile crack growth within the line spring framework, the generalized force state accounting for plasticity is updated considering the yield surface size "frozen" with respect to crack depth to thickness ratio ($\frac{a}{h} = const$). Then the crack tip-deformation parameter $CTOD$ see [2], is computed by using the updated generalized displacement state at the integration point. The calculated value of $CTOD$ is used in a $CTOD - \Delta a$ curve, developed here, in order to quantify the amount of crack growth Δa. Then the yield surface is updated due to crack growth, and a cutting plane algorithm is used to iterate the generalized force solution previously obtained back to the new yield surface in order to satisfy the consistency requirement. The details of the implementation of the backward Euler integration scheme at the integration point of the line spring element in order to account for plasticity and crack growth are presented here for a bilinear material model, see [3], [7].

2 Theoretical background

2.1 Surface cracked shell

The part-through surface crack is originally a three dimensional problem as seen in Fig. 1a. Here $a(x_1)$ is the crack depth at x_1. The three dimensional problem is formulated within the context of two-dimensional plate or shell theory with the part-cracked section represented as a line-spring. The line-springs take into account the additional flexibility due to the surface crack. The

Yield surface	$\phi(\bar{Q}_1, \bar{Q}_2, \sigma_y; c) = \begin{cases} \phi_{df} & : \quad \bar{Q}_1 \geq \bar{Q}_2 \tan(\frac{\pi}{2} + \alpha) \\ \phi_{df}^s & : \quad \bar{Q}_1 < \bar{Q}_2 \tan(\frac{\pi}{2} + \alpha) \end{cases}$
	$Q_1 = N \quad Q_2 = M$
	$\bar{Q}_1 = \frac{N}{2\tau_0 h} \quad \bar{Q}_2 = \frac{M}{\tau_0 h^2} \quad c = h - a$
Work hardening	$dW_p = \mathbf{Q}^T d\mathbf{q}_p = \int_{A_{plastic}} \sigma_{eq} d\epsilon_{p,eq} dA = k\sigma_y \frac{d\sigma_y}{E_p} c^{n'}$
	$d\epsilon_p = \frac{d\sigma_y}{E_p} \quad k \approx 0.2 \quad n' \approx 2$
Continuum tangent	$d\mathbf{Q} = (\mathbf{D}_e - \frac{(\frac{\partial f^T}{\partial \mathbf{Q}} \mathbf{D}_e)^T (\frac{\partial f^T}{\partial \mathbf{Q}} \mathbf{D}_e)}{\frac{\partial f^T}{\partial \mathbf{Q}} \mathbf{D}_e \frac{\partial f}{\partial \mathbf{Q}} - \frac{\partial f^T}{\partial \mathbf{Q}} \mathbf{Q} \frac{\partial f}{\partial \sigma_y} \frac{E_p}{\sigma_y k c n'}}) d\mathbf{q}$
	$d\mathbf{Q} = \begin{bmatrix} dQ_1 \\ dQ_2 \end{bmatrix} \qquad d\mathbf{q} = \begin{bmatrix} d\Delta \\ d\theta \end{bmatrix}$
Elastic J-integr.	$J_e = \frac{K_I^2}{E'} \qquad K_I = \tau_0 h^{\frac{1}{2}} [2\bar{Q}_1 g_T(\frac{a}{h}) + 6\bar{Q}_2 g_B(\frac{a}{h})]$
Plastic J-integr.	$dJ_{I,p} = m\sigma_y d\delta_{I,cracktip,p}$
CTOD vs linespr.deformation	$d\delta_{I,cracktip,p} = d\Delta_p + (\frac{t}{2} - a) d\theta_p$

Table 1: Basic relationships in line spring model

stiffness of the line-spring, with extensional and rotational degrees of freedom (Δ, θ), is derived from a plane strain edge-cracked strip loaded in tension and in bending (N, M), see Fig.1b, i.e. mode I [8]. A formulation of the Line-Spring element compatible with a two-dimensional plate or shell element with four nodes is presented in Appendix A.

The T-stress measures the constraint in the crack tip region and is used in combination with parameters such as the $J - integral$ or the $CTOD$ in order to quantify the dependence of the crack tip stress field on the geometry. The T-stress is the second term in the asymptotic expansion of the elastic solution by Williams, [9]. The T-stress has therefore been considered as an elastic parameter with a limited range of validity. Wang et al., see [10], have proposed a
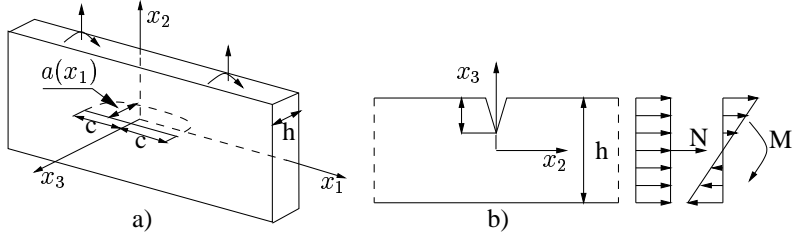
3

Figure 1: Part-trough-surface-crack and plane strain solution.

method for calculating the T-stress for the shell-line-spring-mesh based on Sham's analytical work. It is assumed that T can be written as the summation of the contributions by the membrane force, $N(s)$, and the moment, $M(s)$. Thus the T-stress at any point along the crack front can be expressed as

$$T(s) = \frac{N(s)}{h} \cdot t_N(a(s)/h) + \frac{6M(s)}{h^2} \cdot t_M(a(s)/h) \tag{1}$$

Where functions t_N and t_M are calibration factors for T in a SEN specimen with a crack depth $a(s)$ and thickness h, under unit membrane stress $\sigma^\infty(\sigma^\infty = N(s)/h)$ and unit bending stress $\sigma_b(\sigma_b = 6M(s)/h^2)$. Sham, see Parks [10], has tabulated the t_N and t_M functions for the SEN specimen. In this study the same values are used to calculate the T-stress in the $SENT$ specimen and in the pipe as previously done by Chiesa et al, see [6].

2.1.1 An accurate yield surface of plane strain single-cracked (SEC)

In a homogeneous material situation, the general yield surfaces ϕ, governing the plastic behavior of cracked shell section ligament reads:

$$\phi = \begin{cases} \phi_{df} & : & \bar{Q}_1 \geq \bar{Q}_2 \tan(\frac{\pi}{2} + \alpha) \\ \phi_{df}^s & : & \bar{Q}_1 < \bar{Q}_2 \tan(\frac{\pi}{2} + \alpha) \end{cases} \tag{2}$$

where ϕ_{df} is a parabolic yield surface with a validity confined mainly to the I and IV quadrants of the generalized force space. It reads:

$$\phi_{df} = A\bar{Q}_2 + B\bar{Q}_1 + C\bar{Q}_1^2 + D = 0 \tag{3}$$

where $A = \hat{a}_1^{df}$, $B = -\left(\hat{a}_2^{df} - \hat{b}_1^{df}\frac{a}{l}\right)(a/l)$, $C = \hat{a}_3^{df}$, $D = -\hat{a}_4^{df}(a/l)^2$. $\bar{Q}_2 = \frac{M}{\tau_0 h^2}$ and $\bar{Q}_2 = \frac{N}{2\tau_0 h}$ are the normalized generalized forces. The function ϕ_{df}^s, symmetric to ϕ_{df} with respect to the line $\overline{Q}_1 = tan(\frac{\pi}{2} + \alpha)\overline{Q}_2$, can be used in order to describe simplified (conservative) yielding behavior in the II and III quadrants. The angle α between the symmetry line and the Q_1-axis is found to be close to a linear function of the relative crack depth $\frac{a}{h}$:

$$\alpha(\frac{a}{h}) = \frac{\pi}{6}\frac{a}{h}. \tag{4}$$
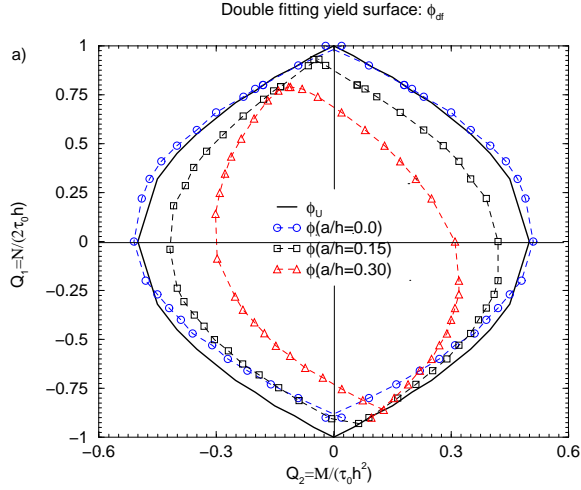
Figure 2: Double fitting yield surface

ϕ_{df}^s reads:

$$\begin{aligned}
\phi_{df}^s &= -A[\bar{Q}_2 \cos 2\alpha + \bar{Q}_1 \sin 2\alpha] \\
&\quad +B[-\bar{Q}_2 \sin 2\alpha + \bar{Q}_1 \cos 2\alpha] \\
&\quad +C[\bar{Q}_2 \sin 2\alpha - \bar{Q}_1 \cos 2\alpha]^2 + D = 0 \quad (5)
\end{aligned}$$

The ϕ is plotted in the generalized force space $Q_{1,2}$ for different crack depth to thickness ratio $\frac{a}{h}$, see Fig. 2. ϕ contains more accurate information about the general yielding behavior of shallow, as well as deep cracks, for the SEC specimen than the typically employed yield surfaces. The yield surface represented in Fig. 2, were obtained from finite element limit-load analysis, see [3].

3 Constraint corrected failure assessment

A new concept has been developed for failure assessment of low constraint applications. The conservatism of the standard failure test is reduced. The proposed procedure for establishing the dimensions of the SENT specimen to be tested is as follows:

- FE model of a cracked pipe (shell-line-spring).

- Calculation of the T-stress from an elastic analysis, by means of Parks-Sham equations.

- FE model of a SENT specimen (shell-line-springs).

- Iteration of the design parameters for the SENT specimen up to the level where the T-stress is comparable to that of the pipe

- Construction of the test specimen following from the previous point.

- Perform the test.

3.1 Geometry-dependent fracture properties

The low constraint concept for failure assessment is based on the testing of a constraint-corrected fracture mechanics specimen under tension. So far work has focused on the SENT specimen. These specimens can be fitted to give the same constraint levels as for pipe with
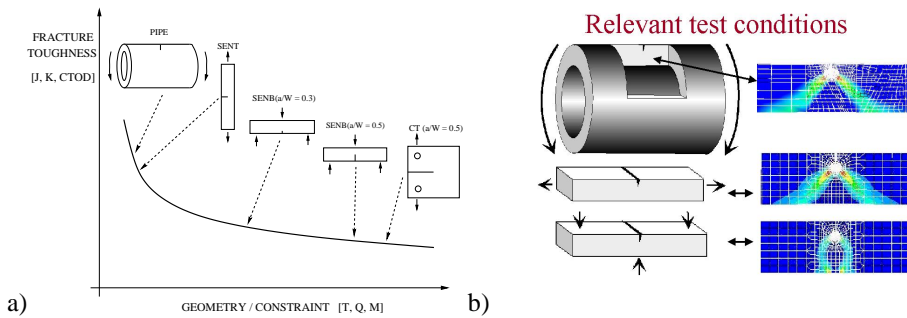
Figure 3: a) Schematic illustration of the influence of the constraint and specimen geometry on the fracture toughness. b) Ligament stress fields in high constraint SENB specimen and low constraint geometries like SENT specimens and pipes.

cracks on the surface or through the entire thickness, see Fig. 3a). The constraint level of the SENT specimen can be adjusted by varying the crack depth or the distance between the clamps. The stress fields in the low constraint geometries, such as SENT and pipes, and in the high constraint geometries, such as SENB, are different, see Fig. 3b). Similar fracture mechanisms can be expected in geometries with a comparable constraint level. If the constraint-corrected SENT specimen undergoes brittle fracture, brittle fracture after ductile crack growth, plastic collapse, or plastic collapse after ductile crack growth, the pipe will most likely suffer from the same failure mechanism. It is important to keep in mind that the fracture toughness derived from constraint-corrected specimens is limited to a specific geometry, and should not be applied to other geometries without first verifying that the constraint in the geometry is similar or higher than that of the specimen. Traditional fracture mechanic specimens give lower bound solutions for the geometries. This is one reason for the high conservatism of the traditional approaches.

3.2 Constraint correction

In [6], FE analysis of a two meter long pipe with a $230mm$ long surface notch with crack depth $a/h = 0.23$ under pure tension has been carried out using ABAQUS see [12]. The pipe wall is $h = 12.7mm$ and the outer diameter is $219mm$. In the shell-line-spring FE-model, Fig.4a) , there are 560 4-node thick shell elements and 9 line spring elements.
In the shell-line-spring FE-model of the SENT specimen, Fig. 4b), there are 48 4-node thick
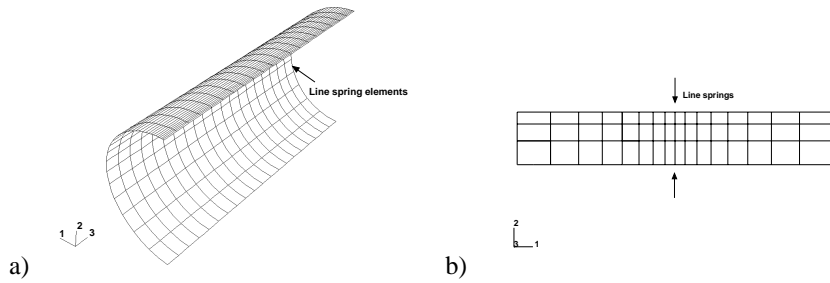
Figure 4: a) A shell-line-spring FE mesh for half of the pipe. b) A shell-line-spring FE mesh for half of the SENT specimen. The coordinates systems are local for each of the two mesh.
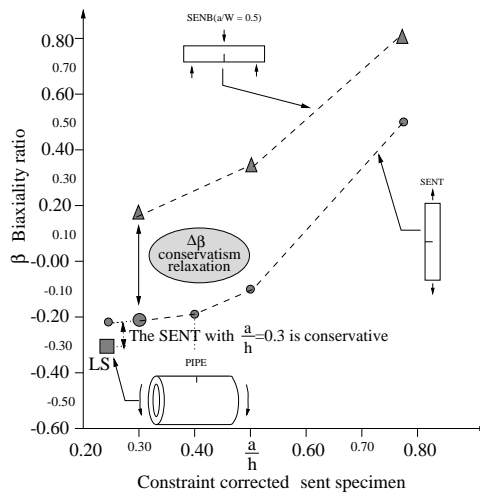
Figure 5: Constraint correction

PIPE WALL SECTION
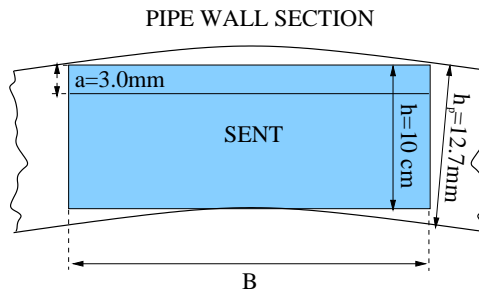
Figure 6: SENT specimen design in order to meet the constraint level of the pipe

shell elements and 3 line spring elements. Due to the symmetries only one half is modeled, with no allowance for transverse motion or rotation of the nodes along the symmetry line. The
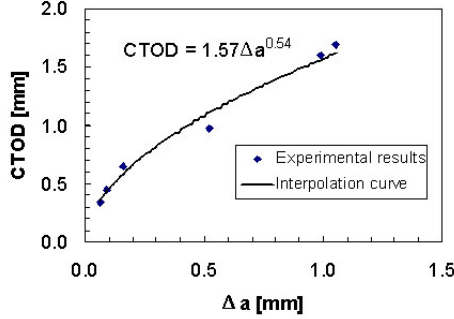
Figure 7: $CTOD - \Delta a$ curve for the constraint-corrected SENT specimen

constraint calculated from the shell-line-spring analysis by using Eq .1 gives conservative results as observed in [6]. Fig.5 presents the biaxiality factor β for different a/h relations of $SENB$ and $SENT$ specimen. β is a dimensionless parameter which relates T to the stress intensity factor K_I through Eq. 6.

$$\beta = \frac{T\sqrt{\pi a}}{K_I}. \tag{6}$$

Fig. 5 confirms what has been presented in section 3.1 (see Fig. 3): the traditional bending specimen SENB is far too conservative when a tubular geometry under tension or global bending is considered. The use of a SENT specimen with the same crack length as for the pipe relaxes the conservatism of the failure assessment, see Fig. 5. The SENT specimen can be constraint corrected until its constraint is similar to the value obtained from the shell-line-spring analysis of the pipe throughout an iterative process, see Fig 5. The constraint correction consists in finding a SENT specimen with a proper crack depth and geometry size so that its constraint is similar to that of the pipe. The crack to thickness ratio is the only parameter used here for constraint correction. The constraint corrected SENT geometry which corresponds to the pipe is the specimen with $a/h = 0.3$ and thickness $h = 10mm$ see Fig. 6. We could also have used a specimen with the same crack depth to thickness ratio as for the pipe as seen in Fig. 5. The reason for employing the proposed specimen is due to the facts that it is firstly conservative with respect to the pipe and secondly it is easy obtainable from the pipe wall..

A representative $CTOD - \Delta a$ curve for the pipe is obtained by testing the constraint-corrected SENT specimen see Fig. 7. The curve interpolating the test results reads:

$$\Delta a = (\frac{CTOD}{1.57})^{\frac{1}{0.54}} \tag{7}$$

4   Numerical implementation of the proposed yield surface

In this section some background on the implementation of the backward Euler integration scheme at the integration point of the inelastic line spring element are presented for the case of an elastic-linear-hardening material.

8

4.1 Numerical procedure for returning to the yield surface

"Frozen yield surface" with respect to relative crack depth: $\phi(\frac{a}{h})$

A return mapping algorithm provides an effective and robust integration scheme of the rate constitutive equations at the integration point of the line spring element. Geometrically, it amounts to finding the closest distance of a point to a convex set, $\phi(\frac{a}{h})$, see [15]. ϕ is considered in a first step "frozen" with respect to crack depth to thickness ratio. At a time increment Δt_n, estimate of the elastic predictor $\Delta \mathbf{q}$ is presumed known. The generalized force increment $\Delta \mathbf{Q}$, due to the elastic predictor, is obtained so that the force state at point B is calculated see Fig. 8. $\mathbf{Q}^B$ will
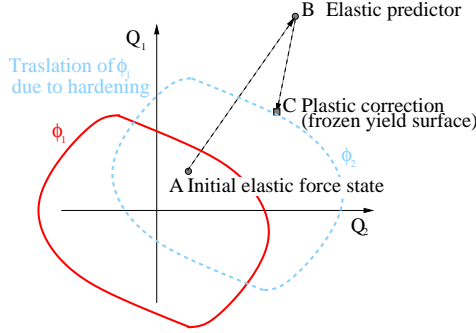
Figure 8: Representation of an elastic-predictor-plastic-corrector return algorithm for the yield surface frozen with respect to crack growth.

most likely not satisfy the yield condition $\phi = 0$, therefore, a plastic corrector $\Delta \lambda \mathbf{a}_B$ is used as first corrector, where $\mathbf{a}_B$ is the gradient to the yield surface at point B

$$\mathbf{a}_B = \frac{\partial \phi(\frac{a}{h})}{\partial \mathbf{Q}}|_B. \tag{8}$$

The generalized force estimate at point C:

$$\mathbf{Q}^C = \mathbf{Q}^B - \Delta \lambda \mathbf{D} \mathbf{a}_B \tag{9}$$

will not always lie on the yield surface, and, therefore, further iterations are required in order to find a force state which satisfies the yield criterion see Fig 8. The backward Euler return is based on the equation

$$\mathbf{Q}^C = \mathbf{Q}^B - \Delta \lambda \mathbf{D} \mathbf{a}_C \tag{10}$$

where $\mathbf{a}_C$ is the gradient to the yield surface at the final force state C. The details of the iterative loop used in order to correct $\mathbf{Q}^C$ and $\Delta \lambda$ to the right solution, can be found in [7], [15], [16] and [18].
The yield surface $\phi(\frac{a}{h})$, Eq. 2, used here, has corners located on the line $Q_1 = Q_2 \tan(\frac{\pi}{2} + a)$. There exist different solutions which can be implemented at the corners in the case when two

yield surfaces are active, see [17] and [18]. In this study, a pragmatic return to the yield surface from the corner is adopted. The "normal" at the corner is not unique, there exists a normal for the double-fitting yield surface and one for its symmetric counterpart. In order to solve this non-uniqueness problem, if we had a stress located on $\phi_{df}(\frac{a}{h}) = 0$ we consider the function $\phi_{df}(\frac{a}{h})$ to be the "master" curve so that the "normal" at the corner is calculated for this curve. The normal is now uniquely defined. When $\phi_{df}(\frac{a}{h}) = 0$, $\phi_{df}^s(\frac{a}{h})$ is checked. If this is violated further iterations are carried out. The numerical implementation is in this way kept as simple as possible.

4.2 Efficient numerical procedure for crack growth simulation.

In order to simulate ductile crack growth within the line spring framework a pragmatic procedure is chosen. The crack tip-deformation parameter $CTOD$ is computed by using the updated generalized displacement at the integration point, $\mathbf{Q_C}$. The calculated value of $CTOD$ is used
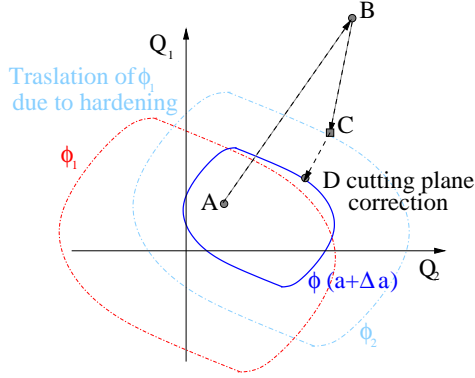
Figure 9: Representation of a cutting plane return algorithm for the yield surface updated for crack growth.

in the $CTOD - \Delta a$ curve, obtained by testing the constraint corrected SENT specimen, in order to quantify the amount of crack growth Δa. Then the yield surface is updated due to crack growth see Fig. 9. The generalized force state $\mathbf{Q_C}$ is mostly like not to lie on the updated yield surface $\phi(a + \Delta a)$. A cutting plane algorithm is here implemented in order to iterate the generalized force solution back to the updated yield surface in order to satisfy the consistency requirement, point D in Fig. 9.

4.2.1 Cutting plane algorithm for crack growth simulation.

"Updated yield surface" frozen with respect to relative crack depth: $\phi(\frac{a+\Delta a}{h})$

A cutting plane algorithm is chosen in order to obtain a generalized force state lying on the yield surface updated for crack growth. The force state at point C, $\mathbf{Q}^C$ will most likely not satisfy the yield condition $\phi(a+\Delta a) = 0$, therefore, a plastic corrector $\Delta\lambda \mathbf{Da}_C$ is used as a first correction

of the generalized force state. $\mathbf{a}_C$ is the gradient to the updated yield surface at point C

$$\mathbf{a}_C = \frac{\partial\phi(a + \Delta a)}{\partial\mathbf{Q}}|_C. \tag{11}$$

The generalized force estimate at point D:

$$\mathbf{Q}_1^D = \mathbf{Q}^C - \Delta\lambda_1\mathbf{D}\mathbf{a}_C \tag{12}$$

will not always lie on the yield surface, and, therefore, further iterations are required in order to find a force state which satisfies the yield criterion. The cutting plane algorithm is based on the equations:

$$\mathbf{Q}_{n+1}^D = \mathbf{Q}_n^D - \delta\lambda_n\mathbf{D}\mathbf{a}_{|D} \tag{13}$$

where $\delta\lambda_n$ reads

$$\delta\lambda_n = \frac{\phi(a + \Delta a)_{|D}}{\mathbf{a}_{|D}^T\mathbf{D}\mathbf{a}_{|D} + A} \tag{14}$$

where A accounts for hardening effect. Eq. 13 and 14 are repeated until $\phi(\mathbf{Q}_{n+1}^D; a + \Delta a) \leq toll$.

4.3 Observation

Ductile crack growth can also be implemented in the line-spring framework in a more formal manner since the yield surface is suitable to account for infinitesimal crack growth. The procedure chosen in the present study allows to keep the algorithm as simple as possible. Furthermore if the line spring shell simulation can account for ductile crack growth in a proper way, it may be sufficient for engineering analysis.

5 Numerical simulation

5.1 Plane strain shell-line-spring-simulation of a SENT specimen

5.1.1 Discretizations

Fig. 10 illustrates the mesh for the SENT specimen with a combination of two shell and a line spring element. The boundary conditions at the ends of the SENT specimen correspond to clamped (no rotation is allowed). The numerical results obtained from USFOS [11], where the new yielding surface is implemented, are compared to those from the ABAQUS software. Displacement in the 2-direction and rotation about the 1-direction for the nodes at the top and at the bottom of the shell-line-spring model are constrained in order to obtain a plane strain situation in the middle of the model see Fig. 10. The feasibility of the line spring implemented in the ABAQUS software is well established. Hence if the SENT specimen is to be analyzed with the USFOS software, the accuracy has to be verified.
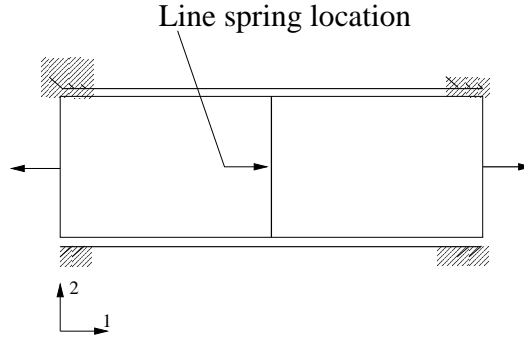
Figure 10: Shell-line-spring FE mesh. The boundary condition used are depicted.

5.1.2 Results

The shell-line-spring mesh is designed to comply with the 10mm thick constraint corrected SENT specimen. An idealized homogenous material is considered in this study along with small deformation theory. Large displacements are not compatible with the implementation of the line spring in the ABAQUS software. The line spring element implemented in USFOS can cope with large displacements. Gross Stress vs normalized displacement curves for the crack
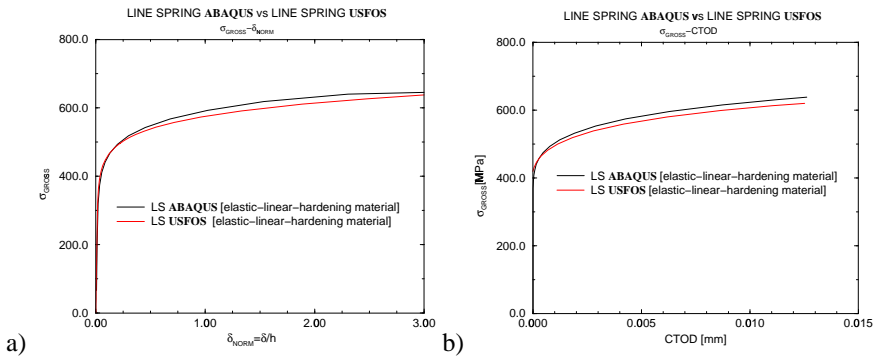
Figure 11: a) Gross stress vs normalized displacement curves obtained by ABAQUS and US-FOS b) Gross stress vs CTOD obtained by ABAQUS and USFOS

depth to thickness ratio $\frac{a}{h} = 0.3$ are plotted in Fig. 11a). The global behavior of the SENT specimen is well described by the USFOS software. The material behavior of both line-spring elements follows an elastic-linear-hardening model. The local deformation field at the crack tip is described by either the $J - integral$ or the $CTOD$ (crack tip opening displacement). There is a good agreement between the $CTOD$ values calculated from the two finite element codes as seen in Fig. 11b), where the $CTOD$ is plotted against the Gross Stress. A parametric study for different crack to thickness ratios is under progress. The two FEM codes are expected to give similar results for deep cracks while for shallow notch specimens different results are expected. This is due to the yield function implemented in the ABAQUS software for the line-spring

element, see [12]. This yield surface is intended for cracks sufficiently deep that the yielding is confined to the ligament.

In order to have a detailed study of the performance of the line spring element implementation, a local study is carried out. A generalized displacement is imposed at the nodes of the line spring:

$$
\begin{bmatrix} \nu_1 \\ \phi_1 \\ \nu_2 \\ \phi_2 \\ \nu_3 \\ \phi_3 \\ \nu_4 \\ \phi_4 \end{bmatrix} = \begin{bmatrix} \nu_1 \\ 0 \\ \nu_2 \\ 0 \\ \nu_3 \\ 0 \\ \nu_4 \\ 0 \end{bmatrix} \text{ where } \begin{cases} \nu_1 - \nu_2 = 0 \\ \nu_4 - \nu_3 = 0 \end{cases} \tag{15}
$$

A constant thickness ratio $\frac{a}{h} = 0.3$ is considered. The generalized-normalized force Q_1 is plotted against the normalized displacement ν_1 at the nodes of the line spring. The generalized force Q_2 is nearly zero for the displacement considered. Fig. 13 shows the results obtained from the
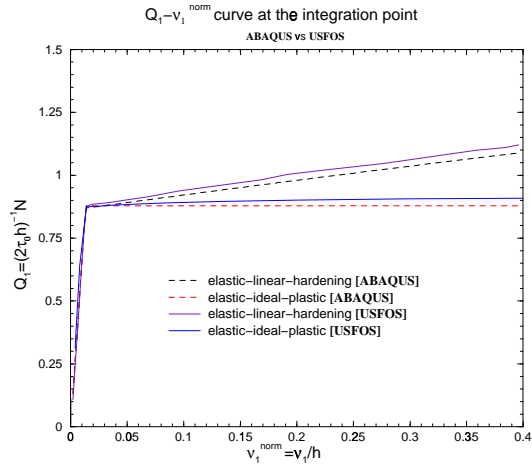
Figure 12: Generalized-normalized force vs the normalized displacement at the nodes of the line spring for two material models.

two FEM codes for the elastic ideal plastic material model and for the elastic linear hardening one. The agreement is good.

5.2 Ductile crack growth

The procedure proposed in section 4 for describing crack growth is implemented in the line spring framework as suggested previously:

- the generalized force state is determined by performing an iterative process to the yield surface considered frozen with respect of crack growth.

13

- a $CTOD$ is calculated.

- crack growth is observed when a critical value of the $CTOD$ is reached. An arbitrary value $CTOD_{cr}$ is assumed here. When $CTOD \geq CTOD_{cr}$ Eq. 7 is used to obtain the amount of crack growth.

- the yielding surface is updated due to crack growth and a further iteration procedure is carried out in order to satisfy the consistency requirement.
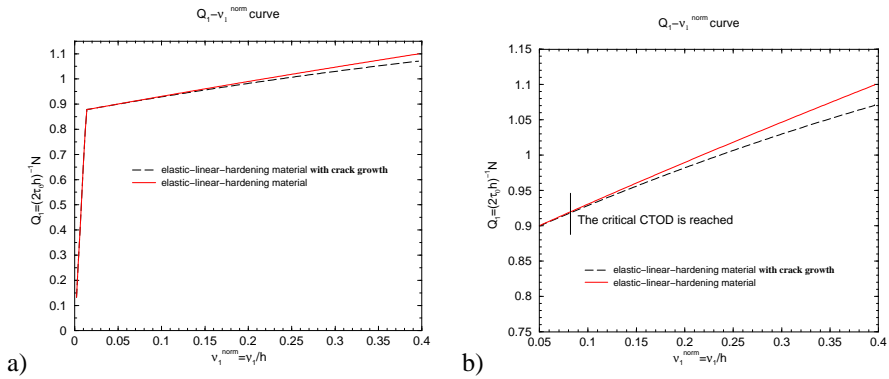
Figure 13: Generalized-normalized force vs the normalized displacement at the nodes of the line spring when crack growth is taken into account.
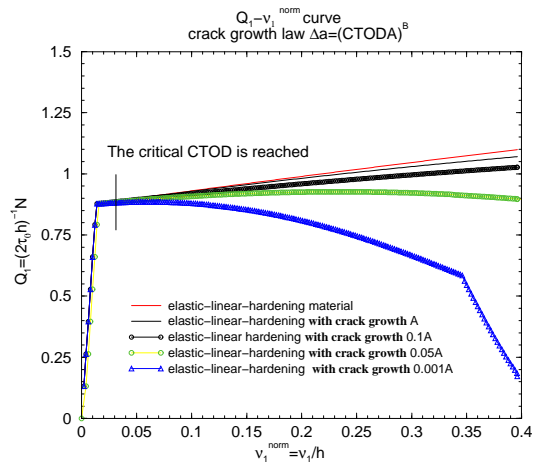
Figure 14: Generalized-normalized force vs the normalized displacement curves at the nodes of the line spring for different value of A.

Fig. 13 shows that the proposed procedure is suited to describe the combined effect of translation of the yielding surface due to hardening and the size decrease of the yielding surface due to

crack growth. Note that a small softening is observed as the net result of hardening and ductile crack growth for a bilinear material. Eq. 7 can be expressed in a more general way as:

$$\Delta a = (\frac{CTOD}{A})^{\frac{1}{B}} \tag{16}$$

For different values of A, different amount of softening is observed as expected see Fig. 14.

6 Conclusions

The improved line spring element is utilized within a new failure assessment approach. Shell line spring calculations are performed in order to calculate the constraint level of a pipe with surface or through the thickness cracks. A SENT specimen is designed to give a constraint level comparable to the one calculated for the pipe. The constraint corrected specimen is furthermore tested in order to obtain a $CTOD - \Delta a$ curve.

The $CTOD - \Delta a$ curve obtained by experimental results is implemented in the line spring framework in order to describe ductile crack growth. With the present implementation, a very efficient approach is obtained. The simulations have good accuracy. Some care is required regarding load increment sizes when ductile crack growth is included. This is due to the fact that a large increment may cause a very large contraction of the yield surface. Work is under way, using the above implementation on structural problems as pipe-laying and reeling.

A Formulation of the Line-Spring element

- The crack line, Fig 1a, is discretized into a finite number of line spring elements.

- The line spring element can be schematically represented by two straight lines $\overline{14}$ and $\overline{23}$ connected to each other by a series of springs as seen in Fig. 15. At zero deformation the lines lie upon each other. When deformation takes place each line displaces in opposite direction. The displacement is constrained by the springs.
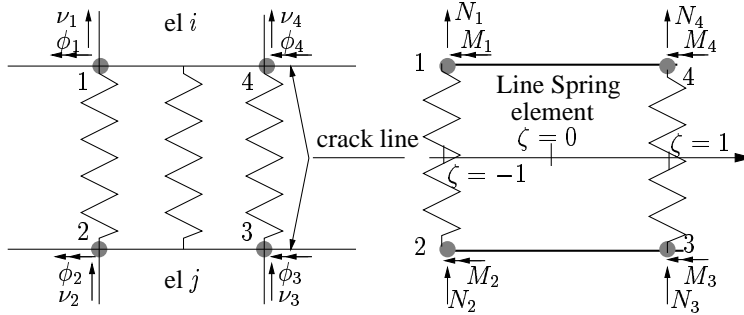
Figure 15: Line spring element.

- Let $\mathbf{q_A} = [\delta_\mathbf{A}, \theta_\mathbf{A}]^\mathbf{T}$ and $\mathbf{q_B} = [\delta_\mathbf{B}, \theta_\mathbf{B}]^\mathbf{T}$ be the generalized displacements of the line spring at $\zeta = \mp 1$ respectively. The relation between the generalized displacements and the nodal displacements (ν_i, ϕ_i) reads:

$$\delta^* = \mathbf{N}^* \nu_\mathbf{e} \tag{17}$$

$$\delta^* = \begin{bmatrix} \delta_A \\ \theta_A \\ \delta_B \\ \theta_B \end{bmatrix} \quad \mathbf{N}^* = \begin{bmatrix} 1 & 0 & -1 & 0 & 0 & 0 & 0 & 0 \\ 0 & 1 & 0 & -1 & 0 & 0 & 0 & 0 \\ 0 & 0 & 0 & 0 & -1 & 0 & 1 & 0 \\ 0 & 0 & 0 & 0 & 0 & -1 & 0 & 1 \end{bmatrix} \quad \nu_\mathbf{e} = \begin{bmatrix} \nu_1 \\ \phi_1 \\ \nu_2 \\ \phi_2 \\ \nu_3 \\ \phi_3 \\ \nu_4 \\ \phi_4 \end{bmatrix}$$

The generalized displacement $\mathbf{q} = [\delta, \theta]^T$ at an arbitrary point $|\zeta| \leq 1$ is assumed to vary linearly within the element. This reads:

$$\mathbf{q} = \mathbf{N}\delta^* \tag{18}$$

$$\mathbf{q} = \begin{bmatrix} \delta(\zeta) \\ \theta(\zeta) \end{bmatrix} \quad \mathbf{N} = \begin{bmatrix} \hat{N}_1 & 0 & \hat{N}_2 & 0 \\ 0 & \hat{N}_1 & 0 & \hat{N}_2 \end{bmatrix} \quad \delta^* = \begin{bmatrix} \delta_A \\ \theta_A \\ \delta_B \\ \theta_B \end{bmatrix}$$

16

where

$$\hat{N}_1 = \frac{1-\zeta}{2} \qquad\qquad \hat{N}_2 = \frac{1+\zeta}{2} \tag{19}$$

- The equivalent nodal forces (N_i, M_i) are calculated as follows:

$$\begin{bmatrix} N_1 \\ M_1 \\ N_4 \\ M_4 \end{bmatrix} = - \begin{bmatrix} N_2 \\ M_2 \\ N_3 \\ M_3 \end{bmatrix} = \int_{L_e} \begin{bmatrix} \hat{N}_1 & 0 \\ 0 & \hat{N}_1 \\ \hat{N}_2 & 0 \\ 0 & \hat{N}_2 \end{bmatrix} \begin{bmatrix} N \\ M \end{bmatrix} ds. \tag{20}$$

The vector $\mathbf{F}_e = [N_1, M_1, N_2, M_2, N_3, M_3, N_4, M_4]^T$ is expressed as outlined above, Eq.20, and reads:

$$\mathbf{F}_e = \int_{L_e} \begin{bmatrix} \begin{bmatrix} \mathbf{N}^T \end{bmatrix} \\ - \begin{bmatrix} \mathbf{N}^T \end{bmatrix} \end{bmatrix} \begin{bmatrix} N \\ M \end{bmatrix} ds. \tag{21}$$

- The relation between the generalized force $\mathbf{Q} = [N, M]^T$ and the corresponding generalized displacement $\mathbf{q}$ at a generic point $|\zeta| \leq 1$ reads:

$$\mathbf{Q} = \mathbf{D}\mathbf{q}. \tag{22}$$

where $\mathbf{D}$ is the stiffness matrix of the line spring at point ζ evaluated as outlined in literature [8].

- the substitution of Eq. 18 and Eq. 19 into Eq. 22 leads to:

$$\mathbf{Q} = \mathbf{D}\mathbf{N}\mathbf{N}^* \nu_{\mathrm{el}} \tag{23}$$

where the matrix multiplication $\mathbf{N}\mathbf{N}^*$ is observed to be equal to $\mathbf{N}^{**} = ([N], -[N])$. Taking into account this observation and substituting Eq. 23 into Eq. 21, we can write the stiffness equation for the line spring element as

$$\mathbf{F}_e = \int_{L_e} \mathbf{N}^{**^T} \mathbf{D}\mathbf{N}^{**} ds \nu_{\mathrm{el}} \tag{24}$$

The line spring element formulated here is compatible with a two-dimensional plate or shell element with four nodes.

References

[1] Skallerud B. and Haugen B. Collapse of thin shell structures: stress resultant plasticity modeling within a co-rotated ANDES finite element formulation. *International Journal for numerical methods in Engineering*. 46, 1961-1986, 1999.

[2] Lee H. and Parks D. M., Fully plastic analysis of plane strain single edged cracked specimen subjected to combined tension and bending. *International Journal of Fracture* 63, 329-349, 1993.

[3] **Paper III:** Chiesa M., Skallerud B. and Gross D., Closed form line spring yield surfaces for deep and shallow cracks: formulation and numerical performance. Submitted for publ. *Computers and Structures* 2000.

[4] Nyhus B., Polanco M., Ørjasæter O. High Strain Testing of Pipe Weld. *SINTEF report*. Confidential, 1999.

[5] Nyhus B. Oseberg Hyperbaric welding procedure development. Fracture mechanics testing and ECA analysis. *SINTEF report*. Unrestricted, 1998.

[6] **Paper II:** Chiesa M., Nyhus B., Skallerud B. and Thaulow C., Efficient fracture assessment of pipelines. A constrain-corrected SENT specimen approach. Engineering Fracture Mechanics 68, 527-547, 2001.

[7] Simo J. C., Taylor R. L. A return mapping algorithm for plane stress elastoplasticity. *International Journal for numerical methods in Engineering*. 22, 649-670, 1986.

[8] Rice J. R., The line spring model for surface flaws. *The Surface Crack Physical Problems and Computer Solutions*. (ed J. L. Sweldow), ASME 1972.

[9] Williams M.L., On the Stress Distribution at the Base of a Stationary Crack. *J. Applied Mech*. Vol 24, 109-114, 1957.

[10] Wang Y. Y., Parks, D. M., Evaluation of the elastic T-stress in surface crcaked plates using the line-spring method. *Int.J. Frac.*. 56, 25-40, 1992.

[11] USFOS Theory Manual. Version 7.4 *SINTEF, Trondheim Norway, 2000*

[12] Hibbit Karlson and Sorenson., ABAQUS Manual, version 5.2.

[13] White C.S., Ritchie R.O., and Parks D.M., Ductile growth of part through surface cracks: experiment and analysis. *ASTM STP 803*. (eds C.F.Shih and J.P.Gudas), ASTM 1983.

[14] Green A.P. and Hundy B. B., Initial plastic yielding in notch bend tests. *Journal of the Mechanics and Physics of Solids 16*. 1956, 128-144.

[15] Simo J. C., Taylor R. L. Consistent tangent operators for rate-independent elastoplasticity. *Computer methods in applied mechnanics and engineering*. 48, 101-118 1985.

[16] Crisfield M.A. Non-linear Finite Element Analysis of Solid and Structures *Vol 1.*

[17] Simo J. C., Kennedy J. C. and Govindee S. Non-smooth multisurface plasticity and viscoplasticity. Loading/unloading conditions and numerical algorithms. *International Journal for numerical methods in Engineering*. 26, 2161-2186 1988.

[18] Crisfield M.A. Non-linear Finite Element Analysis of Solid and Structures *Vol 2.*

An engineering methodology taking into account the effect of local damage on the global behavior of surface cracked shell structures.

Matteo Chiesa[1] Erling Østby, Bjørn Skallerud and Christian Thaulow
Department of Mechanical Engineering
Norwegian University of Technology, Trondheim, Norway

Key words: line spring, plasticity, yield surface, cracked shells, J-integral, elastic predictor, plastic corrector, crack growth.

Abstract. *The line spring finite element is a versatile numerical tool for performing engineering fracture mechanics analysis of surface cracked shells. An accurate yield surface of plane strain single-cracked (SEC) specimens having shallow, as well as deep, cracks is here presented.*
A discussion around the meaning of the $J - integral$ when crack growth occurs is carried out. The $J - integral$ is regarded as a sort of accumulated measure of the global deformation in the ligament. The complete Gurson is used in order to support our observations. Furthermore a crack propagation law relating a local criterion for crack growth to the global deformation field is outlined. A methodology to link micro-mechanically based crack growth simulations with line spring analysis is proposed by suggesting an alternative way to calculate the $J - integral$ from the line spring framework.
Some details of the numerical implementation of the backward Euler integration scheme at the integration point of the line spring element in order to account for plasticity are presented here for a bilinear material model. An efficient numerical procedure, based on

[1]Corresponding author details: R Birkelands Vei 2a N-7465 Trondheim Norway, email: Matteo.Chiesa@matek.sintef.no e–mail

a proposed crack growth law, is also presented in order to account for ductile crack propagation. A numerical case is considered in order to show that the proposed procedure is suited to the purpose.

1 Introduction

Surface cracked shell structures occur in many applications, e.g. pipelines, offshore structures, pressure vessels etc. The defects are usually introduced during the welding process. The direct discretization of the cracked shell structure with solid finite elements in order to compute the fracture mechanics quantities leads to large size problems, and makes such analysis infeasible in most cases. In order to directly calculate the fracture mechanics parameters in structural analysis, a combination of shell [1] and line spring finite elements [2], [3] instead of solid finite elements is an attractive option. The line spring element can be schematically represented by two straight lines $\overline{14}$ and $\overline{23}$ connected to each other by a series of springs as seen in Fig. 1. At zero deformation the lines lie upon each other. When deformation takes place each line displaces in opposite direction. The displacement is constrained by the springs. The stiffness of the line spring is derived from a plane strain SEC (single edged cracked) specimen under tension and bending. The general yield surfaces ϕ see [3], governing the plastic behavior of cracked shell section ligament, is plotted in the generalized force space $Q_{1,2}$ for different crack depth to thickness ratio $\frac{a}{h}$, Fig. 3. ϕ contains more accurate information about the general yielding behavior of shallow, as well as deep cracks, for the SEC specimen than the typically employed yield surfaces.

The materials commonly used for offshore pipelines are normally very tough and ductile. Under such circumstances, the initiation of the crack growth is often preceded by fully plastic yielding of the un-cracked ligament section and some amount of ductile crack growth can often be tolerated before fracture instability occurs. Ductile crack extension is a consequence of large plastic flow causing voids to grow and coalesce, therefore a reliable description of the fully developed yielding field in the rest ligament, see [3], is important for a further development of the line-spring element in order to account for crack growth. The $J - integral$ is generally considered to properly describe the strain-dominated fracture process, because it can connect the local micro-mechanism of crack extension to geometry dependent stress and plastic flow.

A discussion around the meaning of the $J - integral$ when crack growth occurs is here presented. The $J - integral$ does not reflect directly the condition at the crack tip, it should be regarded as some accumulated measure of the global deformation in the ligament. The global deformation is dependent on stress triaxiality and damage accumulation ahead of

2

the growing crack. Damage accumulation ahead of the growing crack is due to void nucle-ation, growth and coalescence. Void nucleation and growth is described by a dilatational plasticity model introduced by Gurson and later modified by Tvergaard and Needleman [4]. The Gurson model can describe the softening behavior due to the nucleation and growth of voids, but has no intrinsic ability to predict the shift from the homogeneous deformation mode to a localized mode due to void coalescence. In the complete Gurson model, Zhang uses Thomason's plastic limit load model as a coalescence criterion for the Gurson model [5]. Zhang modifies Thomason's theory by assuming that the voids are always spherical. This modification makes the plastic limit load model fully compatible with the Gurson model see Appendix A.

In this study the complete Gurson model is utilized in order to relate a local criterion for crack growth to the global deformation field. Analytical expression for the full velocity field in case of ductile crack growth is very difficult to derive, and therefore simplified approaches must be sought. The normalized $J - \Delta a$ curves obtained for two different geometries happen to collapse onto each other for different initial void volume fraction f_0. This suggests that the shape of the crack growth resistance curve is mainly decided by the specimen geometry, and can be modified by a constant factor to take the ductility of the material into account.

An efficient numerical procedure, based on a proposed crack growth law, is presented in order to account for ductile crack growth in the line spring framework. In order to sim-ulate inelastic behavior and ductile crack growth within the line spring framework, the generalized force state accounting for plasticity is updated considering the yield surface size "frozen" with respect to crack depth to thickness ratio ($\frac{a}{h} = const$). Then the defor-mation parameter J, is computed by using the updated generalized displacement state at the integration point. The calculated value of J is used in the $J - \Delta a$ curve, developed here, in order to quantify the amount of crack growth Δa. Then the yield surface is up-dated due to crack growth, and a cutting plane algorithm is used to iterate the generalized force solution previously obtained back to the new yield surface in order to satisfy the consistency requirement. The details of the implementation of the backward Euler inte-gration scheme at the integration point of the line spring element in order to account for plasticity and crack growth are presented here for a bilinear material model, see [3], [6].

2 Theoretical background

2.1 Surface cracked shell

The part-through surface crack is originally a three dimensional problem as seen in Fig. 2a. Here $a(x_1)$ is the crack depth at x_1. The three dimensional problem is formulated within the context of two-dimensional plate or shell theory with the part-cracked section represented as a line-spring.
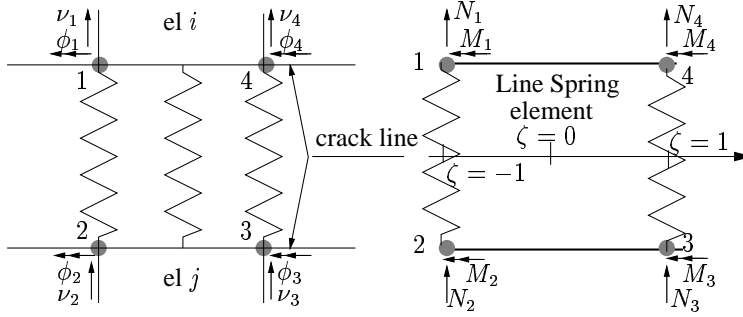
Figure 1: Line spring element.
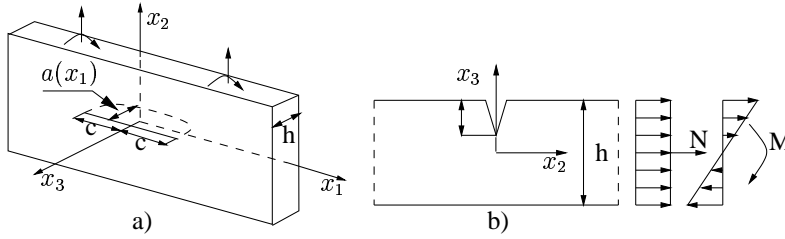
Figure 2: Part-trough-surface-crack and plane strain solution.

The line-springs take into account the additional flexibility due to the surface crack. The stiffness of the line-spring, with extensional and rotational degrees of freedom (Δ, θ), is derived from a plane strain edge-cracked strip loaded in tension and in bending (N, M), see Fig.2b, i.e. mode I. A formulation of the Line-Spring element compatible with a two-dimensional plate or shell element with four nodes is presented in [3].

4

Yield surface	$\phi(\bar{Q}_1, \bar{Q}_2, \sigma_y; c) = \begin{cases} \phi_{df} & : & \bar{Q}_1 \geq \bar{Q}_2 \tan(\frac{\pi}{2} + \alpha) \\ \phi_{df}^s & : & \bar{Q}_1 < \bar{Q}_2 \tan(\frac{\pi}{2} + \alpha) \end{cases}$
	$Q_1 = N \quad Q_2 = M$
	$\bar{Q}_1 = \frac{N}{2\tau_0 h} \quad \bar{Q}_2 = \frac{M}{\tau_0 h^2} \quad c = h - a$
Work hardening	$dW_p = \mathbf{Q}^T d\mathbf{q}_p = \int_{A_{plastic}} \sigma_{eq} d\epsilon_{p,eq} dA = k\sigma_y \frac{d\sigma_y}{E_p} c^{n'}$
	$d\epsilon_p = \frac{d\sigma_y}{E_p} \quad k \approx 0.2 \quad n' \approx 2$
Continuum tangent	$d\mathbf{Q} = (\mathbf{D}_e - \frac{(\frac{\partial f^T}{\partial \mathbf{Q}} \mathbf{D}_e)^T (\frac{\partial f^T}{\partial \mathbf{Q}} \mathbf{D}_e)}{\frac{\partial f^T}{\partial \mathbf{Q}} \mathbf{D}_e \frac{\partial f}{\partial \mathbf{Q}} - \frac{\partial f^T}{\partial \mathbf{Q}} \mathbf{Q} \frac{\partial f}{\partial \sigma_y} \frac{E_p}{\sigma_y k c^{n'}}}) d\mathbf{q}$
	$d\mathbf{Q} = \begin{bmatrix} dQ_1 \\ dQ_2 \end{bmatrix} \qquad d\mathbf{q} = \begin{bmatrix} d\Delta \\ d\theta \end{bmatrix}$
Elastic J-integr.	$J_e = \frac{K_I^2}{E'} \qquad K_I = \tau_0 h^{\frac{1}{2}} [2\bar{Q}_1 g_T(\frac{a}{h}) + 6\bar{Q}_2 g_B(\frac{a}{h})]$
Plastic J-integr.	$dJ_{I,p} = m\sigma_y d\delta_{I,cracktip,p}$
CTOD vs linespr.deformation	$d\delta_{I,cracktip,p} = d\Delta_p + (\frac{t}{2} - a) d\theta_p$

Table 1: Basic relationships in line spring model

2.1.1 An accurate yield surface of plane strain single-cracked (SEC)

For a homogeneous material, the general yield surfaces ϕ, governing the plastic behavior of cracked shell section ligament reads:

$$\phi = \begin{cases} \phi_{df} & : & \bar{Q}_1 \geq \bar{Q}_2 \tan(\frac{\pi}{2} + \alpha) \\ \phi_{df}^s & : & \bar{Q}_1 < \bar{Q}_2 \tan(\frac{\pi}{2} + \alpha) \end{cases} \tag{1}$$

where ϕ_{df} is a parabolic yield surface with a validity confined mainly to the I and IV quadrants of the generalized force space. It reads:

$$\phi_{df} = A\bar{Q}_2 + B\bar{Q}_1 + C\bar{Q}_1^2 + D = 0 \tag{2}$$

5

see [3] for the fitting parameters A, B, C, D. The function ϕ_{df}^s, symmetric to ϕ_{df} with respect to the line $\overline{Q}_1 = tan(\frac{\pi}{2} + \alpha)\overline{Q}_2$, can be used in order to describe simplified (conservative) yielding behavior in the II and III quadrants. The angle α between the
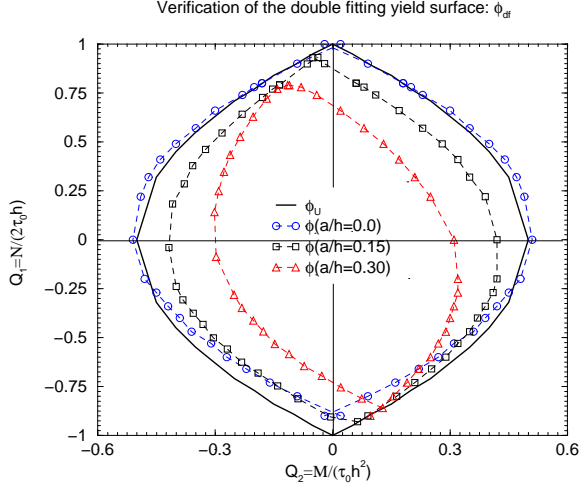
Figure 3: Double fitting yield surface

symmetry line and the Q_1-axis is found to be close to a linear function of the relative crack depth $\frac{a}{h}$. The ϕ is plotted in the generalized force space $Q_{1,2}$ for different crack depth to thickness ratio $\frac{a}{h}$, see Fig. 3. ϕ contains more accurate information about the general yielding behavior of shallow, as well as deep cracks, for the SEC specimen than the typically employed yield surfaces. The fitted yield surfaces represented in Fig. 3, were obtained from finite element the limit-load analysis by Lee and Parks [2], see [3].

3   Fracture mechanics parameters

For very brittle materials, exhibiting no or little plasticity, the critical stress intensity, K_{IC}, or the critical energy release rate, G_{IC}, expresses the fracture toughness of the material. For elasto-plastic materials, Rice [8] introduced the J-integral as a fracture mechanics parameter. The J-integral, for a crack assumed to propagate in the x_1-direction, is evaluated as a line integral from the following expression:

$$J = \oint W\,dy - T_i \frac{\partial u_i}{\partial x_1} ds \qquad (3)$$

6

where W is the stain energy density, T_i are the tractions, u_i the displacements on the path, s, over which the line integral is evaluated. In Rice's original derivation of the J-integral it was actually assumed that the material behaved as a non-linear elastic material. If proportional loading is assumed a special feature of the J-integral is that its value is independent of the path around the crack tip on which it is evaluated. In case of proportional loading the results will be equally valid for materials obeying J_2 deformation theory. Further, under the assumption of non-linear elastic material the J-integral will be identical to the energy release rate, G. Hutchinson [9] and Rice and Rosengren [10] also showed, using a non-linear eigenvalue expansion, that the J-integral would scale the stresses and strains close to the crack tip in the leading asymptotic term of the expansion. In case of a more realistic J_2 flow theory, and taking finite deformation effects at the crack tip into account, unloading will happen in this region, and the path independence of the J-integral is lost. However, if the zone of finite deformation is contained within a region still controlled be the asymptotic behavior the J-integral will uniquely characterize the conditions at the crack tip. Recent studies on the effect of specimen geometry, or constraint level, has revealed that such situations rarely exists in finite specimen geometries, and a single parameter description of the near tip stress level is not possible. However the J-integral will still reflect the size over which high stresses/strains develop in the material, and is thus still a useful fracture mechanics parameter.

a)
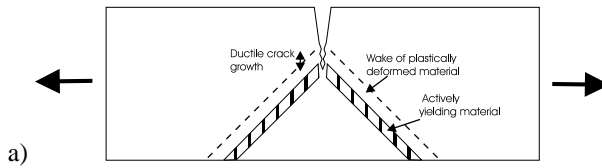
In the case of ductile crack growth the J-integral is also used to express the materials resistance to such crack growth through the $J - \Delta a$ curve, where Δa is the amount of ductile crack growth. In the crack tip region significant non-proportional loading will occur, and strong path dependence for the J-integral is found. However, if the J-integral is evaluated on contours far form the crack tip a more or less path independent behavior is observed. The reason for this can principally be seen from the following argumentation. When the crack grows, the ligament size will change. This will cause the most intense plastic deformation here to translate with the crack growth, leaving a wake of plastically deformed material, as schematically shown for a specimen loaded in tension and bending, respectively, in Fig. 4.

Far from the crack tip the ductile crack growth will have very little influence on the remote
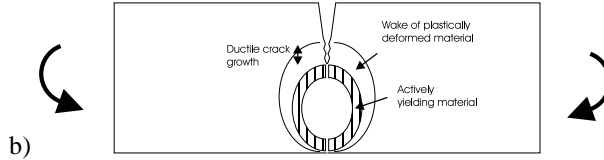
Figure 4: Moving plastic deformation field for a) a specimen loaded in tension and b) in bending

plastic deformation pattern. The J value evaluated according to Eq. 3 will now primarily be controlled by the contribution from the first term, which contains the accumulated value of the moving intense plastic deformation field. When calculated in an area where the flow pattern is not significantly altered by the crack growth, the calculated J-integral is almost independent on the integration path. It is however important to realize that this J-value, often referred to as the far-field J, does not reflect directly the conditions at the crack tip, and should in stead be regarded as some accumulated measure of the global deformation in the ligament. This interpretation will be important to keep in mind in the following.

4   Micro-mechanical damage mechanics

In contrast to the continuum damage model where the damage is treated by thermodynamics, constitutive relations can also be directly obtained from *micro-mechanical* based models. If we limited our analysis to polycrystalline metals where ductile fracture occurs by nucleation, growth and coalescence of micro-voids one of the best micro-mechanically defined models is the so called *Complete Gurson model* see Appendix A. The *Complete Gurson model* describes:

- the decreasing load carrying capacity due to void nucleation and growth by a dilatational plasticity model introduced by Gurson and modified by Tvergaard and Nedleman in a later stage [11], [12];

- the shift from a homogeneous deformation mode to a localized mode by void coalescence due to a plastic limit load model introduced by Thomason [13] [14]

In conclusion, the *Complete Gurson model* integrates both the dilatational plasticity model due to Gurson and the plastic limit load model due to Thomason. The main features of both the dilatational plasticity model and the plastic limit load model which are the fundamentals of the *Complete Gurson model* are presented in details in Appendix A

4.1 Simulation of ductile crack growth

The ductile crack growth behavior is studied for two different geometries. The first one is a shallow cracked, $\frac{a}{W} = 0.15$, specimen loaded in tension, and the second geometry is a deep cracked, $\frac{a}{W} = 0.5$, specimen loaded in bending. The two specimen geometries, with relevant dimensions, are shown in Fig. 5.

Plane strain FE analysis of the two geometries are performed using ABAQUS. Four node
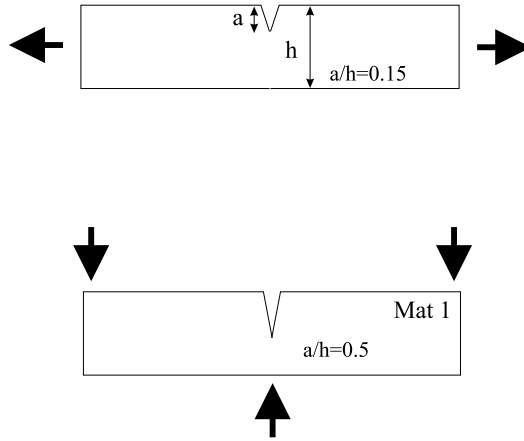
Figure 5: Two specimen geometries, with relevant dimensions.

first order elements (ABAQUS type CPE4) are applied, and large deformation effects are accounted for in the analysis. The relation between plastic strain and the flow stress used for the matrix material is on the form:

$$\bar{\sigma} = \sigma_0 \left(1 + \frac{\varepsilon_P}{\varepsilon_0} \right)^n \tag{4}$$

where $\bar{\sigma}$ is the flow stress, σ_0 is the yield stress, ε_P is the equivalent plastic strain, $\varepsilon_0 = \sigma_0/E$ is the strain at yield, and n is the hardening exponent. A fixed ratio of $E/\sigma_0 = 500$, with $\sigma_0 = 400 MPa$, and $n = 0.1$ is used. Further, three different levels of initial void volume fraction, $f_0 = 0.0005, 0.002$, and 0.005, are used to assess the

effect of varying ductility of the material. One should note that the lowest f_0 value is representative for a base material steel while the other two are typical for the weld material.

Figure 6: $J - \Delta a$ curves for the tensile specimen when three different levels of initial void volume fraction are considered.

The resulting $J - \Delta a$ curves from the numerical analysis are shown in Fig. 6 and 7. From Fig. 6, showing the results for the tensile specimen, it can be seen that the assumed initial void volume fraction has a signif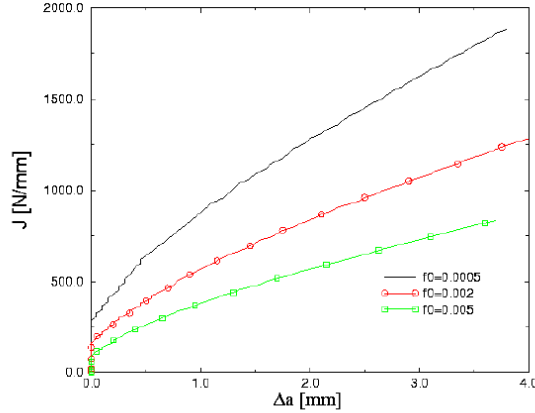icant effect on the crack growth resistance, both with regard to initiation and slope of the resistance curve, expressed through the J-integral. Further, it can be seen that the curves exhibit a somewhat steeper slope for small amounts of crack growth, after which an almost linear relation between J and Δa exist. The results for the bend specimen are shown in Fig. 7. By comparison with the results for the tensile curve it can be seen that the crack growth resistance is lower, as expected due to the higher geometry constraint in this specimen. However, qualitatively they show much the same behavior as the tensile specimen, with still a significant effect of the initial void volume fraction on the crack growth resistance.

A qualitative explanation for the higher crack growth resistance for lower f_0 is due to the higher deformation needed at the crack tip to cause void coalescence. This will be naturally reflected in a higher J, because a higher incremental deformation in the remaining ligament is needed in order to "feed" deformation into the crack tip to sustain ductile
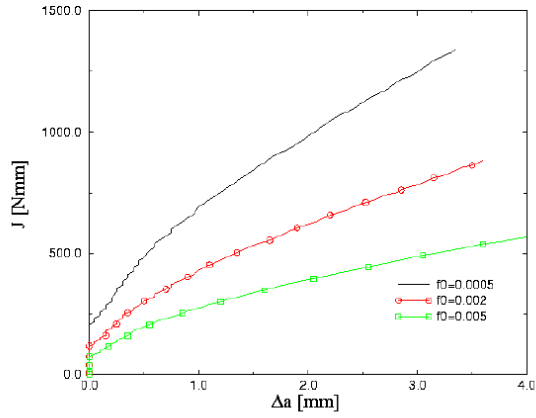
10

Figure 7: $J - \Delta a$ curves for the bend specimen when three different levels of initial void volume fraction are considered.
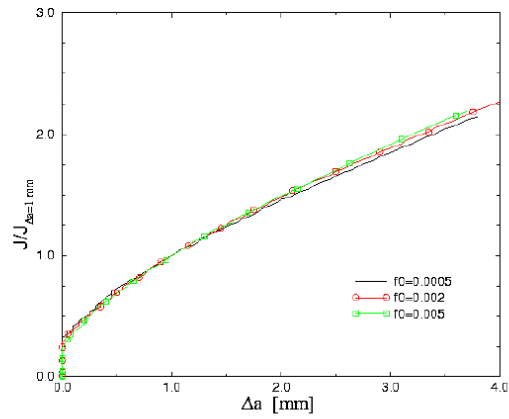
a)
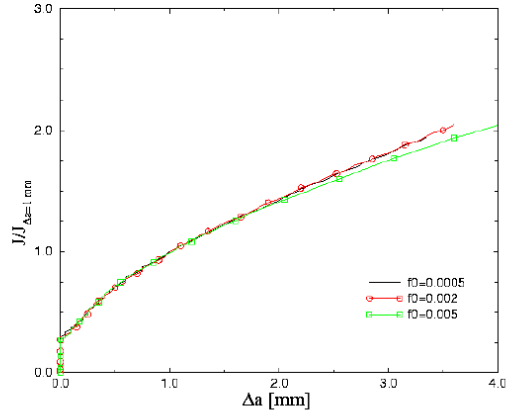
b)

Figure 8: Normalized $J - \Delta a$ curves for a) the tensile and b) the bending specimen.

crack growth. One of the challenges in simulating ductile crack growth is to relate the local criterion for crack growth to the global deformation field. Analytical expression for the full velocity field in case of ductile crack growth is very difficult to derive even in the case of elastic- ideally plastic material behavior, and simplified approaches must be sought. Here we point out one such possible way. In Fig. 8 we have replotted the $J - \Delta a$ curves, with the J-value now "normalized" by the J value at 1 mm of crack growth. A striking feature of these curves is that these normalized curves almost completely collapse onto each other for different f_0, both for the tensile and bend specimens. This points in the direction that the shape of the crack growth resistance curve is in principle given by the specimen geometry, and can be modified by a constant factor to take the ductility of the material into account. However, we point out that the normalization is not perfect. Further, the choice of using the J value at $1mm$ of crack growth is also somewhat arbitrary. Despite this, use of such an approximate relation may open for efficient use of crack growth simulations in engineering analysis, taking the effect of material properties with sufficient accuracy into account. Such an approach is outlined below.

12

5   Methodology to link micro-mechanically based crack growth simulations with line spring analysis

The contribution to the J-integral can be split into an elastic and a plastic part:

$$J = J_{el} + J_{pl} \tag{5}$$

For fully plastic condition, which is the relevant situation for crack growth analysis, J_{el} remains virtually constant with crack growth. Further, the elastic part of the J-integral will be significantly smaller than the plastic part. A common way to approximate the plastic part of the J-integral is found from the expression:

$$J_{ep} = \frac{\eta}{ch} \int P d\Delta_p \tag{6}$$

where η is a geometry factor depending on mode of loading, relative crack depth, and to some extent material parameters, c is the ligament, h is the specimen thickness, and the integral is the plastic work in the deformation zone in the ligament, with P as a global load and Δ_p the corresponding plastic part of the displacement. The plastic work can be obtained directly by integrating the plastic work in the line spring element. The incremental increase in the J-integral can be found by differentiating Eq. 6 with respect to Δ_p. What is further needed is a crack growth law to relate the increment in crack growth, $d\Delta a$, to dJ_{pl}. Two alternative approaches may be proposed here. The first approach is based on fitting the $J - \Delta a$ curve to a power law representation, leading to the following incremental crack growth law:

$$\frac{d\Delta a}{dJ_{pl}} = C_1 C_2 J_{pl}^{C_1 - 1} \tag{7}$$

where C_1 is a constant depending on the material properties, and C_2 depends on the specimen geometry/mode of loading. C_1 and C_2 could be determined from systematic damage mechanics analysis of crack growth as presented above. A more simplified way could be to assume a linear relation between Δa and J_{pl}, which would lead to the incremental crack growth law:

$$\frac{d\Delta a}{dJ_{pl}} = C_3 \tag{8}$$

where C_3 depends on both material properties and specimen geometry/mode of loading. The constant C_3 could be fitted to the almost linear part of the $J - \Delta a$ curve, seen for larger amounts of crack growth in Fig. 8a) and b) . Such an approach would be slightly

13

conservative in that the initially higher resistance to crack growth is disregarded. Once a crack growth law is established, a fully coupled scheme to update the yield surface in the line spring, using J_{pl} and Δa, can be derived.

5.1 Crack propagation law

A representative $J - \Delta a$ curve for the tensile specimen is found by fitting the normalized curve for $f_0 = 0.005$ plotted in Fig 8a) with a power law as previously proposed. The fitting power law reads:

$$J = D_1 \Delta a^{D_2} + D_3 \tag{9}$$

where $D_1 = 0.71$, $D_2 = 0.72$ and $D_3 = 0.28$. The value of the $J-integral$ at $\Delta a = 1mm$ is $J_{\Delta a=1mm} = 880\frac{N}{mm}$. Eq. 9 is compared to the $J - \Delta a$ for different f_0 in Fig. 9. The fitting is satisfactory from an engineering point of view.
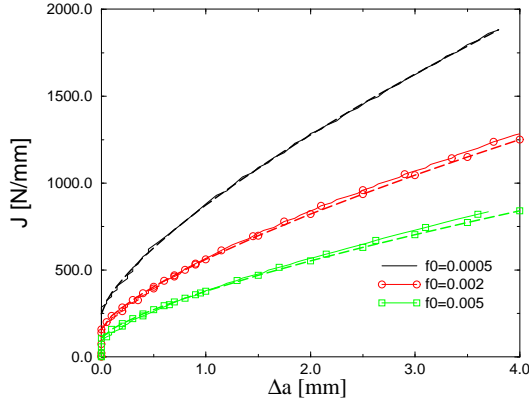

Figure 9: The fitting equation is compared to the $J - \Delta a$ curve obtained from numerical analysis

6 Numerical implementation of the crack propagation law in the line spring framework

In this section some background on the implementation of the backward Euler integration scheme at the integration point of the inelastic line spring element is presented for the

case of an elastic-linear-hardening material.

A return mapping algorithm provides an effective and robust integration scheme of the rate constitutive equations at the integration point of the line spring element. Geometrically, it amounts to finding the closest distance of a point to a convex set, $\phi(\frac{a}{h})$, see [24]. ϕ is considered in a first step "frozen" with respect to crack depth to thickness ratio. At a time increment Δt_n, estimate of the elastic predictor $\Delta \mathbf{q}$ is presumed known. The generalized force increment $\Delta \mathbf{Q}$, due to the elastic predictor, is obtained so that the force state at point B is calculated see Fig. 10. $\mathbf{Q}^B$ will most likely not satisfy the yield condi-
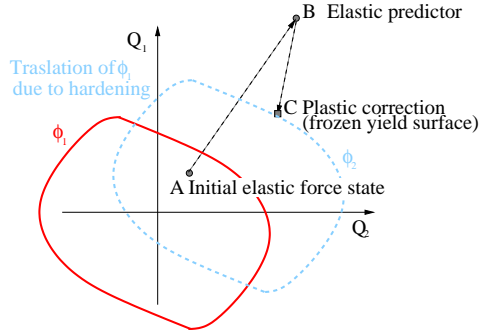
Figure 10: Representation of an elastic-predictor-plastic-corrector return algorithm for the yield surface frozen with respect to crack growth.

tion $\phi = 0$, therefore, a plastic corrector $\Delta \lambda \mathbf{a}_B$ is used as first corrector, where $\mathbf{a}_B$ is the gradient to the yield surface at point B

$$\mathbf{a}_B = \frac{\partial \phi(\frac{a}{h})}{\partial \mathbf{Q}}|_B. \tag{10}$$

The generalized force estimate at point C:

$$\mathbf{Q}^C = \mathbf{Q}^B - \Delta \lambda \mathbf{D} \mathbf{a}_B \tag{11}$$

will not always lie on the yield surface, and, therefore, further iterations are required in order to find a force state which satisfies the yield criterion see Fig 10. The backward Euler return is based on the equation

$$\mathbf{Q}^C = \mathbf{Q}^B - \Delta \lambda \mathbf{D} \mathbf{a}_C \tag{12}$$

where $\mathbf{a}_C$ is the gradient to the yield surface at the final force state C. The details of the iterative loop used in order to correct $\mathbf{Q}^C$ and $\Delta \lambda$ to the right solution, can be found in

15

[16], [24], [25] and [27].

The yield surface $\phi(\frac{a}{h})$, Eq. 1, used here, has corners located on the line $Q_1 = Q_2 \tan(\frac{\pi}{2} + a)$. There exist different solutions which can be implemented at the corners in the case when two yield surfaces are active, see [26] and [27]. In this study, a pragmatic return to the yield surface from the corner is adopted. The "normal" at the corner is not unique, there exists a normal for the double-fitting yield surface and one for its symmetric counterpart. In order to solve this non-uniqueness problem, if we had a stress located on $\phi_{df}(\frac{a}{h}) = 0$ we consider the function $\phi_{df}(\frac{a}{h})$ to be the "master" curve so that the "normal" at the corner is calculated for this curve. The normal is now uniquely defined. When $\phi_{df}(\frac{a}{h}) = 0$, $\phi_{df}^s(\frac{a}{h})$ is checked. If this is violated further iterations are carried out. The numerical implementation is in this way kept as simple as possible.

In order to simulate ductile crack growth within the line spring framework a pragmatic procedure is chosen. The $J - integral$ is computed by using the updated generalized displacement at the integration point, $\mathbf{Q_C}$. The calculated value of J is used in the $J - \Delta a$
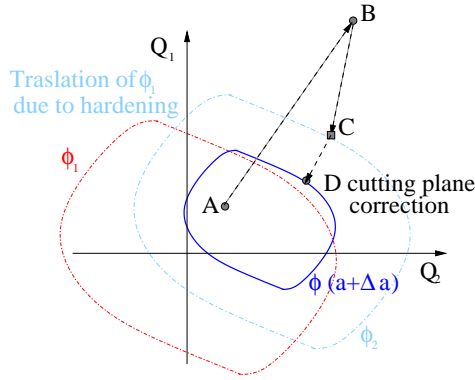
Figure 11: Representation of a cutting plane return algorithm for the yield surface updated for crack growth.

curve, obtained by testing or numerical damage studies in order to quantify the amount of crack growth Δa. Then the yield surface is updated due to crack growth see Fig. 11. The generalized force state $\mathbf{Q_C}$ is most likely not to lie on the updated yield surface $\phi(a+\Delta a)$. A cutting plane algorithm is here implemented in order to iterate the generalized force solution back to the updated yield surface in order to satisfy the consistency requirement, point D in Fig. 11.

A plastic corrector $\Delta\lambda \mathbf{Da}_C$ is used as a first correction of the generalized force state. $\mathbf{a}_C$

is the gradient to the updated yield surface at point C

$$\mathbf{a}_C = \frac{\partial \phi(a + \Delta a)}{\partial \mathbf{Q}}|_C. \tag{13}$$

The generalized force estimate at point D:

$$\mathbf{Q}_1^D = \mathbf{Q}^C - \Delta \lambda_1 \mathbf{D} \mathbf{a}_C \tag{14}$$

will not always lie on the yield surface, and, therefore, further iterations are required in order to find a force state which satisfies the yield criterion. The cutting plane algorithm is based on the equations:

$$\mathbf{Q}_{n+1}^D = \mathbf{Q}_n^D - \delta \lambda_n \mathbf{D} \mathbf{a}_{|D} \tag{15}$$

where $\delta \lambda_n$ reads

$$\delta \lambda_n = \frac{\phi(a + \Delta a)_{|D}}{\mathbf{a}_{|D}^T \mathbf{D} \mathbf{a}_{|D} + A} \tag{16}$$

where A accounts for hardening effect. Eq. 15 and 16 are repeated until $\phi(\mathbf{Q}_{n+1}^D; a + \Delta a) \leq toll$.

7 Numerical simulation

7.1 Plane strain shell-line-spring-simulation of a SENT specimen

7.1.1 Discretization

Fig. 12 illustrates the mesh for the SENT specimen with a combination of two shell and a line spring element. The boundary conditions at the ends of the SENT specimen correspond to clamped (no rotation is allowed). The numerical results obtained from USFOS [19], where the new line spring yielding surface is implemented, are compared to those from the ABAQUS software. Displacement in the 2-direction and rotation about the 1-direction for the nodes at the top and at the bottom of the shell-line-spring model are constrained in order to obtain a plane strain situation in the middle of the model see Fig. 12. The feasibility of the line spring implemented in the ABAQUS software is well established. Hence if the SENT specimen is to be analyzed with the USFOS software, the accuracy has to be verified.
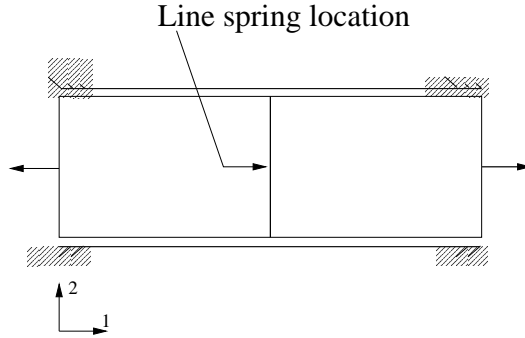
Figure 12: Shell-line-spring FE mesh. The boundary condition used are depicted.

7.1.2 Results

The shell-line-spring mesh is designed to comply with the 10mm thick constraint corrected SENT specimen. An idealized homogenous material is considered in this study along with small deformation theory. Large displacements are not compatible with the implementation of the line spring in the ABAQUS software. The line spring element implemented in USFOS accounts for large displacements, [20]. Gross Stress vs normalized
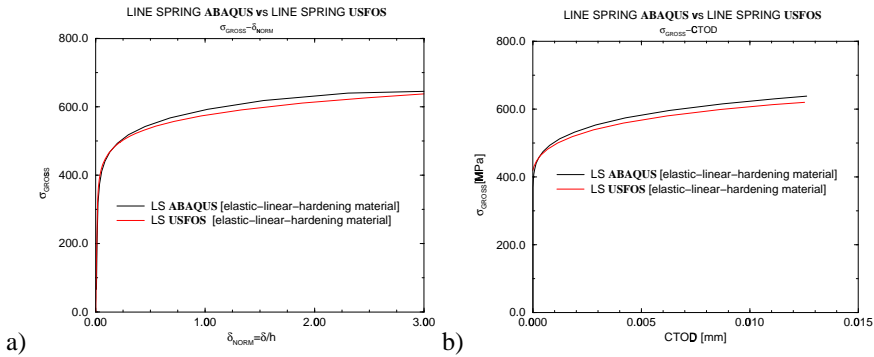
Figure 13: a) Gross stress vs normalized displacement curves obtained by ABAQUS and USFOS b) Gross stress vs CTOD obtained by ABAQUS and USFOS

displacement curves for the crack depth to thickness ratio $\frac{a}{h} = 0.3$ are plotted in Fig. 13a). The global behavior of the SENT specimen is well described by the USFOS software. The material behavior of both line-spring elements follows an elastic-linear-hardening model.

There is a good agreement between the $CTOD$ values calculated from the two finite element codes as seen in Fig. 13b), where the $CTOD$ is plotted against the Gross Stress. A parametric study for different crack to thickness ratios is under progress. The two FEM codes are expected to give similar results for deep cracks while for shallow notch specimens different results are expected. This is due to the yield function implemented in the ABAQUS software for the line-spring element, see [21]. This yield surface is intended for cracks sufficiently deep that the yielding is confined to the ligament.

In order to have a detailed study of the performance of the line spring element implementation, a local study is carried out. A generalized displacement is imposed at the nodes of the line spring:

$$\begin{bmatrix} \nu_1 \\ \phi_1 \\ \nu_2 \\ \phi_2 \\ \nu_3 \\ \phi_3 \\ \nu_4 \\ \phi_4 \end{bmatrix} = \begin{bmatrix} \nu_1 \\ 0 \\ \nu_2 \\ 0 \\ \nu_3 \\ 0 \\ \nu_4 \\ 0 \end{bmatrix} \text{ where } \begin{cases} \nu_1 - \nu_2 = 0 \\ \nu_4 - \nu_3 = 0 \end{cases} \tag{17}$$

A constant thickness ratio $\frac{a}{h} = 0.3$ is considered. The generalized-normalized force Q_1 is plotted against the normalized displacement ν_1 at the nodes of the line spring. The generalized force Q_2 is nearly zero for the displacement considered. Fig. 14 shows the results obtained from the two FEM codes for the elastic ideal plastic material model and for the elastic linear hardening one. The agreement is good.

7.2   Ductile crack growth

The procedure proposed in section 6 for describing crack growth is implemented in the line spring framework as suggested previously:

- the generalized force state is determined by performing an iterative process to the yield surface considered frozen with respect of crack growth.

- a $J - integral$ is calculated.

- crack growth is observed when a critical value of the $J - integral$ is reached. An arbitrary value J_{cr} is assumed here. When $J \geq J_{cr}$ Eq. 9 is used to obtain the amount of ductile crack growth increment.
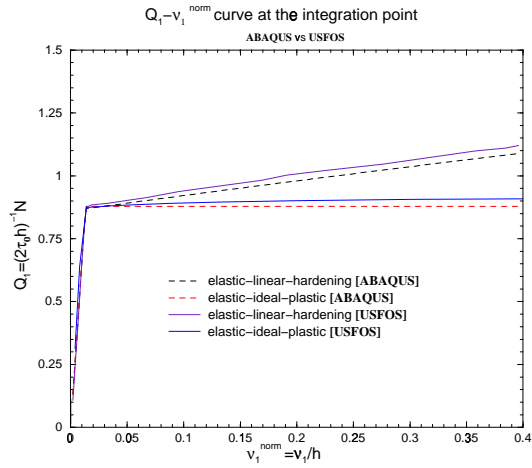
19

Figure 14: Generalized-normalized force vs the normalized displacement at the nodes of the line spring for two material models.

- the yield surface is updated due to crack growth and a further iteration procedure is carried out in order to satisfy the consistency requirement.

a)   b)
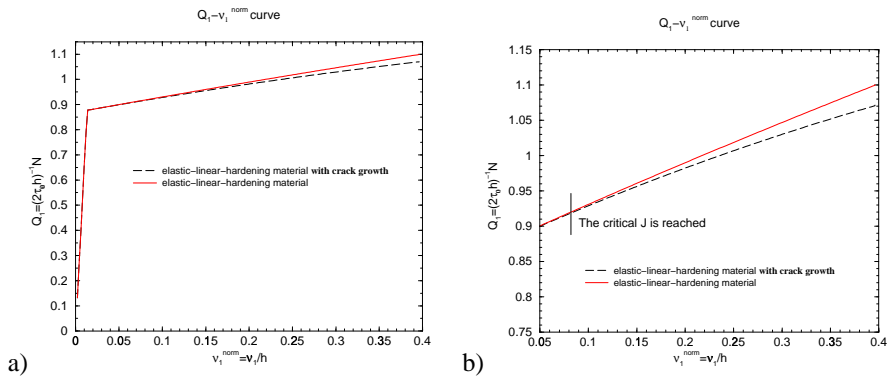
Figure 15: Generalized-normalized force vs the normalized displacement at the nodes of the line spring when crack growth is taken into account.
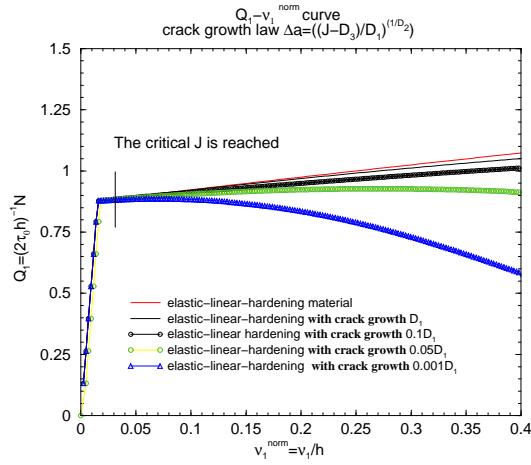
Figure 16: Generalized-normalized force vs the normalized displacement curves at the nodes of the line spring for different value of A.

Fig. 15 shows that the proposed procedure is suited to describe the combined effect of translation of the yielding surface due to hardening and the size decrease of the yielding surface due to crack growth. Note that a small softening is observed as the net result of hardening and ductile crack growth for a bilinear material. Fig. 16 shows that the amount of softening increases, as expected, when the parameter D_1 of the equation describing the crack growth law, Eq. 9, is decreased.

8 Conclusions

A methodology to link micro-mechanically based crack growth simulations with line spring analysis is proposed by suggesting an alternative way to calculate the $J - integral$ from the line spring framework. A parametrical study needs to be carried out in order to find out if the alternative J calculation is feasible for the framework it is meant for. A crack propagation law is suggested.
Some details of the numerical implementation of the backward Euler integration scheme at the integration point of the line spring element in order to account for plasticity are presented here for a bilinear material model. An efficient numerical procedure, based on the assumed crack growth law, is also presented in order to account for ductile crack propagation. A numerical case is considered, showing that the proposed procedure is suited to

the purpose.

A   The complete Gurson model

A.1   The Gurson model

The classical theory of plasticity states that plastic deformation will not change the material volume of a pure material. When a material contains voids, the volume will change under plastic straining and hydrostatic tension stress. The plastic flow becomes *dilatational* [11]. The consequence is that the material will soften and the load carrying capacity will decrease. The model which describes in a better way the softening effect due to the presence of voids is the one due to Gurson. The main assumptions upon which the Gurson yield function is derived are:

- von Mises condition is used to characterize the yield and flow of the matrix material, considered incompressible and undamaged

- the large strain involved in the ductile fracture prosess follows a rigid-plastic model

- a form is then assumed for the velocity field in the aggregate. The velocity allows the voids to grow under the requirement of incompressibility in the matrix. The velocity must meet the kinematic boundary condition corresponding to deformation rates on the surfaces of the unit cube

Based on the above assumption and on the simplification of spherical voids; Gurson obtaines a yield function $\phi(\sigma_{eq}, \sigma_H, f)$ where the softening effect and the damage measure f are contained:

$$\phi(\sigma_{eq}, \sigma_Y, f) = \frac{\sigma_{eq}^2}{\sigma_Y^2} + 2q_1 f \cosh\left(\frac{3}{2}\frac{q_2\sigma_H}{\sigma_Y}\right) - (1 + (q_1 f)^2) \tag{18}$$

where $f = \frac{dV_{voids}}{dV_{cell}}$ is the void volume fraction, $q_1, q_2 = 1$, σ_H is the mean normal stress, σ_{eq} is the conventional von Mises equivalent stress and σ_Y represents the flow stress of the matrix material. Gurson's main hypothesis is that microvoids are nucleated at positions sufficiently far apart as not to result in initial interactions between their local stress and strain fields.

The Gurson model cannot predict void coalescence, but describes well both *growth* and *nucleation* of voids [5]. The *void volume fraction* of a material during a plastic strain increment will change due to:

- the growth of existing voids

- the nucleation of new voids.

The increase of void volume fraction, df, from existing voids and newly nucleated ones will be added together and *homogenized* as 'one' void for the next load increment see Fig. 17:

$$df = df_{growth} + df_{nucleation}. \tag{19}$$

Void growth:

In order to define the growth of existing voids, df_{growth}, under plastic straining,

$$df_{growth} = V_2 - V_1$$
$$df_{nucleation} = V_3 - V_2$$
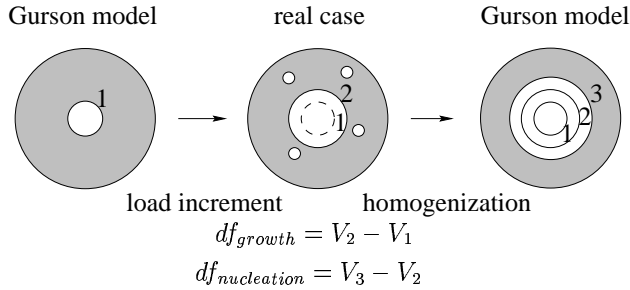
Figure 17: Schematic plot of ductile fracture mechanism

we must take into account the hypothesis of incompressibility for the matrix material. df_{growth} can be written as:

$$df_{growth} = (1 - f)d\varepsilon_{ij}^{P}\delta_{ij}. \tag{20}$$

where ε_{ij}^{P} is the plastic strain tensor.

Void nucleation:

Void nucleation is a highly material dependent process. Void nucleation depends, in general, on particle strength, size, shape and the hardening exponent of the matrix material. The nucleation mechanism can be strain controlled, or stress controlled where

the hydrostatic tension stress plays a role. There are several nucleation models, but only a few of them can be applied to the Gurson model. It has been common practice to relate the void nucleation to an increment of deformation which results in an increment of strain and an increment of stress. The general nucleation law can be written as:

$$df_{nucleation} = A d\varepsilon_{eq}^p + B(d\sigma_m + d\sigma_{eq}) \tag{21}$$

where ε_{eq}^p is the equivalent plastic strain increment associated with the plastic strain tensor and σ_{eq} is the Mises equivalent stress. In Eq. (21), the first term on the right hand side represents the part of nucleation due to the equivalent plastic strain increment and the second term due to the stress increment. A and B in Eq. (21) can be called the strain and stress controlled nucleation intensity.

A.1.1 Observations

- Eq. 18 predicts the material will soften and the load carrying capacity will decrease due to growth and nucleation of voids when increasing plastic strain is applied to the material.

- Eq. 18 does not contain any fracture criterion. It predicts ∞ ductility. In order to improve the equation and predict a more realistic loss of load carrying capacity, Tvergaard proposed different values for the parameters $q_1 = 1.5$ and $q_2 = 1$. Tvergaard's modification has the effect of amplifying the influence of hydrostatic stress at all strain levels, but the value of the void volume fraction at fracture is still unrealistically high.

- A material curve derived by using the Gurson model fits well with a curve derived by material tests up to a certain point where a bifurcation between the two curves takes place. The model predicts a ductility for the material which is much higher than that observed one by material tests. The impossibility of describing the observed bifurcation is due to the fact that no coalescence model is taken into account in the Gurson model.

Critical void volume fraction

The Gurson model fails to predict void coalescence. An alternative criterion has to be added to the original model in order to describe void coalescence. A possible criterion to describe such a process assumes that void coalescence appears when a critical void volume fraction, f_c is reached. In this way we add a localization or bifurcation condition to the Gurson model. The weakness of this criterion is that f_c is not a material parameter; it depends both on the initial void volume fraction and on stress triaxiality T. The

dependence on T can be relaxed in the case of small f_0. Once the void coalescence or, the bifurcation point, has been determined to occur according to a criterion, the void coalescence process can be simulated by the following function introduced by Tvergaard and Needleman:

$$f^* = \begin{cases} f & : \quad \text{for} \quad f \leq f_c \\ f_c + \frac{f_u^* - f_c}{f_F - f_c}(f - f_c) & : \quad \text{for} \quad f > f_c \end{cases} \tag{22}$$

where:

$f_c \longrightarrow$ critical void volume fraction at which void coalescence starts

$f_u^* = 1/q_1 \longrightarrow$ in order to keep numerical stability, never equal to 1

$f_F \longrightarrow$ volume fraction at final separation of the material Eq. 22 implies that, before void coalescence, the void volume fraction and the decrease of load carrying capacity takes the 'normal' way by the Gurson model. After the void coalescence has started, the void volume fraction will be amplified to represent the sudden loss of load carrying capacity. The void coalescence process is a really rapid process with large void volume expansion.

A.1.2 Observations

- Eq. 22 is not directly based on a physical process, but is the result of numerical fitting.

- It has been shown that the effect of void coalescence is well simulated by the function 22. Once $f = f_c$, the void growth rate is increased so that in a few steps the load carrying capacity is artificially reached.

- $f = f_c$ corresponds to the start of void coalescence. Eq. 22 adds the coalescence process to Eq. 18

- Difficulty to determine the critical void volume fraction parameter f_c.

Limits of the Gurson model

- **Non uniqueness** of the initial void volume fraction and damage evolution parameters. Many sets of parameters which describe the same material behavior can be found.

- Difficulty in the calibration of numerical models due to the high dependency on length scale.

- The parameter $f_c = f_c(f_0, \frac{\sigma_h}{\sigma_{eq}})$ is absolutely not a material independent parameter. It is fitted by comparing the Gurson model result and the experimental one. This parameter predicts void nucleation, measuring the numerical values at failure and is not connected with a physical failure mechanism.

A.2 Plastic limit load: a localized deformation model due to void coalescence

The deformation of void containing materials can be split, as discussed previously, into two distinctive phases: the homogeneous phase and the localized one. Thomason [11] developed his theory on a dual dilatational constitutive equation theory for ductile fracture. It is based on the observation that void coalescence is caused by localized necking of intervoid matrix. Thomason argues that there are two deformation modes in competition. Both deformation modes are dilatational. It means that they will result in change of material volume. Thomason states, out of thermodynamical considerations, that the material will always follow the deformation mode which needs less energy. Thomason found that the localized deformation mode can be described by a plastic limit model strongly dependent on the void/matrix geometry. For a material without voids the plastic limit load is
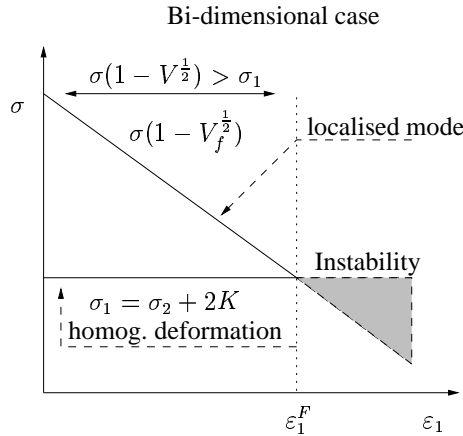
Bi-dimensional case

Figure 18: Homogeneous deformation mode vs Localized deformation mode.

infinite. In the beginning of the deformation process, the void dimensions are small and the corresponding plastic limit load is very large. In such a situation, the homogeneous

mode deformation prevails. The plastic limit load decreases proportionally to the growth of voids. Once the localized stress is equal to the plastic limit load, localized mode deformation becomes possible. Fig. 18 represents the effect of increasing plastic strain ε_1 on the 'virtual' plastic limit load stress $\sigma_n(1 - \sqrt{V_f})$, where V_f is the void volume, and the actual stress σ_1. The condition for void coalescence by internal necking of the intervoid matrix can be written in a unidimensional case as:

$$\sigma_1^{Homogeneous} = \sigma_1^{Localised} \tag{23}$$

where $\sigma_1^{Homogeneous}$ is the maximum principal stress at the current yield surface and represents the homogeneous deformation mode; $\sigma_1^{Localised}$ is the local maximum principal stress and represents the micro-capacity of a voided material to resist the localized deformation. Eq. 23 implies that if the applied load has reached the capacity of the material to resist the void coalescence, the unstable localized deformation mode will prevail and void coalescence will take place.

A.3 A complete Gurson model

In the complete Gurson model, Zhang uses Thomason's plastic limit load model as a coalescence criterion for the Gurson model. Zhang modifies Thomason's theory by assuming that the voids are always spherical. This modification makes the plastic limit load model fully compatible with the Gurson model. In the complete Gurson model, void coalescence is not determined by the critical void volume fraction f_c. f_c is the material response at void coalescence. The complete Gurson model contains:

- homogeneous yielding function:

$$\phi(\sigma_{eq}, \sigma_Y, f) = \frac{\sigma_{eq}^2}{\sigma_Y^2} + 2q_1 f^* \cosh\left(\frac{3}{2}\frac{q_2\sigma_H}{\sigma_Y}\right) - (1 + (q_1 f^*)^2) \tag{24}$$

- void grow and nucleation:

$$df = (1 - f)d\varepsilon_{ij}^P \delta_{ij} + Ad\varepsilon_{eq}^p + B(d\sigma_m + d\sigma_{eq}) \tag{25}$$

- void coalescence condition:

$$\begin{cases} \sigma_1 < \sigma_Y g(f, \varepsilon_i) & \text{no coalescence} \quad : \quad f^* = f \\ \sigma_1 = \sigma_Y g(f, \varepsilon_i) & \text{coalescence start} \quad : \quad f^* = f_c \end{cases} \tag{26}$$

the critical void volume fraction, f_c, is the material response at void coalescence. It depends on stress triaxiality and the initial value of void volume fraction $f_c = f_c(f_o, \frac{\sigma_H}{\sigma_Y})$.

- post-coalescence response:

$$f^* = f_c + \frac{f_u^* - f_c}{f_F - f_c}(f - f_c) \quad \text{for} \quad f > f_c \tag{27}$$

A.3.1 Observations

- The **non-uniqueness** problem is solved. f_c is automatically determined.

- If we suppose that the voids are nucleated at the beginning, f_0 is the only parameter which controls the failure behavior. This is not the real behavior, but gives good results.

- It is not possible for f_0 alone to describe the nucleation event completely. Other parameters metallurgically determined are used for this issue. When metallurgical analysts are not available, test results of fracture strain versus stress triaxiality can be used for fitting the nucleation parameters.

- Void nucleation parameters calibrated by a fitting which takes in consideration the triaxiality level can be transferred to different geometry.

- The model turned in to a fitting model. The one to one relationship between micro-mechanism and the parameters presented in the Gurson dilatation function is not longer achieved.

- Considering a simplified nucleation model also known as single parameter nucleation model (f_0(initial nucleation) or A(continuous nucleation), such a parameter can be used as a criterion in order to classify materials independent of geometry.

References

[1] Skallerud B. and Haugen B. Collapse of thin shell structures: stress resultant plasticity modeling within a co-rotated ANDES finite element formulation. *International Journal for numerical methods in Engineering*. 46, 1961-1986, 1999.

[2] Lee H. and Parks D. M., Fully plastic analysis of plane strain single edged cracked specimen subjected to combined tension and bending. *International Journal of Fracture* 63, 329-349, 1993.

[3] **Paper III:** Chiesa M., Skallerud B. and Gross D., Closed form line spring yield surfaces for deep and shallow cracks: formulation and numerical performance. Submitted for publ. *Computers and Structures* 2000.

[4] V. Tvergaard and A. Needleman Effect of crack meandering on dynamic ductile fracture. *J. Mech. Phys. Solid* V40, 1992, No.2, 447-471

[5] Z.L. Zhang, C. Thaulow, J. Ødegård A complete Gurson model approach for ductile fracture Engineering Fracture Mechanics 67 (2) (2000) pp. 155-168.

[6] **Paper IV:** Chiesa M., Skallerud B., and Nyhus B., Efficient numerical procedures for fracture assessments of surface cracked shells Presented at European Conference on Computational Mechanics

[7] Rice J. R., The line spring model for surface flaws. *The Surface Crack Physical Problems and Computer Solutions*. (ed J. L. Sweldow), ASME 1972.

[8] Rice J. R., A path independent integral and the appropriate analysis of strain concentration by notches and cracks. *J. Applied Mech*. 35, 379-386, 1968.

[9] J. W. Hutchinson, Singular behavior at the end of a tensile crack in a hardening material *J. of the Mechanics and Physics of solids*. 16, 13-31, 1968.

[10] J.R. Rice, G.F. Rosengren Plane strain deformation near a crcak tip in power-low hardening material *Journal of the Mechanics and Physics of Solids*. 16, 1-12, 1968.

[11] V. Tvergaard Material failure by void growth to coalescence *Advances in Applied Mechanics* 83-151, Academic Press, pp.69

[12] J. Koplik and A. Needleman Void growth and coalescence in porous plastic solids *Int. J. of Solids and Structures* 24 835-853, pp.19

[13] P.F. Thomason A three-dimensional model for ductile fracture by the growth and coalescence of microvoids. *Acta Metall*. 33, 1087-1095, 1985.

[14] P.F. Thomason Three-dimensional models for the plastic limit-loads at incipient failure of the intervoid matrix in ductile porous solids. *Acta Metall*. 33, 1079-1085, 1985.

[15] Simo J. C., Taylor R. L. A return mapping algorithm for plane stress elastoplasticity. *International Journal for numerical methods in Engineering*. 22, 649-670, 1986.

[16] Simo J. C., Taylor R. L. A return mapping algorithm for plane stress elastoplasticity. *International Journal for numerical methods in Engineering*. 22, 649-670, 1986.

[17] Williams M.L., On the Stress Distribution at the Base of a Stationary Crack. *J. Applied Mech*. Vol 24, 109-114, 1957.

[18] Wang Y. Y., Parks, D. M., Evaluation of the elastic T-stress in surface crcaked plates using the line-spring method. *Int.J. Frac.*. 56, 25-40, 1992.

[19] USFOS Theory Manual. Version 7.4 *SINTEF, Trondheim Norway, 2000*

[20] Skallerud B. Numerical analysis of cracked inelastic shells under large deformation or mixed mode loading *Int.J. of Solids and Structures*. 56, 25-40, 1999.

[21] Hibbit Karlson and Sorenson., ABAQUS Manual, version 5.2.

[22] White C.S., Ritchie R.O., and Parks D.M., Ductile growth of part through surface cracks: experiment and analysis. *ASTM STP 803*. (eds C.F.Shih and J.P.Gudas), ASTM 1983.

[23] Green A.P. and Hundy B. B., Initial plastic yielding in notch bend tests. *Journal of the Mechanics and Physics of Solids 16*. 1956, 128-144.

[24] Simo J. C., Taylor R. L. Consistent tangent operators for rate-independent elasto-plasticity. *Computer methods in applied mechnanics and engineering*. 48, 101-118 1985.

[25] Crisfield M.A. Non-linear Finite Element Analysis of Solid and Structures *Vol 1*.

[26] Simo J. C., Kennedy J. C. and Govindee S. Non-smooth multisurface plasticity and viscoplasticity. Loading/unloading conditions and numerical algorithms. *International Journal for numerical methods in Engineering*. 26, 2161-2186 1988.

[27] Crisfield M.A. Non-linear Finite Element Analysis of Solid and Structures *Vol 2*.

[28] Rice J. R. and Levy, N., The part through surface crack in an elastic plate. *J. Applied Mech*. 185-194, 1968.

[29] V. Tvergaard Material Failure by Void Coalescence in Localized Shear Bands. *Int. J. of Solids and Structures* V18, 659-672, pp.14

[30] J. Ødegaard and Z. Zhang Quantification Of Damage Parameters *Sintef report*

INTEGRATED LOCAL/GLOBAL ANALYSIS AND FRACTURE ASSESSMENT OF PIPELINES WITH DEFECTS

Bjørn Skallerud and Matteo Chiesa

Department of Applied Mechanics, thermo-, and fluid-dynamics,
Norwegian University of Technology, N-7491 Trondheim, Norway
e–mail: bjorn.skallerud@maskin.ntnu.no
e–mail: matteo.chiesa@matek.sintef.no

Tore Holmås

Dept. of Marine Structures,
Marintek,N-7777 Trondheim, Norway
e–mail: Tore.holmas@marintek.sintef.no

Abstract. *The present study addresses nonlinear finite element analysis of pipelines subjected to e.g. large curvatures. Cracks are accounted for by means of a newly developed line spring finite element formulation. Linking these elements to shell elements, and further linking the shell elements to beam elements, one has a global model of the pipeline that also accounts for local flexibilities and fractures due to defects (in the welds). This has obvious practical advantages, e.g. related to easy meshing/preprocessing, in addition to having a tool that directly provides fracture mechanics quantities, such as J-integral/CTOD etc, that is compared to the fracture toughness of the material. A recent development in this respect is the notion of two-parameter fracture assessment. This means that both the crack tip stress tri-axiality (constraint) and the corresponding fracture toughness is employed in the assessment, giving a much more realistic capacity of cracked structures. The above simulations are carried out by means of the software USFOS, accounting for large displacements and plasticity.*

1 Introduction

Pipelines are subjected to severe load histories during reeling and laying. The pipe segments are joined by means of girth welds, introducing local stress concentrations and weld defects. Using existing fracture assessment methods on a pipe subjected to e.g.. reeling, may not allow for any flaws at all due to the inherent conservatism in the method (e.g. PD 6491, BS, 1999). Production of welded pipelines free of defects is difficult or even impossible. Therefore it is of primary importance to have feasible assessment tools that are more accurate, giving more realistic capacities of pipe cross sections with cracks. With this, it can be shown that some defects can be accepted, and state of the art welding procedures may be sufficient.
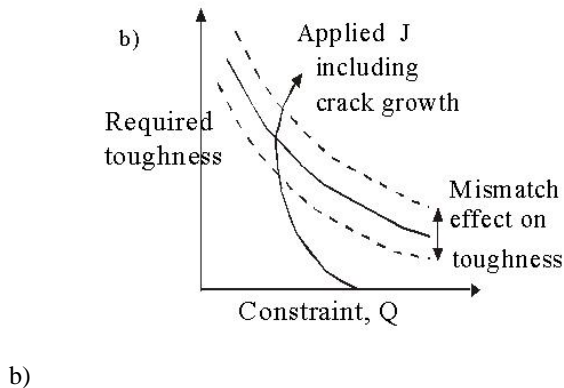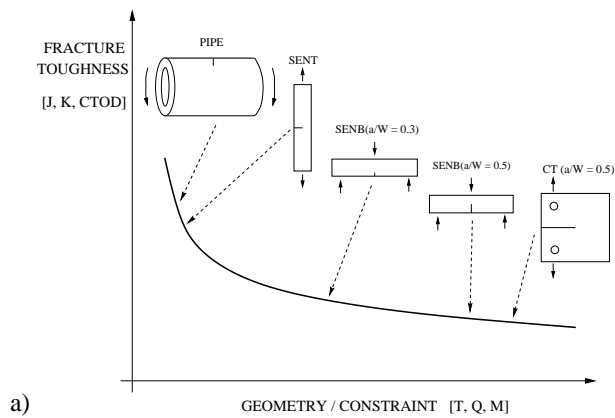

Figure 1: Effects of constraint on fracture toughness.

The present study addresses nonlinear finite element analysis of pipelines. The cracks are accounted for by means of a newly developed line spring finite element formulation [1], [2], [3].

Linking these elements to shell elements, and further linking the shell elements to beam elements, one has a global model of the pipeline that also accounts for local flexibilities and fractures due to defects. An important advantage with such an approach is a direct fracture mechanics assessment e.g. via computed $J-$integral or $CTOD$. A recent development in this approach is the notion of two-parameter fracture assessment. This means that the crack tip stress tri-axiality (constraint) is employed in determining the corresponding fracture toughness, giving a much more realistic capacity of cracked structures.

Fig.1a illustrates the effect of constraint on fracture toughness. It is noted that the usual fracture mechanics test specimens $(SENB, CT)$ have high constraint in the crack tip stress field, resulting in low toughness. A main characteristic with these specimens is that the ligament is loaded in bending. A ligament loaded primarily in tension, such as in a pipe or a single edge-notched tensile specimen $(SENT)$, provides a lower constraint and a higher toughness. The maximum allowable crack obtained using the fracture toughness from a $SENB$ or CT specimen, given a large external load or deformation, would be vanishingly small.

The welds are often the most critical part of the structure regarding unstable fracture. Proper design and selection of materials govern structural integrity. Current fabrication practice adopts a weld metal overmatch with respect to the base metal. The overmatch weld has the advantage to increase structural capacity (for cracks in the weld metal) for shallow and medium size cracks and thus improve resistance to failure of the welded joint. However, for cracks located in the heat affected zone (HAZ), weld metal overmatch may have detrimental effects see [4]. With the introduction of new high strength structural steels, undermatch welds may be expected. The best solution would be evenmatch, however, this is difficult to achieve in practice. Therefore, it is necessary to quantify the effect of weld metal mismatch. It turns out that a constraint based approach may be employed to obtain representative fracture toughness for this case also.

Often some ductile crack growth occurs before the critical fracture event is met. Fig.1b illustrates how constraint correction of the toughness works. The constraint may decrease initially due to increased plastic deformation, but as the crack grows, more bending is introduced in the ligament, and the constraint increases again. The fully drawn line represents the fracture toughness, whereas the dotted lines indicates effect of material mismatch (undermatch/evenmatch).

2 Theory

2.1 Two- and three-parameter fracture mechanics

In conventional fracture mechanics, it is assumed that crack tip stress field is controlled by a single parameter, e.g. the stress intensity factor K or the $J-$integral, and that the toughness obtained from tests with one specimen geometry can be transferred to structural applications. In general, there are two types of constraints in a weld: i) the geometry constraint caused by crack size, specimen dimensions and loading mode; ii) the material mismatch constraint due to inhomogenous material properties. These constraints may be characterized by the Q or T parameter and the M-parameter, respectively (O'Dowd and Shih [5], Betegon and Hancock [6], Ranestad et al. [7], Zhang et al [4], Parks [8], Kirk and Bakker [9]. The constraints invalidate

Table 1: **Nomenclature**

J	Rice's path independent integral
K	stress intensity factor
dN, dM	force and bending moment increments
$d\Delta, d\theta$	line spring deformation increments
σ_{ij}	components of stress tensor
δ_{ij}	Kronecker delta
C_t	tangent stiffness
σ	yield stress
Q, T, M	constraint parameters
r, θ	polar coordinates
$ctod$	crack tip opening displacement

conventional fracture mechanics, i.e. for a given value of crack driving force J, the crack tip stress field is influenced by the constraint level. Fig.2a illustrates the geometry constraint effect on the crack tip stress field, where a reference solution given by the upper curve may be the HRR-field (i.e. a crack in an infinitely large specimen), whereas the lower curve is the actual stress field. Hence, there is no one-to-one relation between the crack driving force and crack tip stress field, and the fracture toughness obtained from one case cannot be directly transferred to another one. For cleavage fracture occuring after significant plastic deformation, with attainment of a critical stress (normal or maximum principal stress) over a microstructurally relevant volume, the RKR criterion see [10], is a feasible failure criterion. Brittle fracture initiates when a critical stress is reached in front of the crack tip over a sufficiently large distance. If this distance is given by point 2 in Fig.2a, then one sees that the stress field in a low constraint situation has reached the critical stress over a too small distance, point 1. This situation is manifested in Fig.2b considering $J-$integrals. Here $J_{reference}$ is the $J-$integral that would exist in an infinitely large specimen with the same crack tip stress field as in the actual specimen. Fracture
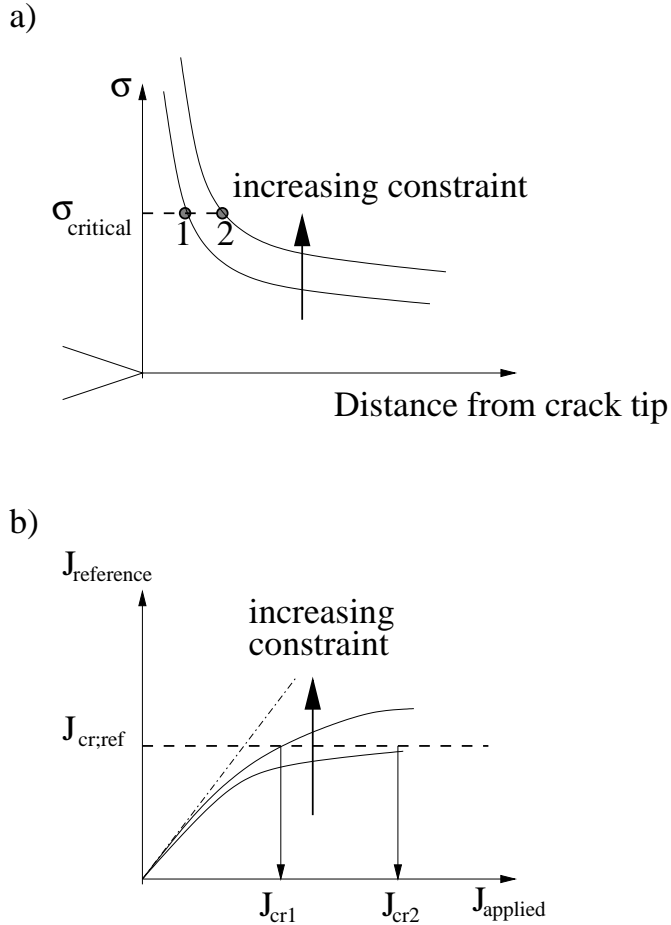
a)

b)

Figure 2: a) effect of constraint on crcak tip stress field, b)relationship between applied J and reference J

would initiate in a low constraint specimens for applied J equal to J_{cr1} or J_{cr2} . When these $J-$levels are reached, the RKR-criterion is fulfilled. Using the actual stress field (accounting for actual constraint), and comparing with the HRR stress field it is possible to determine what magnitude of Japplied that is required to initiate fracture.

The factors that influence the transferability and invalidate the one-to-one relation between crack driving force J and crack tip stress field is called constraint. For specimens made of homogenous materials, the constraint is termed geometry constraint. It has been proposed that the stress field at different levels of geometry constraint can be characterised by the $J-Q$ theory, i.e. the J integral and Q, a hydrostatic stress parameter see [5]. According to the $J-Q$ theory, the crack tip field inside the plastic zone can be separated into two parts. The first part is called reference field which is controlled by J, i.e. the one-to-one relation between the J and stress

field is maintained in the reference field. The actual stress field is influenced by the constraint level at the crack tip, it therefore modifies the reference field. This leads to a second stress field, called difference field, which is practically controlled by the parameter Q. The complete stress field can therefore be written:

$$\sigma_{ij} = \sigma_{ij}^{ref} + Q\sigma_{ij}\delta_{ij} \qquad (1)$$

The material strength distribution in a real weld is complicated and certain simplifications of a weld crack problem are needed. For a specimen made of inhomogenous materials with an inter-face crack, the observed fracture toughness of a reference material is obviously influenced by the mismatch properties of the material on the other side of the interface. For materials with identical elastic properties, there are three types mismatch: strength mismatch, hardening mismatch, and combination. Recently, extensive numerical studies have been carried out to investigate the effect of material mismatch constraint on the interface crack tip stress field of bi-material and tri-material boundary layer models. In the J-Q-M formulation a general approximation for the difference field has been used, i.e. $\sigma_{i,j} = \sigma_{i,j}(r, \theta, J, Q, M)$, [4], [7] , [11].

In order to relate $J_{reference}$ to fracture, an approach where the fracture is related to testing of weld thermal simulated $CTOD$ specimens has been applied. These specimens represents a ho-mogenous microstructure of the most brittle part of the HAZ, hence the mismatch constraint, M, will be zero. For many steels, fracture after weld thermal simulation are experienced at a low $CTOD$, giving only a limited size of the plastic zone and little relaxation from the initial high constraint in small scale yielding. In this way $J_{reference}$ can be related to the failure of homogeneous microstructures and a specimen size where valid J results are obtained (e.g. un-der small scale yielding). A horizontal limit in Fig.2b can be chosen to represent the critical J experienced in weld thermal simulation testing, and the $J - Q - M$ approach is then used to transfer from this "ideal" situation to the actual weld under consideration.

2.2 Finite element formulation

The finite element employed herein is quadrilateral thin shell element with six degrees of free-dom at each node, i.e. a higher order membrane displacement interpolation (drilling degree of freedom), denoted ANDES (acronym for assumed natural deviatoric strain). It is a non-conforming high-performance shell element, see [12], [13]. The plasticity modeling is based on a simplified version of Ilyushin's stress resultant yield criterion. One advantage with the simpli-fied yield surface is that one only have one active yield surface at any time in the stress update in addition to not having to integrate over shell thickness, see [14]. The line spring element is a one-dimensional element introducing additional flexibility in the shell due to surface cracks. The elastic stiffness is obtained from known solutions for edge cracked strips see [15]. The tan-gent stiffness is obtained by the flow rule, consistency condition, and assuming additive split of elastic and plastic deformations in the ligament

$$\begin{bmatrix} d\Delta \\ d\Theta \end{bmatrix} = \begin{bmatrix} d\Delta \\ d\theta \end{bmatrix}_e + \begin{bmatrix} d\Delta \\ d\theta \end{bmatrix}_p \qquad (2)$$

Here $d\Delta$ is the incremental line spring extension and $d\theta$ incremental line spring rotation. The plastic response of the line spring is governed by yield surfaces having the crack depth as
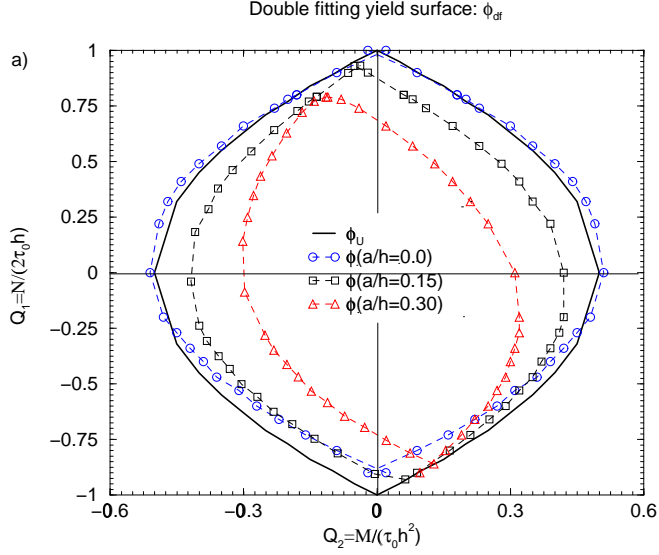
Double fitting yield surface: ϕ_{df}

Figure 3: Yield surface for different crcak depths ($a/h = 0, 0.15, 0.3$)

parameter, see Fig.3. The tangent stiffness has crack depth, yield stress , and hardening as parameters:

$$\left[\begin{array}{c} dN \\ dM \end{array} \right] = \mathbf{C}_T(a, \sigma^{LS}, E_P^{LS}) \left[\begin{array}{c} d\Delta \\ d\theta \end{array} \right] \tag{3}$$

With this one may employ weld metal material properties in the line spring if the crack is located in the weld, see [16]. The fracture mechanics parameters may be determined by means of elastic and plastic J-integral contributions. The elastic J is determined directly from stress intensity factors, the plastic J is calculated incrementally from the incremental plastic line spring deformations, i.e.

$$J_e = \frac{K_I^2}{E/(1 - \nu^2)}$$
$$dJ_p = f(d\Delta_p, d\theta_p)$$
$$J_p = \int dJ_p$$
$$J = J_e + J_p$$

Combining a computed $J-$integral with a measure of geometry constraint, initiation of fracture may be predicted. For the shell and line spring finite element model, a convenient way of determining constraint is by means of the $T-$stress. The $T-$stress is the second term in the asymptotic expansion of the elastic solution for the crack tip stress field by Williams see
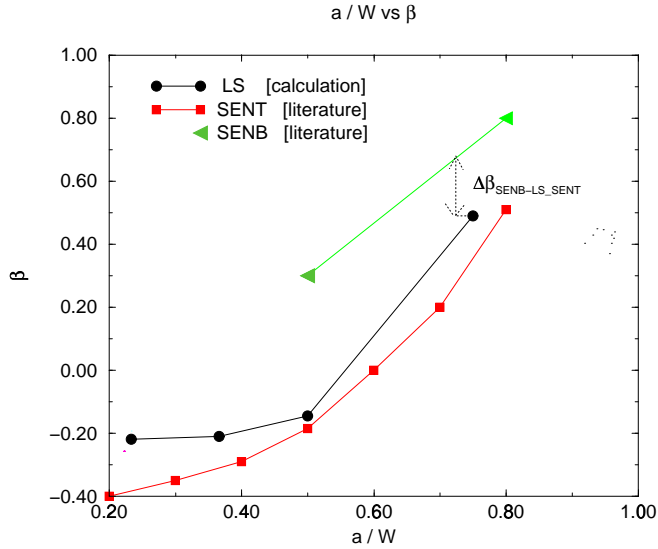
7

Figure 4: Constraint as a function of crack depth to thickness ratio for different specimens [3].

[17]. The T-stress has therefore been considered as an elastic parameter with a limited range of validity. Betegon and Hancock [6] have shown that the $T-$stress provides a good estimate of the constraint even beyond the elastic and small scale yielding regime. Lee and Parks [18] have proposed a method for calculating the $T-$stress for the shell-line-spring-mesh based on Sham's analytical work see [19]. By use of the membrane force and bending moment along the semi-elliptical crack front, the $T-$stress at any point along the crack front can be expressed, i.e. $T = T(a, N, M)$. Hence, a two-parameter fracture mechanics approach is possible with shell/line spring elements also. The following parameter is used to measure constraint: $\beta = T\frac{\sqrt{\pi a}}{K_I}$. This dimensionless parameter is plotted in Fig.4. It is observed that a higher (is obtained for the SENB specimen as compared to the SENT specimen.

3 NUMERICAL SIMULATIONS

3.1 Surface cracked plate in four-point bending

Surface cracked plate in four-point bending This case has been analyzed earlier by two alternative formulations (either a thick shell element or solid element analysis), see [20]. In the present study, a thin shell element is used with the new line spring formulation. A rectangular plate with two opposite boundaries pinned, the two other free, subjected to symmetric four point bending load. The pinned boundaries can carry membrane forces (in plane) in addition to the transverse load, see Fig.5a. Fig. 5b shows the total load versus load-line displacement for an intact plate and a surface cracked plate. A membrane force effect is noted in addition to the increased flexibility due to the crack.
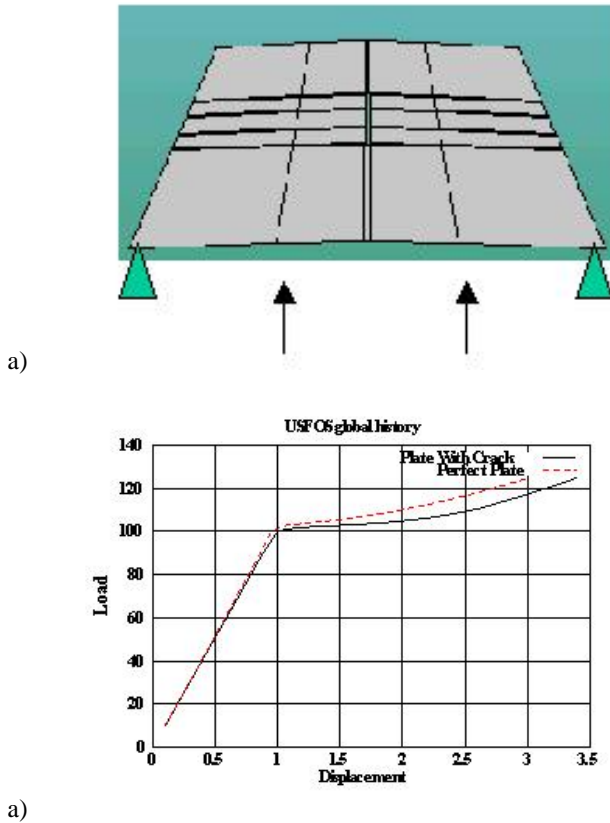
a)

a)

Figure 5: a) finite element mesh, b) load deflection curves.

3.2   Pipe subjected to bending

Test results for the present case is reported by Eide et al. [21]. It is a pipe subjected to four point bending. The pipe is girth welded at midsection, and a semi-elliptical surface crack is initiated there. The present case analyzed is denoted $T3$, the crack depth to crack width is 0.05, and the crack depth to shell thickness is 0.5. The shell thickness is $20mm$, and pipe diameter is $508mm$. The specimen length is $3840mm$. Yield strength and plastic hardening modulus is approximately $430Mpa$ and $730Mpa$, respectively. The weld can be considered evenmatch. The fracture toughness was determined by means of ctod testing of three-point bending tests of both base material and weld metal. An average critical ctod was $0.7mm$. Note that crack depth to thickness ratio for these tests was 0.5. According to Fig.4 the corresponding (is about 0.4, a high constraint. Fig.6 shows the computed and measured response given by normalized bending moment and deflection. The normalizing moment is the rigid plastic moment capacity. The test failed for a deflection about 0.1 times the diameter in a brittle manner. Eide et al. [21] used a

9
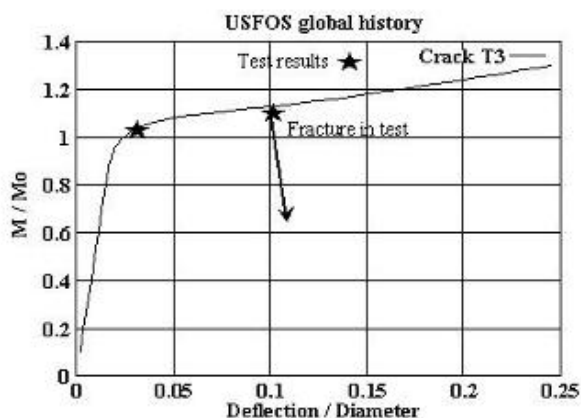
a)

Figure 6: Global response of surface cracked girth welded pipe.

level 3 failure assessment diagram in determining the critical $ctod$ at failure. With this, a critical ctod of $1.3mm$ was predicted, i.e. much higher than those measured by the three-point bend specimens. This is well explained by the constraint, since the computed constraint by means of the current approach is about zero (see also Fig.4). Hence, due to a reduced constraint in the pipe compared to the SNEB test results, the fracture toughness is increased significantly. Combining the global shell and line spring finite element calculation with a constraint corrected fracture toughness gives a more realistic capacity assessment with respect to fracture. Fig.7 depicts the contours of equivalent plastic strain in the shell elements in central part of the pipe. The red color represents strains higher than 1%. It is noted that some stress reduction in front of the crack gives a redistribution to the intact part of the shell. The line spring elements (not shown) also have a high utilization.

4 Concluding Remarks

A methodology accounting for cracks in girth welded pipes is presented. It is based on a combination of line spring elements, shell elements, and two-(or three-)parameter fracture mechanics assessments. The central points are that three-dimensional modeling of the crack is not necessary, and fracture mechanics parameters are computed in an efficient manner. In addition to the usual calculation of $J-$integral or $CTOD$, the fracture assessment is supplemented by a constraint measure that scales the failure condition. In most cases this is manifested by having very conservative critical CTOD values from the typical fracture mechanics test specimens, and with a constraint correction representative for the actual pipe, the conservatism is reduced. A consequence of this is that present weld procedures may be satisfactory and finite sized weld defects may be accepted.
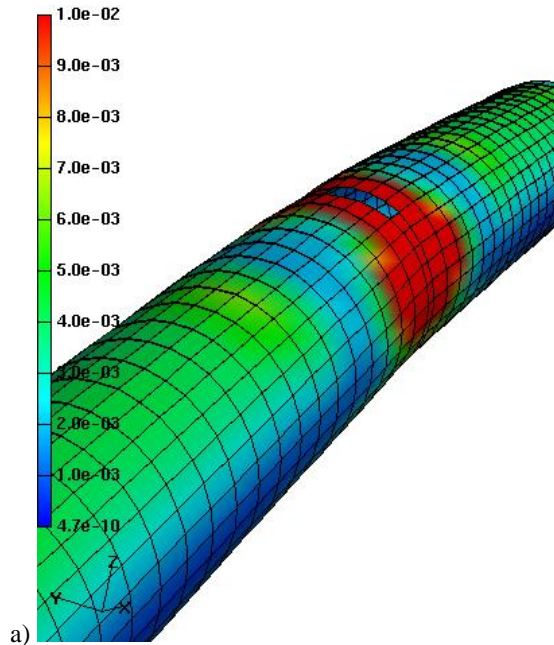
Figure 7: Global response of surface cracked girth welded pipe.

References

[1] Skallerud B., A mixed mode I/II inelastic line spring. *Int. J. Solids Struct.* 33 , 4143-4166,1996.

[2] Skallerud B., Numerical analysis of cracked inelastic shells with large displacements or mixed mode loading. *Int. J. Solids Struct.* 36 , 2259-2283,1999.

[3] **Paper II:** Chiesa M., Nyhus B., Skallerud B. and Thaulow C., Efficient fracture assessment of pipelines. A constrain-corrected SENT specimen approach. Engineering Fracture Mechanics 68, 527-547, 2001.

[4] Zhang Z. L., Thaulow C. and Hauge M., Effects of crack size and weld metal mismatch on the HAZ cleavage toughness of wide plates. *Engineering fracture mechanics* 57 , 653-664, 1997.

[5] O'Dowd N. P. and Shih C. F., Family of crack tip fields characterized by a triaxility parameter-Part I,II. *J. Mech. Phys. Solids* 40 ,939-963, 1995.

[6] Betegon C., and Hancock J.W., Two-parameter characterization of elastic plastic crack-tip fields.*J. Appl. Mech.* 58, 104-110, 1991.

[7] Ranestad Ø., Zhang Z. L. and Thaulow C., Two-parameter (J-M) description of crack-tip stress-fields for an idealised weld in small scale yielding. *Int. J. of Fracture* 2000.

[8] Parks D. M., Advances in characterization of elastic-plastic crack tip fields. Topics in fracture and fatigue *J. Press. Vessels Tech.* 104, 287-292, 1992.

[9] Kirk M., and Bakker A. Constraint effects in fracture and application. second volume *ASTM STP 1244, Philadelphia.*

[10] Ritchie R. O., Knott J. F. and Rice J. R., On the relationship between critical tensile stress and fracture toughness in mild steel. *J. Mech. Phys. Solids* 21 , 395-410, 1973.

[11] Zhang Z. L., Hauge M. and Thaulow C. Two-parameter characterization of the near tip stress fields for a bi-dimensional elastic-plastic interface crack. *Int. J. Fracture.* 79 , 65-83, 1996.

[12] Felippa C. A. and Militello C. Membrane triangles with corner drilling freedoms: II. The ANDES element. *Finite Elem. in Analysis & Design.* 12, 189-201, 1992.

[13] Haugen B. Buckling and stability problems for thin shell structures using high performance finite elements. Ph.D.thesis, Univ. Colorado, Dept. Aerospace Engng. 12, 189-201, 1994.

[14] Skallerud B. and Haugen B. Collapse of thin shell structures: stress resultant plasticity modeling within a co-rotated ANDES finite element formulation. *International Journal for numerical methods in Engineering.* 46, 1961-1986, 1999.

[15] Rice J., and Levy N. The part through surface crack in an elastic plate. *J. Applied Mech.* 185-194, 1972.

[16] **Paper I:** Chiesa M., Skallerud B. and Thaulow C., Line spring elements in a yield strength mismatch situation with application to welded wide plates. To appear in *Engineering Fracture Mechanics.*

[17] Williams M.L. On the stress distribution at the base of a stationary crack. *J.Applied Mech.* 24 , 109-114, 1957.

[18] Lee, H. and Parks D.M., Enhanced elastic-plastic line spring finite element. *Int. J. Solids Struct.* 32 , 2393-2418,1995.

[19] Sham T.L., The determination of the elastic T-term using higher order weight functions. *Int.J. Fracture.* 48 , 81-102, 1991.

[20] Skalerud B. and Zhang Z.L. Finite element modeling of cracked inelastic shells with large deflections: 2D and 3D approaches. *Int. J. Fatigue and Fract. Engng Mater and Struct.* 24 , 109-114, 2000.

[21] Eide O.I., Berge S., and Lereim J. Fracture tests of girth welded tubular models with surface cracks. *WELDTECH'88, London.*